Titre: Title:	Characterization of microstructure and dopant distribution of laser diffused resistors
Auteur: Author:	Yougui Liao
Date:	2005
Type:	Mémoire ou thèse / Dissertation or Thesis
Référence: Citation:	Liao, Y. (2005). Characterization of microstructure and dopant distribution of laser diffused resistors [Thèse de doctorat, École Polytechnique de Montréal]. PolyPublie. https://publications.polymtl.ca/8187/

Document en libre accès dans PolyPublie
Open Access document in PolyPublie

URL de PolyPublie: PolyPublie URL:	https://publications.polymtl.ca/8187/
Directeurs de recherche: Advisors:	Michel Meunier
Programme: Program:	Non spécifié

NOTE TO USERS

UNIVERSITÉ DE MONTRÉAL

**CHARACTERIZATION OF MICROSTRUCTURE AND DOPANT
DISTRIBUTION OF LASER DIFFUSED RESISTORS**

YOUGUI LIAO

DÉPARTEMENT DE GÉNIE PHYSIQUE

ÉCOLE POLYTECHNIQUE DE MONTRÉAL

THÈSE PRÉSENTÉE EN VUE DE L'OBTENTION

DU DIPLÔME DE PHILOSOPHIÆ DOCTOR

(GÉNIE PHYSIQUE)

2005

Canada

UNIVERSITÉ DE MONTRÉAL

ÉCOLE POLYTECHNIQUE DE MONTRÉAL

Cette thèse intitulée :

CHARACTERIZATION OF MICROSTRUCTURE AND DOPANT DISTRIBUTION OF LASER DIFFUSED RESISTORS

Présentée par: Yougui LIAO

en vue de l'obtention du diplôme de : Philosophiæ Doctor

a été dûment acceptée par le jury d'examen constitué de :

M. MARTINU Ludvik, Ph.D., président

M. MEUNIER Michel, Ph.D., membre et directeur de recherche

M. SCHIETTEKATTE François, Ph.D., membre

Mme. SIMARD-NORMANDIN Martine, Ph.D., membre

ACKNOWLEDGEMENTS

Finally, I would like to thank all my friends in Montreal for making this period of my life an enjoyable and meaningful one.

ABSTRACT

Recently, a laser fine tuning (LFT) technology had been developed for fabricating highly accurate resistances, which are compatible with the conventional CMOS fabrication flow used in commercial microelectronics industry. This method uses very small die area to produce Si laser diffused resistors (LDRs). In the fabrication process, the doping atoms diffuse from the highly doped, so-called source and drain, regions into the lightly doped gap region (with opposite dopants) when the Si materials is melted by focusing a laser beam on the center of the gap region and the edges of the adjacent heavily doped regions. Therefore, the two heavily doped regions can be connected by the diffused resistive link with a medium dopant concentration, forming LDR. The resistance value of the LDR can be highly controlled by adjusting the parameters, involving the laser focused spot size, laser power, pulse duration, number of laser expositions and position of the laser spot relative to the gap, heavily doped regions and initial structures of the devices. One main advantage is that there are no needs of additional fabrication steps before the laser trimming process. Nd:YAG (Neodymium:Yttrium Aluminum Garnet) with wavelength of 532 is one good choice to provide energy to melt silicon materials.

In order to completely understand the laser-processing mechanisms and accurately control the electrical and material properties of the LDRs, the research during this thesis was focused on microstructural characterization and dopant distribution measurements of LDRs fabricated under various laser parameters and different initial device structures. The aim of the project was to use theses results to improve the accuracy, thermal coefficient of resistance (TCR) and long-term stability of those microdevices.

Obtaining accurate quantified electrically activated dopant distribution in the actual microelectronic devices was a real challenge, especially when one considers microdevices (LDRs) having a very small area of few μm^2. By considering a vector as etching rate instead of a scalar (as considered by previous researchers) and by using a

novel calibration method, the reliability, reproducibility and accuracy of quantification of dopant concentrations, ranging from 9×10^{16} to 6×10^{19} atoms/cm^3, of the dopant evaluation technique have been significantly improved. Therefore, the dopant profiles in the non-irradiated heavily doped regions in our devices were obtained using dopant selective etching (DSE) in combination with cross-sectional transmission electron microscopy (TEM) and focused ion beam (FIB) techniques. Furthermore, the developed method has been applied to our LDRs and the two-dimensional (2D) dopant distributions with wide range of boron concentrations of the resistive links were quantified with spatial resolution of 1 to 5 nm. This results shows that the LDRs with boron concentrations up to ~ 0.24×10^{18} atoms/cm^3 and ~8.9×10^{18} atoms/cm^3 can be produced depending on different structures of initial microdevices and laser parameters. Those profiles were accurately compared with numerical simulation results based on heat transfer and diffusion equations.

Three-dimensional (3D) and two-dimensional (2D) periodic silicon nanostructures formed by polarized focused Nd:YAG laser irradiation (532 nm) with spot size less than 3 μm on Si covered by SiO$_2$ are presented in this thesis. We observed different structures, including periodic coexisting of liquid and solid, and ripples, were obtained under different laser intensities. However, when the light intensity is out of those ranges, either no melting was created or the periodicity was destroyed. The periodicity of these periodic structures is 360 nm related to the wavelength of frequency doubled Nd:YAG laser and the index of refraction of SiO$_2$. We propose a model based on the fact that as the oxygen is diffusing locally from SiO$_2$ into the melted Si, thus forming SiO$_\beta$ with a lower melting point.

The resistivity and dopant distribution in these arrays of periodic submicron resistive links between the heavily doped regions were characterized. Then, the widths were measured by scanning capacitance microscopy (SCM), the depths were obtained by TEM and DSE, and then resistance values were measured using a four-point probe technique. Those arrays with different resistance values in LDRs can be accurately achieved by finely controlling the laser power and pulse widths. The SCM technique

not only detects material properties at surface but also detects those at pn junctions near surface regions as a consequence of the built-in depletion based on different polarity of the applied DC bias voltage (V_{DC}). A mechanism related to oxygen activation as donors is also proposed to explain the measurements of SCM signal vs. V_{DC}. Moreover, the dopant uniformity in LDRs, fabricated with laser power of 3.10 W and 3.75 W, is also deduced. It was found that between 2 to 7 submicron conductive links are formed in the focused spot size of 3 μm and their number depends only on laser intensity ranging from 3.10 W to 3.75 W, while their average width (151 − 300 nm) and depth (108 − 147 nm) strongly depends on both laser intensity and number of laser pulses. The resistances of these links are between 363 − 493 Ω and the effective average doping levels are from 1.5×10^{18} to 2.4×10^{19} cm^{-3}.

The physical structures, induced by laser irradiation with various process parameters, were obtained by microstructural analytical methods, such as TEM and AFM (atomic force microscopy), in combination with chemically selective etching technique. Point defects, dislocations, interdiffusion of both oxygen and silicon between the dielectrics and the melted silicon as well as mass transportation due to liquid convection are determined. Furthermore, the formation mechanisms of these point defects and dislocations are also proposed. The presence of point defects and dislocations implies that long laser pulses should be used in the LDRs' fabrication. The regrowth of Si crystal simultaneously starting from both the dielectrics/Si interface and the Si-liquid/solid interface is for the first time suggested. The origin of this phenomenon is based on the increase of heat conductivity of the dielectrics due to diffusion of Si from the melting pool into the hot dielectrics. The liquid convection induces non-ideal dopant transportation. Therefore, the oxygen and silicon inter-diffusion and liquid convection suggests that short laser pulses should be used in fabrication process. All these structural information suggests that fabrication of high quality LDRs requires considering and controlling all processing conditions.

CONDENSE EN FRANÇAIS

Plusieurs applications utilisant des circuits intégrés mixtes à haute vitesse, tels que les télécommunications, les circuits de référence de tension, les ajusteurs de fréquence analogique, les oscillateurs contrôlés par tension, ou encore les convertisseurs numérique/analogique (N/A) et analogique/numérique (A/N) de haute précision, requièrent une technologie de pointe qui est toutefois limitée par la précision de ses composants tant actifs que passifs. Cette imprécision se traduit, dans la fabrication de résistances par couche minces et épaisses, en une variation de l'ordre de 10% à 20% des résistances par rapport aux valeurs attendues [1]. Parker et al. ont démontré que pour plusieurs circuits intégrés de haute performance, tel que les convertisseurs N/A et A/N, une précision de l'ordre de 2% [2] est trop élevée pour plusieurs résistance fabriquée à partir de silicium polycristallin. Afin de produire des circuits plus performants, l'ajustement des valeurs de résistance dans les circuits intégrés par un procédé post-fabrication constitue une technique efficace. Ces résistances ajustables sont utilisées pour compenser les variations de résistance inhérentes au procédé de fabrication. Généralement, les résistances sont ajustées finement vers le haut en réalisant l'ablation du matériau constituant la couche sur certaines portions de la résistance.

Une technologie d'ajustement par laser novatrice, compatible avec la technologie conventionnelle CMOS, a récemment été développée [3] pour la fabrication de résistances ultra précises. Ce procédé est connu sous le nom de *Laser Fine Tuning technology* (LFT) et est commercialisée par *LTRIM Technologies* sous la marque de commerce FASTRIM[TM]. Cette méthode d'ajustement utilise qu'une très petite surface pour produire des résistances diffusées par laser (*Laser Diffused Resistance* ou LDRs). Un avantage de cette technique est qu'elle ne nécessite aucun procédé de fabrication additionnel.

Tel que montré dans les précédentes publications de notre groupe de recherche [3-6], la technique d'ajustement par laser est réalisée sur un MOSFET sans grille produit par n'importe quel procédé de fabrication CMOS conventionnel. La résistance peut être faite de silicium monocristallin dopé N, par exemple avec de l'arsenic (As) et/ou du phosphore (P), ou dopé p, par exemple avec du bore (B), avec une large fourchette de concentration de dopant. Par exemple, pour la fabrication d'une résistance de type P, la structure du composant de départ comprend deux régions fortement dopées en bore, formées par implantation ionique dans un puits de type N avant un recuit. Ces deux régions sont séparées par une structure d'une certaine longueur (L), ce qui résulte en la formation de deux jonctions PN en série. La largeur des régions implantées est d'environ 4µm. Le dispositif est connecté en utilisant le réseau d'interconnections du circuit intégré. En raison de la présence des deux jonctions PN se faisant face, avant le LFT, le seul courant qui parcoure le dispositif est

le courant de fuite de l'une ou l'autre des diodes. Le dispositif se comporte donc essentiellement comme un circuit ouvert de résistance infinie.

L'irradiation laser de l'espace entre les régions fortement dopées par un faisceau focalisé dont le diamètre est inférieur aux régions dopées induit une augmentation de la température du silicium et, éventuellement, sa fusion. Puisque le coefficient de diffusion du silicium liquide est relativement élevé, les atomes de dopants vont diffuser rapidement des régions fortement dopées vers les régions faiblement dopées de la région médiane. Suite à l'arrêt de l'irradiation, le silicium liquide se solidifie avec un nouveau profil de dopant, créant par le fait même un lien résistif entre les régions fortement dopées. Afin d'éviter d'endommager les dispositifs et structures avoisinants et de produire des LDRs de haute qualité et de haute précision, les différents paramètres du procédés sont contrôlés. Ceux-ci comprennent la dimension du faisceau laser focalisé, la puissance du laser, la durée de l'impulsion, le nombre d'impulsions envoyées, la position du faisceau laser par rapport aux différentes structures initiales du dispositif. Plusieurs sources laser peuvent être utilisées pour la technique du LFT. Le laser Nd :YAG représente un bon candidat grâce à sa puissance élevée qui peut faire fondre le silicium même sous plusieurs couches diélectriques réparties sur une épaisseur totalisant environ 8 μm.

Cette thèse porte sur la caractérisation microstructurale des dispositifs fabriqués par le procédé LFT afin de mieux comprendre les mécanismes en jeux. Cette

meilleure compréhension permettra un meilleur contrôle des propriétés tant électriques que structurales des résistances diffusées ainsi qu'une amélioration de la précision et de la stabilité de celles-ci. Au niveau industriel, cette démarche pourra mener à une optimisation de la technique du LFT et des structures de départ utilisées pour la LFT. Les propriétés des LDRs pourraient se trouver détériorées par certains défauts, que ce soit des défauts ponctuels (interstices, lacunes), des dislocations, ou encore des impuretés (principalement de l'oxygène provenant des diélectriques). L'uniformité de la distribution en impuretés dans le Si solidifié pourrait aussi avoir un impact important sur la stabilité et les propriétés électriques du dispositif en introduisant des niveaux énergétiques dans la bande interdite du Si. De plus, on pourrait vérifier que la valeur de résistance des LDRs sont dépendantes de la distribution de dopant induit par la LFT.

Le taux de refroidissement très élevé du silicium liquide dû à la basse température du substrat favorise la formation de défauts ponctuels. La probabilité de contraintes thermiques importantes lors de l'irradiation laser et de réarrangement fautif lors de la cristallisation du silicium liquide pourrait induire la formation de craques et de dislocations. Le gradient de température à l'interface diélectrique/silicium liquide peut de plus y causer une différence de tension de surface qui induit un transport de masse par convection qui vient s'ajouter au terme de diffusion. Le rayonnement du laser peut aussi être absorbé par les couches diélectriques, augmentant leur température et brisant les liens oxygène-silicum, autorisant une diffusion d'oxygène

dans le silicium liquide. Cependant, tous ces phénomènes n'ont lieu que dans un très petit volume (2 µm à 4 µm) à l'intérieur de la zone irradiée. L'évaluation bidimensionnelle de ces caractéristiques est réalisée à l'aide de techniques à haute résolution tels que la microscopie électronique à transmission (TEM), la microscopie électronique à balayage (SEM), la microscopie à force atomique (AFM), la microscopie à balayage capacitif (SCM), la gravure chimique ainsi que des mesures électriques combinées avec des techniques unidimensionnelles, par exemple la spectroscopie de masse des ions secondaires (SIMS).

Cette thèse se divise en huit chapitres. Le premier chapitre introduit les concepts de base concernant le LFT ainsi que les motivations et les objectifs de ce travail. Le deuxième chapitre résume les précédents travaux de recherche reliés aux objectifs de cette étude. Le troisième chapitre porte sur les techniques d'analyse utilisées pour la caractérisation microstructurale : analyse des défauts ponctuels, dislocations et défauts de volume.

Le quatrième chapitre présente une méthode novatrice de quantification de la distribution de dopants. Cette méthode, basée sur la microscopie électronique à transmission (TEM), la gravure sélective des dopants et la technique du faisceau d'ions focalisé (FIB), peut de plus être utilisée pour d'autres dispositifs dans l'industrie de la microélectronique. Le taux de gravure est ici considéré comme un vecteur plutôt que comme un scalaire. Celui-ci est déterminé par une modélisation du

procédé de gravure ainsi que par une méthode de calibration novatrice. En comparaison avec les techniques conventionnelles de détermination de profils de dopage (DES/TEM), cette méthode permet l'amélioration de la reproductibilité, de la précision et de la fiabilité des mesures. La concentration en dopants des résistances diffusées testées varient de 9×10^{16} à 3.6×10^{18} atoms/cm^3. Les résultats d'une simulation numérique basée sur les équations de la chaleur et de diffusion sont en accord avec les résultats expérimentaux.

Le cinquième chapitre présente deux structures périodiques formées sur un substrat de silicium couvert par une couche d'oxyde SiO$_2$. Elles sont dues à une variation des composés chimiques induite par la diffusion des impuretés. Ces structures apparaissent suite à l'irradiation du substrat par un laser polarisé, et ce pour différentes intensités laser. Pour certaines intensités dites élevées, des vaguelettes sont formées, correspondant à la fusion complète de la région irradiée. Pour d'autres intensités dites faibles, une coexistence des phases liquides et solides est induite. Dans ce chapître, nous présentons les nanostructures de silicium obtenues en focalisant un laser polarisé Nd:YAG (532 nm) sur un substrat de silicium (Si) recouvert d'une couche d'oxyde (SiO$_2$). La dimension de la tache focale est inférieure à 3 µm. Les nanostructures observées sont bi ou tridimensionnelles et présentent un caractère périodique. Nous observons qu'à faible intensité laser (0.9 à 1.08W), une périodicité bidimensionnelle des phases liquides et solides est présente tandis qu'à forte intensité (1.08 à 1.44W), des vaguelettes tridimensionnelles sont formées. En dehors de ces

valeurs d'intensité, soit la fusion n'a pas lieu (<0.9W) ou la périodicité est détruite (>1.44W). La période des nanostructures formées est de 359nm et est déterminée à la fois par la longueur d'onde du laser incident et l'indice de réfraction de la couche d'oxyde. Nous proposons un modèle basé sur l'hypothèse que la diffusion locale de l'oxygène du SiO_2 vers le Si liquide crée un composé SiO_β dont le point de fusion est inférieur au SiO_2, engendrant une fusion préférentielle de ces régions. Ce phénomène entraîne alors une dynamique de rétroaction positive à la suite des impulsions successives, créant les nanostructures observées. Les résultats d'une modélisation basée sur la variation du point de fusion et du coefficient de réflexion du silicium et de ses différents oxydes confirment les résultats expérimentaux.

Le sixième chapitre se concentre sur l'étude de la création et des propriétés des résistances submicroniques créées par la coexistence des phases liquides et solides. Cette étude a été réalisée principalement à l'aide du microscope à balayage capacitif (SCM). Les résultats expérimentaux montrent que la résistivité augmente et que la concentration nette de dopant diminue lorsque qu'une intensité laser plus forte ou un nombre plus important d'impulsions est utilisé. De plus, les nombres de ces liens conducteurs dépendent seulement de l'intensité du laser tandis que leur largeur dépend à la fois de l'intensité du laser et du nombre d'impulsions utilisés. Des matrices périodiques de résistances sub-microniques ont été fabriquées sur un substrat de silicium recouvert d'une couche de SiO_2. Ce résultat a été obtenu en focalisant un laser pulsé et polarisé Nd:YAG à fréquence doublée sur le puits entre deux régions

fortement dopées. Une diffusion préférentielle des dopants induite par une fusion périodique du silicium explique la formation de ces résistances.. De 2 à 7 résistances ont été observées à l'intérieur de la tache laser de 3 µm. Il a été montré que ce nombre ne dépend que de l'intensité du laser, dans notre cas variant de 3.10 W à 3.75 W. Il a de plus été montré que la largeur moyenne (151 – 300 nm) et la profondeur (108 – 147 nm) de ces structures dépendent fortement à la fois de l'intensité laser et du nombre d'impulsions effectuées. Les résistances mesurées varient entre 363 et 493 Ω tandis que la concentration de dopant moyenne varie de 1.5×10^{18} à 2.4×10^{19} cm^{-3}.

Le septième chapitre porte sur la caractérisation microstructurale des dispositifs ajustés par laser qui comporte des défauts ponctuels, des dislocations et des défauts volumiques. Un mécanisme de formation de ces défauts y est suggéré. Une stratégie visant à optimiser la production de dispositifs de haute qualité par irradiation laser y est aussi proposée.

Finalement, le huitième chapitre présente les conclusions de cette thèse et formule des recommandations concernant les futurs travaux, tant expérimentaux que de modélisation, requis pour approfondir la compréhension des phénomènes physiques en jeux dans les LDRs.

TABLE OF CONTENTS

CHAPTER 6 ARRAY OF PERIODIC SUBMICRON CONDUCTIVE LINKS IN SI COVERED BY SIO₂ FORMED BY POLARIZED LASER IRRADIATION

CHAPTER 7 STRUCTURAL CHARACTERIZATION OF LASER DIFFUSED RESISTORS

CHAPTER 8. GENERAL DISCUSSION AND CONCLUSIONS

LIST OF FIGURES

LIST OF TABLES

LIST OF APPENDICES

CHAPTER 1 INTRODUCTION

1.1. LASER FINE TUNING TECHNOLOGY

Many high-speed mixed-signal integrated circuits (ICs) applications, such as telecommunication, precision voltage reference circuits, analog frequency tuning circuits, VCO's D/A and precision A/D converters, require high performance technologies that are ultimately limited by the accuracy of both active and passive components of the technology. For example, inaccuracies and variations in thin film and thick film resistance deposition typically result in 10% to 20% variation from the designed resistance values [1]. Parker et al. had demonstrated that for many high performance ICs such as A/D and D/A converters, using a relative accuracy of about 2% [2], is still unacceptable in many polycrystalline silicon resistors. In order to produce superior circuit performance, it is necessary to adjust the resistor values in integrated circuits (ICs) after fabrication. These tunable resistors are employed to compensate for resistance variation existing in fabrication flow. Generally, the resistors are trimmed continuously (fine adjustment) upwards by removing the film material from certain portions of the resistance, while downward trimming is not generally attempted because it calls for the addition of material to the film. Furthermore, as indicated in Table 1.1 [3], most trimming methods, involving laser ablation of thin or thick films, and mesh trimming,

Table 1.1 Major resistance trimming methods

Method	Resolution	Size	Special Processing (besides trimming)
Thin and thick film trimmed by laser, ion and electron beams		Large	Resistive film
Mesh trimming	Discontinuous	Large	Resistive film
Laser polysilicon link making	Continuous	Small	Polysilicon film on field oxide with masking and implantation
Polymer trimming	Continuous	Large	Polymer film
Pulsed voltage	Continuous	Large	Resistive film and additional pads
Floating gate device	Continuous	Large	Additional pads
Laser-diffused resistance	Continuous	Very small	None

and laser polysilicon link making, require an added processing steps needed to fabricate them. For example, before laser polysilicon link making, some additional process such as implantation of polysilicon and masking processes are required in the previous fabrication process [2]. These complex processes add additional cost and potential yield problems.

Recently, a novel laser-trimming technology was developed [3] for fabricating high accurate resistances, which is compatible with the conventional CMOS fabrication flow used in commercial microelectronics industry. This process is now called Laser Fine Tuning (LFT) technology and is commercialized by LTRIM Technologies under the trade mark FASTRIM^{TM}. This trimming method uses very small die area to produce laser diffusible resistors (LDRs). One typical advantage is that there are no needs of additional fabrication steps before the laser trimming process.

As shown in previous publications by our research group [3 – 6], the LFT technique is performed on a gateless MOSFET structure produced by any conventional CMOS fabrication flow. The resistor can be doped monocrystalline silicon with n-type, such as arsenic (As) and/or phosphorus (P), or p-type dopants, such as boron (B), with a wide range of carrier concentrations. As an example, as shown in Fig. 1.1, for a p-type resistor the device structure involves two highly boron doped regions, which are formed by ion implantation into an n-well and then annealed, and are separated by a gap with a certain length (L), resulting in two p-n junctions in series. The width of the ion-implanted areas in the devices, used for fabricating LDRs, is about 4 μm. The electrical connections to the device are formed using vias and interconnection network in microelectronic ICs. Before performing LFT, because the two p-n junctions are facing each other, only a leakage current in one of the two diodes exists and the device is essentially operating as an open circuit with an infinite resistance.

Irradiating in the gap region and the edge parts of the heavily boron doped regions by a focused visible laser beam, with a diameter of less than the width of heavily doped regions, induces a temperature increase of silicon and, finally, the melting of the irradiated crystalline Si. During the melting, due to the high diffusion coefficient in the

liquids, dopant atoms diffuse quickly from the heavily doped regions into the lightly doped gap region. After the laser beam is switched off, the liquid silicon freezes and re-solidifies, resulting in the diffused dopant atoms in a new local profile, thus creating a resistive link with a finite resistance between the highly doped regions. In order to avoid damaging adjacent devices and structures in microelectronic ICs and produce accurate LDRs with desired values and high quality, a careful control of processing parameters is necessary. These parameters involve the laser focused spot size, laser power, pulse duration, number of laser expositions and position of the laser spot relative to the gap, heavily doped regions and initial structures of the devices.
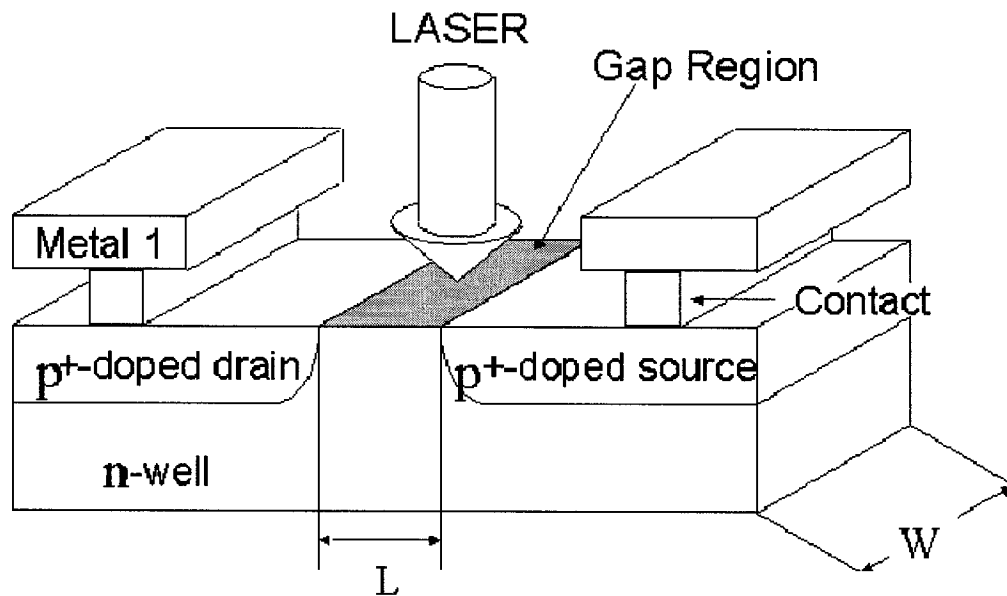
Fig. 1.1 Schematics of laser fine tuning technology.

In this study, all the initial devices before LFT were obtained and all the LDRs were fabricated at LTRIM technologies, Montreal. Those initial devices before LFT process are identical and contain multi-layers of dielectrics, including SiO_2, SiO_xN_y, and Si_3N_4, on silicon substrate, fabricated by conventional CMOS technology. The different contrast in the low magnification TEM image shown in Fig. 1.2 indicates different layer of dielectrics with different chemical components. The overall thickness of the dielectric layers is 8 μm. As shown Fig. 1.2, the two electrical contacts are about 7 μm far from

the gap area, where the laser beam will be focused; therefore, no heating effect on the contacts was caused by the laser heating. The thesis presents two types of LDRs, which are fabricated using initial flat and field effect devices. The difference between the two devices is from CMOS fabrication process. For the flat devices, the poly-Si gate was initial fabricated and, then, was etched after ion-implantation process, while, for filed effect devices, field oxide was produce in order to avoid implants injecting into the gap region.
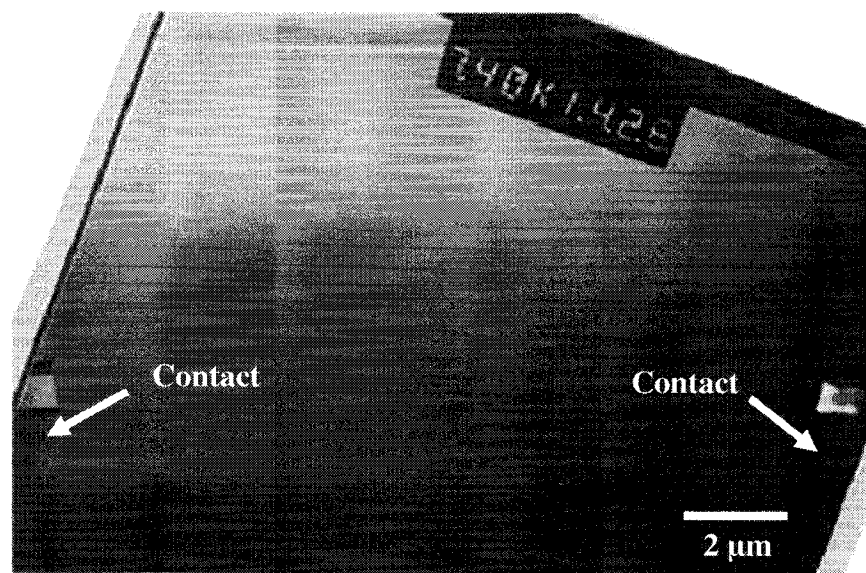
Fig. 1.2 Bright field TEM image showing the entire structure of an initial gateless field effect device used for LDR fabrication.

1.2. OBJECTIVES AND ORGANIZATION OF THE THESIS

The focus of this thesis is to obtain a complete microstructural characterizations and dopant distribution measurements of these microdevices fabricated by the LFT technology in order to fully understand the effects of the laser irradiation on the LDRs structures and the mechanisms of this focused laser processing incorporation with electrical behaviors and, the ultimate objectives are to use the information to completely control the electrical and material properties of the resulted microdevices, improve the

accuracy and long-term stability of the microdevices, and finally provide a modeling for incorporating LFT in industry. As shown in Fig. 1.3, it is important to know the dopant distribution in the LDRs in order to understand the LDRs' formation and the effects on resistance values. Due to the heating process of melting the silicon we could anticipate that the LDRs will contain defects which could affect the devices' characteristics. Actually, LDRs might be degraded by point defects (mainly interstitials and vacancies), dislocations, and impurities (mainly oxygen from the dielectrics) because they can provide energy level in the band gap of Si and strongly affect the electrical properties and long-term stability of the doped Si.

Laser processing parameters	**Dopant distributions and microstructure of LDRs**	**Electrical characteristics of LDRs**
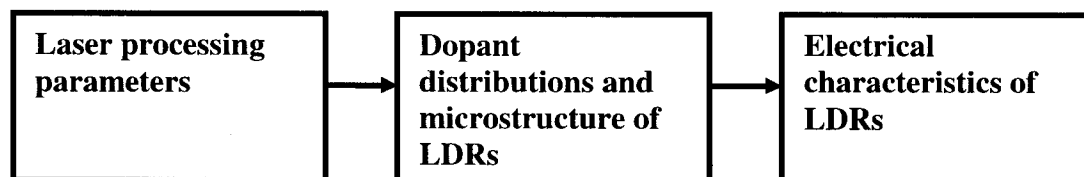
Fig. 1.3 Schematics of objectives of this thesis.

Because the cooling rate of the laser induced liquid might be very high due to the low temperature of the silicon substrate in the initial microdevices, point defect could be formed and should be investigated. The probability of thermal stress during laser irradiation and mismatch of atoms during regrowth from liquid Si might induce material cracks and/or dislocations. The temperature gradient can cause difference of surface tension at the dielectrics/liquid Si interface, thus creates liquid convention, introducing mass transportation other than "normal" dopant diffusion in the liquid Si. The laser energy might also be absorbed by the dielectrics, thus increasing the SiO_2 temperature, which could cause the breaking of oxygen-silicon bonds and the diffusion of oxygen atoms into the melted Si. However, all those phenomena take place in very small dimension of about 2 – 4 μm within the laser irradiated volume and high spatial resolution technique have to be used and adapted to obtain the microstructures and the dopant distributions in the LDRs. The two-dimensional (2D) evaluation of those characteristics has been performed by transmission electron microscopy (TEM), scanning electron microscopy (SEM), atomic force microscopy (AFM), scanning

capacitance microscopy (SCM), chemical etching process, and electrical measurement in combination with one dimensional (1D) technique such as secondary ion mass spectrometry (SIMS).

After this introduction chapter, this thesis consists of seven additional chapters. Chapter 2 contains a summary of prior research works related to the objectives of this study. Previous electrical characterizations and modeling for LDRs' formation, heat transportation and dopant diffusion are covered. The mechanism of the interaction between laser light and materials such as monocrystalline silicon is also briefly reviewed. This chapter also concludes with previous work on defects, including point defects, dislocations and so on, which can affect the electrical properties of the regrown materials following melting. Chapter 3 makes an overview of analytical techniques used for microstructural characterization, such as analyses of point defects, dislocations and volume defects, as well as dopant evaluation, including methods based on chemical reactions, electrical measurement, secondary ion mass spectroscopy and scanning electron microscopy.

Covering a significant aspect of this thesis, Chapter 4 presents an improved methodology for quantifying the dopant distribution, based on dopant-selective etching, transmission electron microscopy (TEM) and focused ion beam (FIB) technique. The technique can be used for any microelectronics devices, requiring to obtain high resolution dopant profiles. The two-dimensional (2-D) dopant distributions in LDRs were determined using the developed method and successfully compared with those calculated results, obtained by a thermodynamic and heat transfer model developed by our research group. This chapter had been accepted for publication by Journal of The Electrochemical Society in September 2005.

Chapter 5 presents two periodic structures, which are formed in silicon covered by SiO_2 due to the variation of oxygen concentration induced by O diffusion. Those periodic structures are produced under polarized laser irradiation with different laser intensity. At specific high intensity range ripples are created corresponding to melting of the entire laser irradiated region, while at specific low intensity range coexisting of solid

and liquid is induced. This chapter had been accepted for publication by Applied Physics A in October 2005.

Following our findings of the preceding chapter, Chapter 6, then, states the study of the creation and properties of submicron conductive links due to the coexisting of solid and liquid Si. This study was performed mainly by using scanning capacitance microscopy (SCM) and experimental results show that the resistivity increases and the net dopant concentration decreases when higher laser intensity or more laser pulses are used. Moreover, the number of conductive links depends only on the laser intensity, while the width of the links depends on both the laser intensity and the laser pulses. This chapter had been submitted to Journal of Applied Physics for publication in July 2005.

Chapter 7 presents a detailed microstructure characterization of with emphases on point defects, dislocations, and volume defects. The formation mechanisms of those defects are also suggested. In this chapter, the optimization strategy for producing high quality microdevices by finely focused laser irradiation is also proposed.

Finally, Chapter 8 presents the conclusions of this thesis and suggests recommendations for future experimental and modeling efforts in order to have further understanding or quantification of the physical behaviors in the LDRs fabricated by focused laser processing.

CHAPTER 2 LASER INDUCED SILICON MELTING AND ITS APPLICATION TO MICROELECTRONICS

In this chapter, an introduction to the fundamental interaction processes between light and matter is given and, then, the principle and modeling of the LFT technology are presented. Finally, the chapter ends with a discussion on the challenges that the new technology is faced with.

2.1 INTRODUCTION

Because lasers can directly act as energy sources, there are a number of phenomena, which can be caused, when laser irradiates on different materials. However, one important case is that the laser provides a high intensity source, from which the materials might be melted due to the interaction between light and materials [7 – 9]. Using pulsed laser, the facility of rapidly heating and then cooling surface layers without heating the bulk depends mainly on the laser intensity, pulse duration, number of the laser pulses. Some applications such as forming novel structures and alloys have been proposed based on this temporal and spatial control. For example, laser surface alloying is a technique which actually mixes the added constituents with the base material, forming a new alloy in the region that has been melted.

Another application, which has been widely studied, is laser annealing. The laser irradiation of Si can induce transient melting which leads to rapid recrystallization with very high (from 1 to 40 m/s) liquid/solid interface velocities, thus, recovering the crystal damage created during ion-implantation and trapping the dopants in the Si with concentration higher than its solid solubility. In this way, the "box-like" doping profile with ultrashallow junction can be obtained and the sheet resistivity of the doped Si can be very low, potentially satisfying the technology of the next generation CMOS devices.

Recently, this laser annealing technique was modified and used to melt the Si materials underneath the dielectrics with thickness of more than 6 µm in order to

fabricate LDRs with high accuracy. This technique is the LFT based on initial structures that are fabricated using commercial CMOS flow. In the LDRs, the regrown Si materials are in crystalline phase.

2.2. LASER INDUCED HEATING OF MATERIALS.

Various lasers, ranging from infrared to UV and from femtosecond pulse to cw, can interact with materials giving rise to a complex phenomenon -- a photon absorption and energy dissipation. The absorbed light is not directly converted into heat, but into excess distributed energy between the excitation energy for the bound electrons, the kinetic energy of free carriers and the excess of phonons. The transformation of the laser energy into heat mainly takes place in three steps: (i) Spatial and temporal randomization of the motion of the particles by collisions during the laser irradiation, until they reach a thermal equilibrium; (ii) Energy transfer to the materials involving a large number of mechanisms, each of them with its own time constant; however, they can be described by an overall energy relaxation time depending on the material and the laser intensity; (iii) Heat flow towards cooler system, e.g. substrate. The temperature distribution induced by laser irradiation can be calculated by using the classical heat equation given by

$$\rho(T)c_p(T)\frac{\partial T}{\partial t} = \nabla[k(T)\nabla T] + Q(T) + L(T),$$

where L(T) is the material's latent melting heat. While the source term Q is zero in the transparent layer over the substrate. In the absorbing solids, $Q(R,\alpha,I,z,t)$ depends on both material and laser parameters, as shown below

$$Q = I(R,t)f(z,\alpha)$$

where $f(z,\alpha)$ describes the absorption of the laser light along the z-direction and α is the optical absorption coefficient which depends on laser wavelength λ.

We can assume that the heat is produced due to the absorption over a length $1/\alpha$ and diffuses approximately, during the pulse duration t_p, over a length L_{th}:

$$L_{th} = 2\sqrt{k\ t_p}$$

where k denotes the thermal diffusivity of the substrate materials.

The surface temperature at the end of the laser pulse can be calculated by [9]:

$$T \cong 1.13 \cdot F \cdot (1-R) \cdot \frac{\sqrt{k t_p}}{\rho C_p}, \qquad \text{(when } 1/\alpha << L_{th})$$

$$T \cong \alpha \cdot F \cdot (1-R) \cdot \frac{1}{\rho C_p}, \qquad \text{(when } 1/\alpha >> L_{th})$$

where F is the laser fluence, C_p the heat capacity, R the reflectivity, ρ the mass density.

Some very illustrative calculations of normalized temperature distribution, in a semi-infinite solid, as a function of normalized depth at the end of laser pulse are given in the Fig. 2.1 [9]. The numbers indicate the ratio (ξ) of the absorption length $1/\alpha$ to the thermal diffusion length L_{th}. These profiles are obtained by assuming a uniform heat source is used. As we can see, there are two extreme cases of ξ (0 or 1), indicating the significant differences between the resulting temperature profiles at the surface layer of the materials. In the first case ($\xi \rightarrow 0$, $1/\alpha << L_{th}$), the exponential absorption profile induces an entirely exponential temperature profile with an relatively high surface temperature, of which almost no heat flow during the pulse duration. In the second case ($\xi \rightarrow 1$), a Gaussian temperature profile with a relatively low surface temperature is caused due to heat conduction into the bulk, which minimizes the temperature gradients at the surface.

The structure heated by laser can be insulators, crystalline semiconductors, and metals. Energy of visible light absorbed by insulators is negligible except when defects become important. For metals, laser can heat the materials due to interaction between phonons and free electrons after considering reflectivity. Furthermore, the heating of crystalline semiconductor could lead to material modification, phase transformation and melting. Although laser induced heating of materials, including semiconductors, does not necessarily show melting, the laser induced heating is widely employed in various

applications such as material alloy and laser annealing. Almost all semiconductors act as metals, when it is in liquid state, with very high thermal and electrical conductivities.

$$\xi = \frac{1}{\alpha \, L_{th}}$$
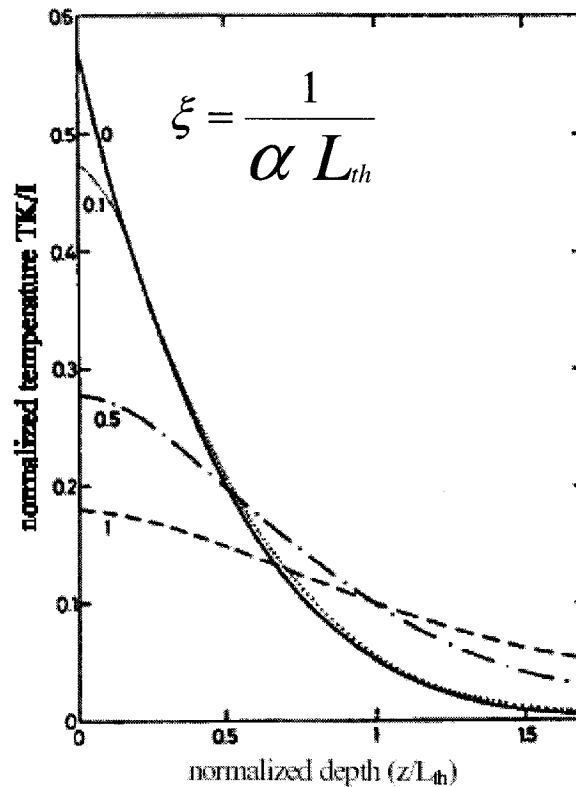
Fig. 2.1. Normalized temperature depth distributions for a laser irradiation as a function of normalized depth [9].

2.3. LASER INDUCED SILICON MELTING

2.3.1. MELTING DUE TO LASER IRRADIATION

A surface and bulk modification is observed when the Si material is heated to melting temperature and, then, rapidly re-solidified, driven by the large thermal gradient. The material modification is mostly due to the unique properties of atomic liquids such as high atomic mobility and (or) solubility, which enables microstructures that are not accessible through pure solid-state reactions.

Laser irradiation can also induce phase transformation with the same chemical components of the materials. Heating from the laser irradiation provides a thermal budget for diffusion and electrical activation of dopants. For example, materials can be transferred to their amorphous state from monocrystalline and polycrystalline states by means of laser irradiation with high intensity [10 – 12]. This can be achieved by ultrarapid re-solidification following laser-induced melting, which is usually referred to a quenching process with high cooling rates. Irradiation with nanosecond pulses leads to cooling rates, which are much shorter than $\sim 10^{10}$ K/s [13]. These cooling rates depend directly on the laser intensity, the pulse duration, the number of laser pulses, the temperature of the substrate, the impurities of the materials, and the thermal conductivity of the solid materials in contact with the liquid [9] [17].

Another application of laser induced melting is laser annealing after ion-implantation. Ion-implantation for doping of monocrystalline and polycrystalline Si usually induces a large amount of atomic disorder in the crystalline structure of the surface layer. Furnace annealing and rapid thermal annealing (RTA) are often employed to recover crystallinity. However, under laser irradiation with short pulses [10] [14], boxlike doped crystalline Si with uniform dopant distribution and without defects such as dislocations are obtained in a much shorter time because the atoms of each chemical component are highly mobile and, then, distribute uniformly. Previous TEM results [15] show that the defect density after a cw (continuous wave) melt laser annealing is extremely decreased when compared to conventional furnace annealing. The typical size of laser beam used in laser annealing is approximately 50 – 100 μm in diameter.

2.3.2. MELTING OF SI COVERED BY SIO₂ DUE TO LASER IRRADIATION

The laser induced melting of silicon materials, covered by SiO_2, is directly related to the formation of LDRs, studied in this thesis. Degorce et al. in our research group extensively studied the melting and solidification with this specific structure [18]. In their modeling and experimental measurements, they used a new three-dimensional transient temperature field model (TTFM), which considers the laser induced melting as out-of-equilibrium heating. This model includes heat absorption, heat transformation in the bilayer device (Si dioxide and Si substrate), and phase change to determine the relationship between the interface velocity and temperature. By considering the SiO_2 with 0.5 µ m thick and the laser intensity with Gaussian distribution, Fig. 2.2 shows the transient temperature, as a function of time, of the center point and those at r = 0.5 and 1
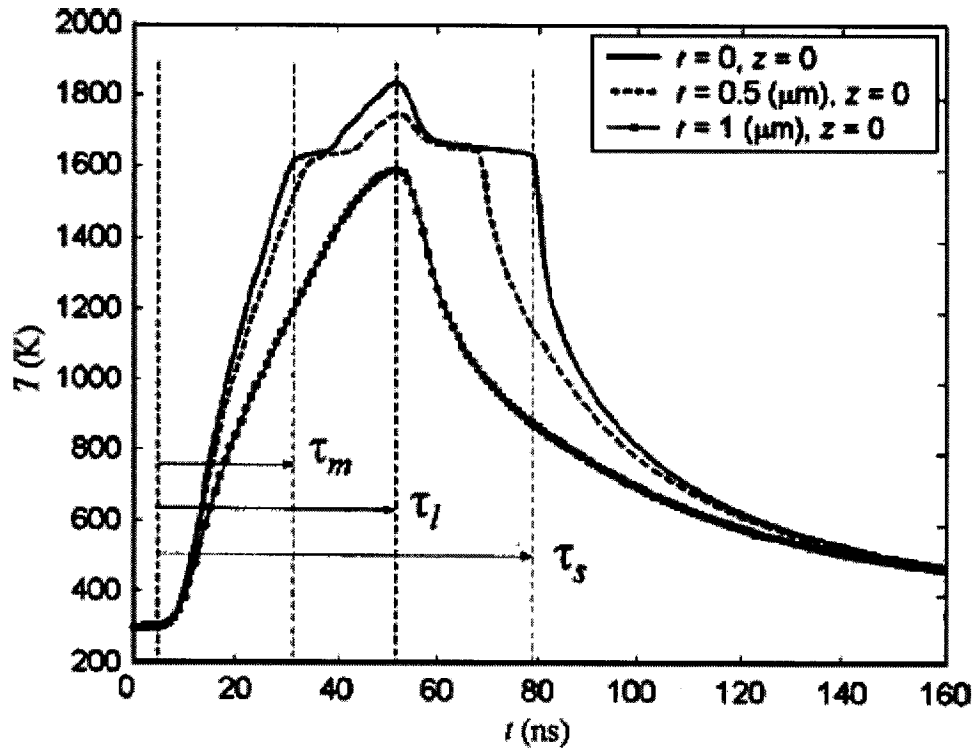
Fig. 2.2. Temperature at the center point (r=0, z=0) and two other points (r = 0.5 and 1 µ m) on the surface [18].

μ m at the Si surface. The plateau is at $t_{melting}$ of 1690 K of pure Si material. The maximum of the laser intensity is 1.35×10^7 W/cm^2, the laser beam radius is 0.85 μ m, and the pulse duration is 40 ns. When the laser intensity becomes large, the maximum temperature in the liquid silicon could be higher than the melting temperature of SiO$_2$, yielding to oxygen inter-diffusion and the lost of the SiO$_2$/Si interface. In this case, it is important to point out that the melting points of the silicon crystal and silicon dioxide varies with the oxygen content as shown in the phase diagram in Fig. 2.3 [39]. The melting point of SiO$_2$ decreases when oxygen atoms are lost and, on the other hand, the melting point of Si also decreases when oxygen atoms are added. This will also affect the dopant diffusion behavior under laser irradiation because of the significant difference of diffusivities between solid and liquid.

Fig. 2.4 shows the spatial evolution of the liquid/solid interface velocity (v_{sl}) in the radial (r) and vertical (z) directions of the melted zone. The interface velocity and interface temperature (T_{int}) are almost constant during solidification stage. Moreover, the

OXYGEN CONTENT [%]
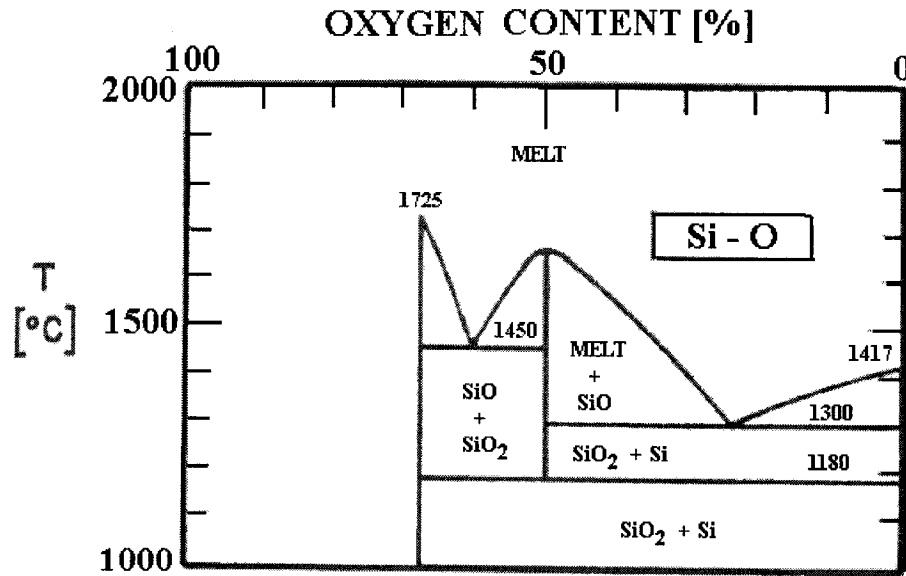
Fig. 2.3. Phase diagram of Si-O, indicating the melting point variation of crystalline silicon and silicon oxide [39].

velocity in the radial direction is much higher than that in the vertical (b) directions.
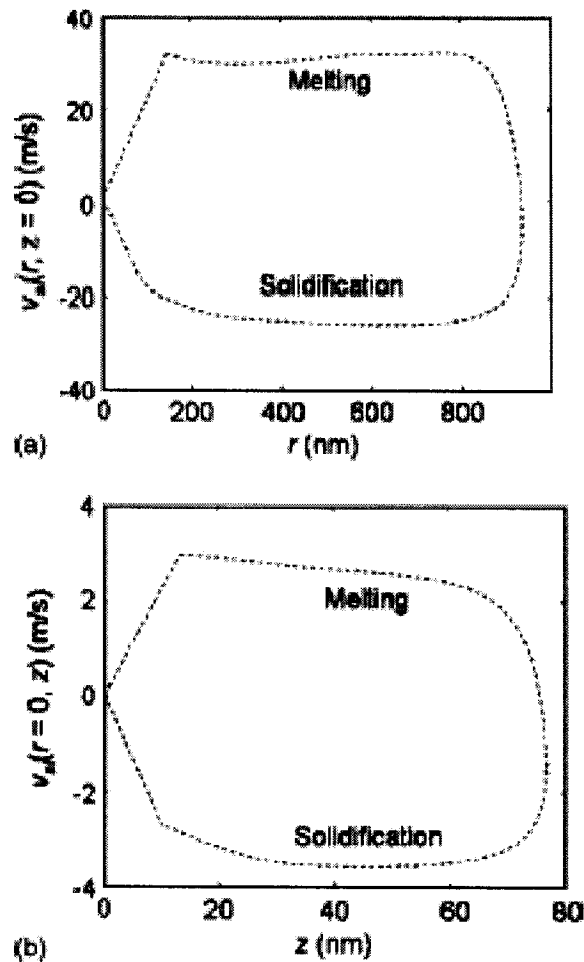
Fig. 2.4 Interface velocity during melting (upper part) and sodification stages (lower part) versus position in the radial (a) and vertical (b) directions.

2.3.3. DEFECTS DUE TO LASER IRRADIATION

Defect formation: Based on previous studies of grown Si by Czochralski technique, it is known if the growth rate of silicon from liquid is slow enough to maintain thermodynamic equilibrium; the excess defects could be minimized and dopant distribution could be more uniform and/or stable, either by coming out of the material surface or, in some cases, by forming solid precipitates in the crystals. However, real crystals mostly differ from the ideal ones because they possess imperfections or defects [22]. Some undesirable imperfections in regrown silicon, including formations of three-

dimensional (3-D) defects [23 – 24], such as impurity precipitates and voids, two-dimensional (2-D) defects [22] [25], such as stacking faults, twins, grain boundaries, one-dimensional (1-D) defects [26 – 27], such as threading dislocations and dislocation loops, zero-dimensional (0-D) defects [28 – 29], such as point defects (vacancies and interstitials) and diffused impurities, have been extensively studied from early days.

One important 3-D defect is impurity, including dopant and clusters. At high ion implantation doses the peak of the implanted boron profile becomes immobile [30] as well as electrically inactive [31]. For example, although the actual atomic structure of these clusters is not well-known, they are assumed to by compose of components of B_nSi_m, where n, m denote the number of atoms in the clusters (n, m < 5). Pelaz et al. [32 – 33] suggested that only small boron clusters are stable, and also found that the Si interstitial supersaturation is a prerequisite for boron clustering. The boron atoms can be released by following dissociation reaction that some thermally generated silicon interstitials interact with the cluster.

Threading dislocations, a major type of 1-D defects existing in silicon, are formed to degrade the physical properties of micro-devices. The initial dislocations have strong interaction with point defects, impurities and other defect because various defects distribute near and at dislocations [34 – 37] [40]. Szabo [38] observed the occurrence of cracking and defects during Czochralski growth due to inhomogeneous temperature yielding to stress fields.

Similar to grown Si by Czochralski technique, regrown silicon materials by laser induced melting with large beam, greater than several millimeters, also contain different defects, including 0-D defects [28 – 29], 1-D defects [26 – 27], 2-D defects [22] [25], and 3-D defects [23 – 24]. Dislocations, created by laser melting, were widely studied previously. Kaki et al. [46] indicated that in order to restrict the generations of grain boundaries as well as dislocations, it is necessary to control the temperature profile in both the liquid Si and growing film so that the random nucleation is reduced and the solidification direction of the molten Si is unified. However, the defect density can be minimized by modifying the laser system or sample structures [47 –53]. For example, a

new method was developed to suppress defect formation as a result of reduction of solidification rate of the top silicon layer by laser-irradiating the bottom Si layer of the structure of Si/SiO$_2$/Si/glass [50].

When silicon is heated to an elevated temperature by a laser beam, it can cool down rapidly, e.g. 10^{10} K/s, so that most defect could be frozen, yielding to a defect concentration exceeding their thermodynamic equilibrium. Therefore, the defects and (or dopants) in the grown materials by laser melting technique, can, and often do, exceed the solid solubility. As Cullis [54] expected, annealing by laser irradiation with substantially high energy densities could completely dissolve the damage caused by ion-implantation and, thus, eliminate all extended defects of the re-crystallized layer. However, the extremely high re-solidification rate (often > 2 msec^{-1}) toward the end of the laser annealing cycle caused the formation of non-equilibrium solid solutions. Point defects with very high concentrations were trapped in the quenched, re-crystallized surface layer. Using TEM (transmission electron microscopy), Cullis et al. [21] observed microtwin and occasional dislocation pairs extending up to the sample surface from a buried irregular band of point defect clusters in the regrown silicon by laser irradiation technique. Foti and Rimini [55] argued that laser irradiation on ion-implanted silicon produced a large variety of defects, especially dislocations with line length from 2000 to 4000 Å and volume density of 5×10^8 cm/cm^3. Nipoti et al. [56] demonstrated that after laser irradiation, point defects of vacancy type, which were found by double-crystal X-ray diffraction (DCD), were responsible for the lattice distortion. Those point defects with a rather high density were also suggested to be generated by the fast quenching rate at the end of the laser pulse, almost irrespective of the ambient to which the wafer surface is exposed. Moreover, the crystalline silicon after laser irradiation might also be amorphized if the re-solidification process is too fast to form perfect monocrystalline and polycrystalline states.

Electrical properties of defects in silicon: Almost all defects, including dopants, can provide energy levels in the forbidden gap of silicon. For example, some impurities,

existing in silicon and SiO_2, such as oxygen atoms can also act as donors, acceptors, and (or) deep levels, as shown in Fig. 2.5. The levels below the gap center are measured from the top of the valence band and are acceptor levels. The levels above the gap center are measured from the bottom of the conduction level band and are donor levels unless
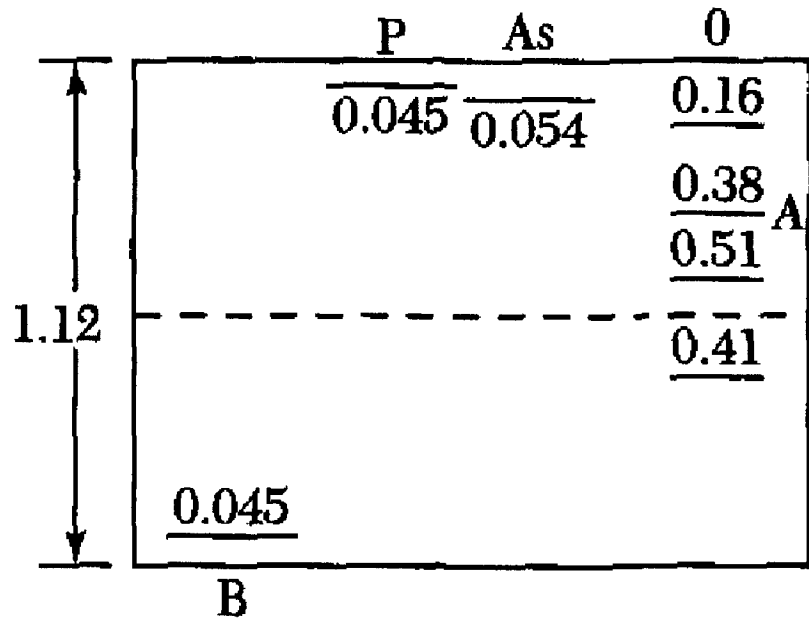
Fig. 2.5 Ionization energies (in eV) for various impurities in silicon.

indicated by A for acceptor level [41]. As we can notice here, O atoms can provide several energy levels; however, O atoms in silicon after rapid cooling, following laser irradiation, mostly act as donor.

Except dopant atoms, which are absolutely necessary for creating devices, most crystalline defects are harmful, regardless of the density in which they may exist in any micro-devices. For example, a space-charge layer can be induced at the dislocations under electrically biased or non-biased conditions. Christiansen et al. showed that the dislocation network, which existed in laser re-crystallized silicon materials [58], frequently affect the electronic levels in the band gap and, thus, lead to electrical activity in terms of minority carrier recombination and potential barriers [59].

Other imperfections are mainly elementary lattice defects that affect electrical activity of the dopants and modify other electrical properties of the devices and materials. They consist of native defects (vacancies, self-interstitials and their agglomerates), complexes of dopant atoms and native defects, and other impurity atoms. It was suggested that a plastic deformation of silicon [60], due to laser irradiation, led to a formation of donor and acceptor states, an inversion of conductivity type in n-Si, and a formation p-n junction at dislocations under an n-Si indentation. These phenomena might be caused by a collection of impurities or Si dangling bonds. The vacancies and self-interstitials in silicon regrown by laser melting can provide various charge states [61 – 62]. It was stated that both boron-vacancy and boron-interstitial complexes are also able to trap electrons at the gap levels [63 – 64], which are unstable at room temperature.

Cervera et al [65] pointed out that lattice defect and deep centres [66], which were created by laser melting under certain conditions, causes a worsening of the electrical characteristics of the devices. Moreover, if the oxygen concentration in the liquid is high, some oxygen atoms in c-Si grown at any rate can be electrically activated after laser annealing process. Some researcher suggested that heating, by thermal annealing or laser irradiation, at 400 ~ 450 ^{0}C increases oxygen donors [67 – 69]. In order to deactivate oxygen-related charge centers, a high-temperature treatment, such as RTA annealing at 1000 °C for 10s [70], is necessary. Mada et al. [68] concluded that high concentration defect-related donor states can be generated during laser annealing of p-type silicon with surface melting. These donors were suggested to be created by electrically activating the oxygen atoms.

Stability effect due to defects: As experimentally verified by Yakimov [34], the electrical and optical activity of so-called "clean dislocation" can be very low but increase when the interaction between dislocation and point defects occurs under the plastic deformation, subsequent annealing, and/or electrical stress. Therefore, the dislocation influence on the semiconductor properties and device performances is mainly controlled by the redistribution and/or reconstruction of pre-existing point

defects and by the reconstruction of dislocations themselves as a result of dislocation-point defect interactions. Maroudas et al. [43] suggested that the dislocation core can be assumed to be a perfect sink for the impurity atoms in many circumstances, thus, the resistivity can be changed during thermal or electrical stress due to the migrations of impurities into the dislocations by diffusion or drift, respectively. Furthermore, the migration of impurities to dislocations, decorating the dislocation cores, also leads to the formation of point defects, which could be traps to the majority carriers.

Saarinen et al. [44] mentioned that vacancy, interstitial and point defect-related complexes are elementary deep centers in silicon materials. For example, according to the study of Watkins [45], both the monovacancy and interstitial atoms are mobile even at low temperatures below 150 K. The complexes, such as divacancies (V_2), vacancy–oxygen (V–O) pairs (A-centres) and vacancy–donor impurity pairs (E-centres), are formed by the migration of the elementary vacancy defects surviving at room temperature. Moreover, for regrown Si by small focused laser beam, one potential problem, which can be caused by a non-uniform temperature profile due to Gaussian distribution of the light intensity, is that a number of regrowth velocities across the beam may induce different types of defects, causing instability of electrical properties of the fabricated devices.

2.4 LASER FINE TUNING

The laser processing technique used here involves two possible steps, which are laser fine tuning (LFT) and non-melting annealing by laser irradiation.

2.4.1 PRINCIPLE

Fig. 2.6 shows the structure of a MOSFET, consisting of a lightly doped n-well and two heavily doped p-type regions, namely source and drain, formed by ion implantation and thermal annealing. As shown in Fig. 1.1 above, the structure used in LFT is gateless MOSFET in order to avoid energy absorption due to conventional poly-
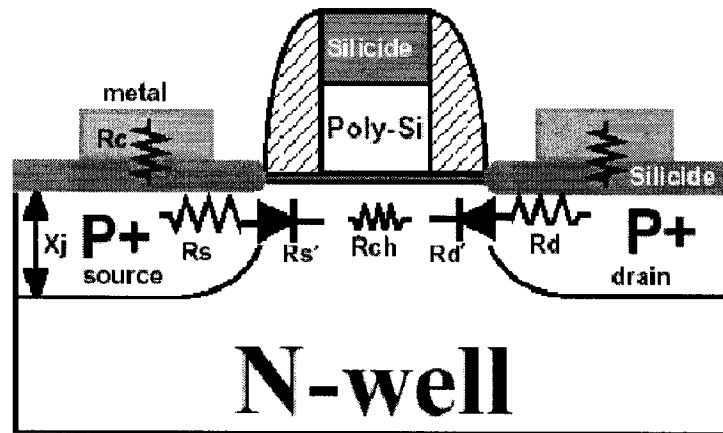
Fig. 2.6. The structure of a MOSFET with an n-well and heavily implanted source and drain.

Si gate. Fig. 2.7 shows a typical initial gateless structure, indicating the components for the overall resistance. The schematics of the laser fine tuning (LFT) [3] process, for fabricating highly accurate resistor, under laser irradiation is shown in Fig. 2.8. N-type or p-type resistors can be fabricated, depending on the original dopant concentration of the source/drain and laser processing parameters, and any desired resistance values can achieve by controlling the laser parameters.

Before the LFT process, the total resistance (R) is the sum of nominal channel resistance (R_{ch}), two additional resistances (R_s and R_d), and junction resistance (R_{jun}), involving pn/np junction resistances ($R_{jun}=R_{d'}+R_{s'}$). Because the two pn/np junctions, namely $R_{d'}$ and $R_{s'}$, are in series, the current between the source and the drain, which is
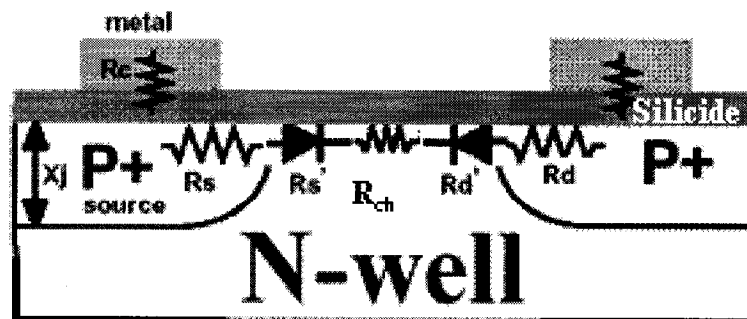
Fig. 2.7. Gateless structure for LFT, showing the components for the overall resistance value.

caused due to current leakage, is very small. That is to say, the total resistance is very high and the device can be considered as an open circuit.
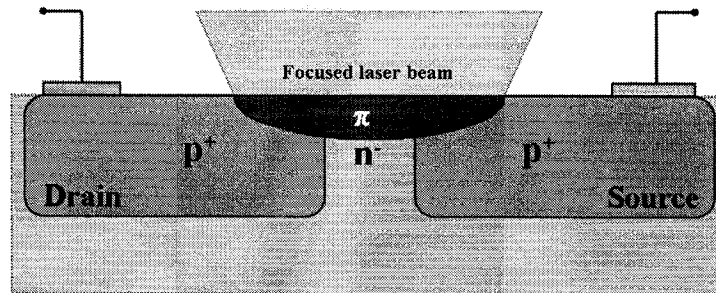
Fig. 2.8 Schematics of LFT process.

As introduced by Meunier et al [3], the irradiation by a focused laser beam on the lightly n-doped gap and partial volumes of highly p-doped source/drain regions causes the silicon to melt, driving the p-type dopants from the source and drain into the gap region. Following the melting, the liquid silicon re-solidifies to form dopant redistributed volume. Since the p-type dopant concentrations in the nominal source and drain regions are much higher than the n-type dopant concentration in the gap, this region between the two heavily doped regions becomes p-type doped and the pn junctions disappear, forming a resistive link with a finite resistance value. Thus, the obtained LDR can be sketched with an equivalent DC circuit as shown in Fig 2.9. However, the dopant concentration in the resistive link is still lower than the concentrations in the source and drain regions, therefore, the total resistance is totally dominated by the resistance of the doped gap. The resistors with desired value could be fabricated by strictly controlling the processing parameters such as the laser spot size, the pulse duration, the laser power, the number of laser expositions, and the position of the laser spot relative to the device.
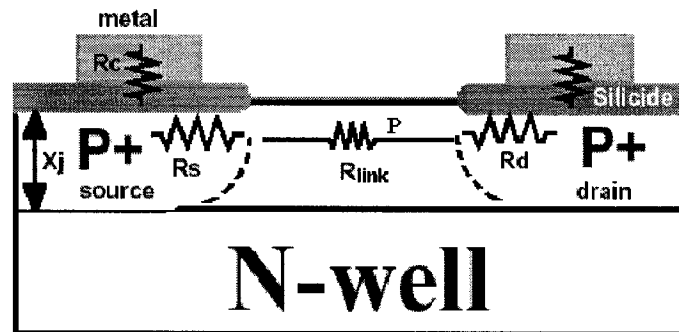
Fig. 2.9 Link fabricated using laser trimming.

The LFT system (Fig. 2.10) has been described previously [16]. The energy source for melting silicon is a Spectra Physics Millenia Doubled ND:YAG with a power of 10 W. A Neos Technologies acousto-optic modulator, controlled by a Hewlett Packard 81101A pulse generator for providing the modulation signal, is employed as a high-speed shutter. A microscope objective made by Mitutoyo focuses the laser beam on the device gap to a 2 ~ 4 μm spot in diameter. Three-dimensional (3-D) device position
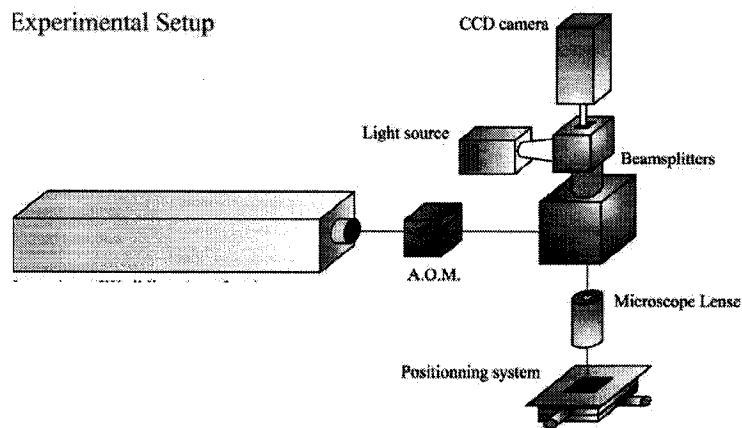
Fig. 2.10 Schematic setup of the LFT system.

relative to the laser beam is adjusted on a ASL AVLIIZ X-Y-Z positioning table, made by Aerotech Inc., with a stacking of 3 stepping motor translation stages. The horizontal X and Y-axis translations with resolutions of 20 nm provide precisely device motion normal to the incident laser beam, and the vertical motion with 50 nm resolution is

performed by the Z-axis positioning function. Real-time observation of the device on the finely tuned microdevices is allowed with a Hitachi CCD camera through a mirror, which can be removed during laser irradiation. A high-speed computer controls the entire laser process procedure.

However, it should be mentioned that the crystalline silicon melts at approximately 300 K lower than that of silicon dioxide (SiO_2). The laser intensity in the LFT should be controlled and utilizes this melting point difference to establish a processing window. As the laser intensity is increased, a threshold, at which not only the silicon becomes melted but also the silicon dioxide becomes melted, is reached

2.4.2 ELECTRICAL CHARACTERISTICS OF LDRS

The electrical properties of the LDRs are mainly determined by the doping distributions in the laser-created resistive links in the devices. All the dopants, following laser-induced melting, can be assumed to be completely activated. Because the diffusion coefficient of dopants in liquid Si [D_{Boron} = 3.3±0.4×10^{-4} cm^2/s; $D_{Arsenic}$ = 3.3x10^{-4}cm^2/s [20]] is almost seven orders of magnitude higher than that in crystalline Si [10] [107], it can be assumed that the dopants are only driven into the melted silicon region, while the dopants are immobile (D_{solid} < 10^{-12} cm^2/s)in the solid region and, thus, only a rapid dopant redistribution in liquid silicon is induced. For example, to a typical pulsing time of 200 ns, dopant diffusion distance is ~ 1.6 nm in liquid Si and is less than 0.03 nm in solid Si based on estimation according to $2\sqrt{Dt}$. Therefore, only the region within the maximum melted depth has to be considered for the calculation of temperature variation and dopant redistribution. The maximum melted volume can be calculated by solving the basic energy balance equations, involving the laser source, the heat conduction of the liquid and solids, liquid convection as well as light reflection.

For more accurate evaluation, the final doping level after the last laser irradiation can be calculated by considering not only the melting time of the local Si materials and the liquid temperature but also the initial dopant profiles in the heavily doped regions

and the initial structure of the devices. By considering the three-dimensional out-of-equilibrium transient temperature field (T(r,t)) [18], more accurate melting time and liquid temperature can be evaluated, as shown in Section 2.3.1. In this model, the phenomena of superheating and undercooling were considered. Then, basically using Fick's law $\partial C/\partial t = -D\nabla C$, the accurate dopant profile in the resistive link can be obtained. In addition, dopant distribution in the resistive links may also be affected by segregation if the growth velocity is low enough [42]. However, it is not important in our case because the dopants are B, As and P and the cooling rates are very high. Further factor, which should be considered on electrical properties of the LDRs, is the oxygen concentration in the regrown Si, diffused from the dielectrics, because the electrically activated oxygen atoms act as donors. In principle, the regrown Si material with higher net dopant concentration after impurity compensation has a lower resistivity, indicating that more dopants diffused from heavily doped regions into the gap region and, thus, inducing lower resistance value of the device.

The electrical performances of LDRs were previously measured [5] [16]. The I-V (current-voltage) curves (Fig. 2.11) show that the processed microdevices have linear characteristics at lower applied voltages, in good agreement with low-field carrier transportation described by the ideal ohmic relation. At intermediate voltages, I-V curves show sub-linear performances because of carrier mobility saturation, while at high voltages the current increases probably following the phenomenon of avalanche effect (Fig. 2.12). In principle, these experimental characteristics, described by I-V curves, can be interpreted starting from the 3-D distributions of electron and hole concentrations related to the obtained dopant distribution.
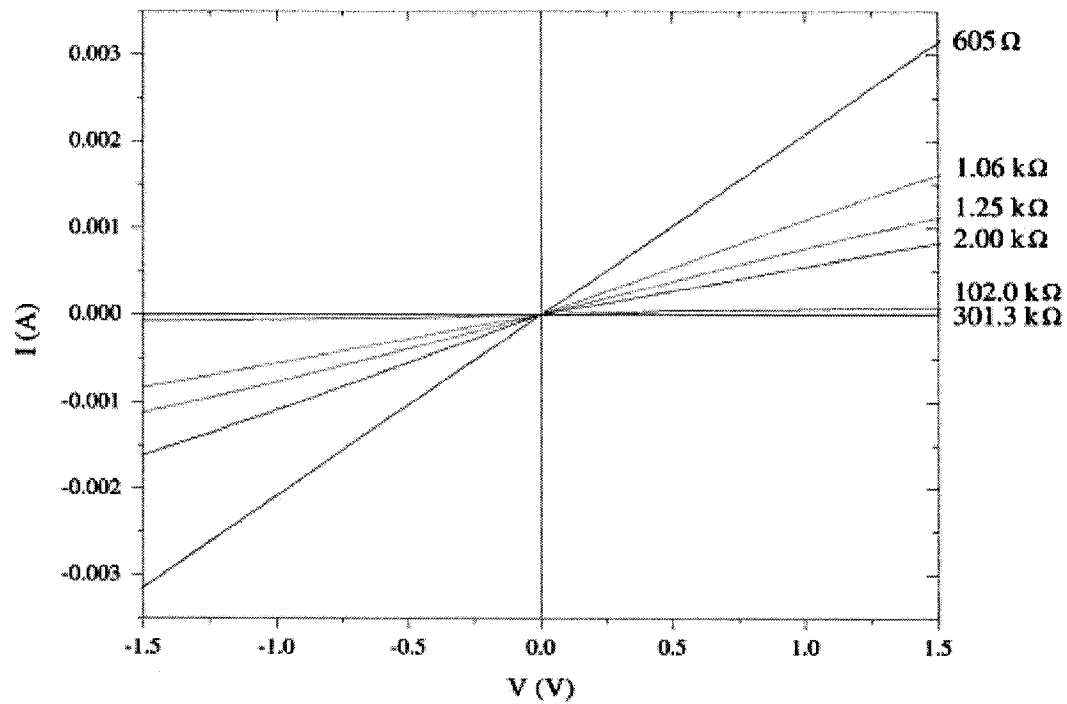
Fig. 2.11 I-V characteristics at low applied voltages.

2.4.3 DOPANT PROFILING AND STRUCTURAL CHARACTERIZATION OF LDRS

As shown above, studies on instrumental setup, laser trimming process, electrical behavior and modeling, and laser processing modeling have been carried out during many years in our research group. However, the dopant distributions and the microsctructures of the LDRs, related to the laser processing conditions, determine the electrical characteristics and short/long term stabilities. These various relationships are shown schematically in Fig. 2.13.

As described above, the dopant distribution highly determines the electrical properties. Unfortunately, the only results done previously on dopant distribution of laser diffused links was performed by Cohen et al. [222], who estimated the 1-D dopant profile along "source-link-drain" direction by simulation based on the consideration of dopant diffusivity in the melt as a function of the temperature. Up to now, no
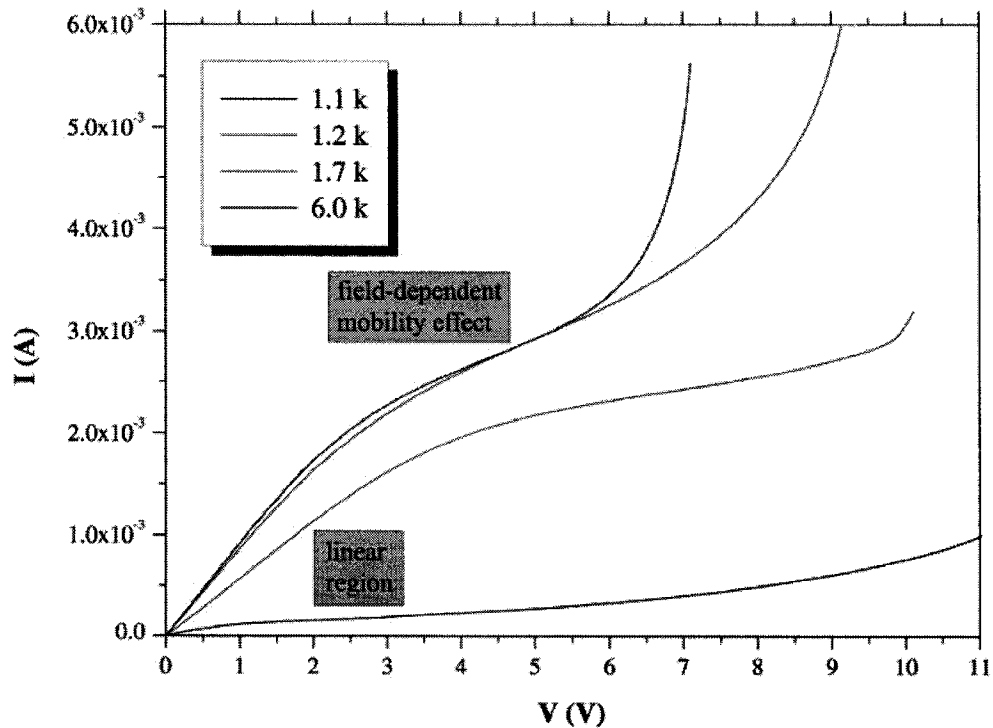
Fig. 2.12 IV characteristics at higher voltages.

experimental data are available to show the status of dopant profile in LDRs based on LFT processing. In fact, the actual dopant distribution in the devices might not be uniform, determining the current path under electrical potential.

Moreover, the quality of the regrown Si under laser-induced annealing with large beam size had been studied previously. However, the status of the regrown Si under laser-induced melting with focused beam, which is used in LFT technique, could be very different and has never been studied. The defect type and density might also be different from those of the former one due to the smaller thermal budget and the smaller area of liquid/solid interface. On the other hand, interdiffusion between dielectrics and silicon, which does not exist in the conventional laser annealing process, may happen in the case of the gateless MOSFET structures, which is used for fabricating LDRs. Therefore, silicon atoms and dopants in the melt could diffuse into the dielectrics as well as oxygen atoms in the dielectric multilayers could diffuse into the melting pool. As far as we know, no results have been obtained on the microstructure of regrown Si formed by LFT

with a focused laser spot less than 10 μm. Even in the simulation of Cohen et al. [222], the ideal crystal in LFT after laser melting was assumed. Therefore, the properties such

```
┌─────────────────────┐         ┌─────────────────────┐
│ Dopant distributions│◄═══════►│Electrical characteristics│
│ and microstructures │         │   and stabilities   │
└─────────────────────┘         └─────────────────────┘
          ▲                                │
          ║           ╱                    ▼
          ▼         ╱                ┌─────────────────────┐
┌─────────────────────┐             │ Device applications │
│Laser-process conditions├──────────►│    in industry      │
└─────────────────────┘             └─────────────────────┘
```
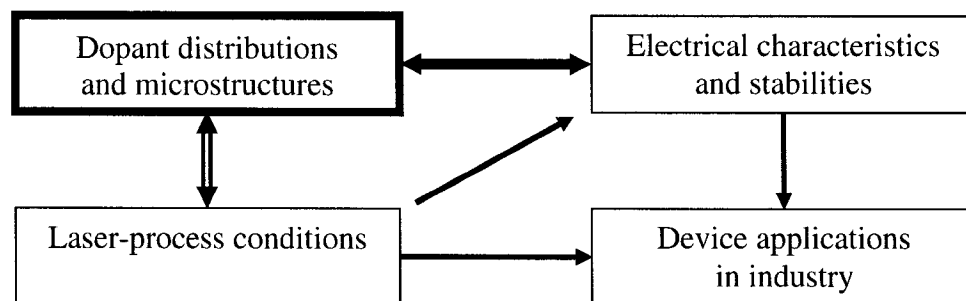
Fig. 2.13. Diagram of relationship between the study and the
other researches/applications.

as imperfections, including 0-D, 1-D, 2-D and 3-D defects, should be evaluated in order to completely control and improve the tuning accuracy and short/long-term stabilities for modern IC industry applications.

As a summary, wee have to understand the questions following: (i) how the focused laser beam does physically interact with the microdevices, (ii) what is the dopant diffusion behavior related to the laser irradiation, and (iii) what is the relationship between the electrical properties of the LDRs and the irradiation conditions. In the study presented in this thesis, microstructures in the processed devices, including dopant distributions and status of defects, in comparison with the initial devices, are characterized by using some typical analytical techniques covered in the next chapter.

CHAPTER 3. OVERVIEW OF ANALYTICAL TECHNIQUES FOR DOPANT EVALUATION AND STRUCTURAL CHARACTERIZATION

3.1. STRUCTURAL CHARACTERIZATION

Several techniques are used to obtain the microstructure of microelectronics devices, especially for characterizing lattice defects in silicon crystal. These techniques can be categorized as destructive and non-destructive methods [71]. The destructive techniques involve techniques such as transmission electron microscopy (TEM) and scanning electron microscopy (SEM). The non-destructive methods are namely capacitance-voltage, X-ray topography (XPT), and backscattering techniques.

TEM and SEM give very detailed information on defects such as dislocations and precipitates due to their high spatial resolution, although those analysis processes are extremely time-consuming and high-priced. A projection of defects in wafer scale could be given by an XPT imaging, which is relatively fast because the processing time is only in the order of hours. For example, McNally et al. [108] used synchrotron X-ray topography to study the quality of 200 mm diameter epitaxial silicon wafer for 0.25 μm CMOS technology by monitoring the presence of oxygen-related defects and dopant strain homogeneity. Small angle neutron scattering (SANS) is employed to provide information about the average size, form and density of lattice defects. Chemical etching technique, scanning capacitance microscopy (SCM) and deep-level transient spectroscopy (DLTS) are also important methods for characterizing the Si crystal quality. However, it should be pointed out that most of the available defect characterization techniques, especially point defects, are not direct but can only provide information about the manifestation of an interaction between the object of the measurement and some externally input stimulus [72].

3.1.1. POINT DEFECT EVALUATION

The presence of point defects [28] in the crystal significantly alters the electrical behaviors of the semiconductor materials and devices by distorting the electronic potential and, then, resulting in the introduction of energy levels into the "forbidden" band gap. Typically, those defects can be separated into two categories: native point defects and impurity-related defects. Native point defects, including vacancy, interstitial, and interstitialcy, exist in the pure and doped silicon lattices. The vacancy is an empty lattice site, while the interstitial, also called self-interstitial, is a silicon atom located in an interstitial position. An interstitialcy is composed of two atoms in non-substitutional positions configured about a single substitutional lattice site. The defect energy levels are normally categorized as either shallow or deep. In the case of silicon, shallow energy levels are introduced by doping the crystal with atoms from group III or group V of the periodic table. These dopants mainly occupy substitutional positions in the silicon lattice by forming covalent bonds with the four or three neighboring host atoms. Dopants from group V, such as phosphorous with ionization energy 0.044 eV, and group III, such as boron with ionization energy 0.046 eV, act as donors (n-type) and acceptors (p-type), respectively. Other defects form a much stronger electronic potential that binds the carriers more effectively. Those deep level defects (or traps) introduce energy levels deeper in the band gap. Unlike shallow dopants, deep level defects can be normally present in more than two charge states. In thermodynamic equilibrium, the exchange of electrons between the deep level and the conduction band and the exchange of holes between the deep level and the valence band are both balanced.

Direct observation of vacancy or interstitial properties is difficult. Recently, the positron annihilation experiment technique in silicon has been applied to study those native point defects in semiconductors [73 – 76]. While only vacancies were observed at temperatures greater than 1100 K via positron lifetime measurements [77], interstitials cannot be observed by this technique. The aligned Rutherford backscattering spectrometry (RBS) [78] are able to determine the concentration of self-interstitials only

if it is very high. Therefore, several indirect measurement techniques for point-defect parameters have been developed. For example, the presence of vacancies and interstitials in silicon have been confirmed indirectly [57] by the study of the behaviours of dopant diffusion and silicon self-diffusion. Dopants in silicon crystal diffuse via point defects and provide a method to study point-defect parameters like diffusivity, equilibrium concentrations and interface recombination velocity. Nipoti et al. [56] analyzed point defects using double-crystal X-ray diffraction (DCD) technique by comparing with the perfect crystalline silicon as a reference. From the phenomenon that the lattice parameter is smaller than that of the underlying perfect substrate, they deduced that these point defects are in vacancy-type. Other indirect methods such as preferential chemical etching, SCM, DLTS, minority-carrier transient spectroscopy (MCTS), can also be employed for indirect point defect characterization. In this chapter, some techniques will be more detailed because they have high efficiency on defect characterization and are used in this thesis.

Chemical etching technique – Preferential wet chemical etching process could be used to characterize not only dopants but also defects in silicon, including dislocations as well as point defects. This technique is destructive to the analyzed materials and devices. Due to its magnifying effect, the chemically etched volume provides the possibility of indirect defect detection using TEM, SEM and even optical microscope. However, this effect also gives rise to the artifacts of the dimension measurements of the defect distribution due to its locally enlarging etched defective volume in 3-D directions. Etchants for defect delineation are often composed of hydrofluoric acid (HF) and an oxidizing agent such as CrO_3 [79] [80] [81], $KBrO_3$ [82] and HNO_3 [83–84]. As Lehmann summarized, the enhancement of the etch rate may occur for several reasons [85], for examples: (a) Higher chemical energy of the elastic strain field present around dislocations; (b) High impurity concentration caused by gettering of impurities by dislocations; (c) Impurity that has formed a precipitate; (d) Different doping concentrations.

D. G. Schimmel [79] studied defect delineation by preferential etching using various chemical solutions. Table 3.1 shows the comparison of the etch rate of the main solutions used in defect characterization in silicon material and devices. Even if the Secco solution gives the best etched pit for the <100> defective Si samples due to its highly selective etching profiles, it is not often used because the solution is a poison. Moreover, in practical analysis, etch results, reflected by the obtained pits, can be influenced by various factors, such as impurities in the defective volume, conductivity type, temperature of solutions, agitation and illumination. Basically, formation of holes is required for an oxidation process prior to the step of the oxide removal by HF.

Table 3.1. Comparison of etch rates based on Sirtl, Secco, Dash solutions.

Etch	Formula	Etch rate
Sirtl	$HF:CrO_3$ (1:1)	Nonlinear, ~3.5 µm/min
Secco	$HF:KrCr_3O_3$ (2:1)	1.5 µm/min with ultrasound agitation
Alternate Secco	$HF:CrO_5$ (2:1)	~ 1 µm/min with ultrasound agitation
Dash	$HF:HNO_3:CH_3COOH$ (1:3:10)	~ 0.1 µm/min with light n-substrate

Scanning capacitance microscopy – Scanning capacitance microscopy (SCM), which is extensively used for material and device analysis, is based on an electrical measurement of the materials. The principle of the SCM measurements is to use a conductive AFM tip to detect the so-called voltage derivative of the contact capacitance ($\Delta C/\Delta V$). ΔC is defined as the difference between the capacitance C (V_+) at the highest voltage V_+ used and the capacitance C (V_-) at the lowest voltage V_- used. The magnitude of ΔC is related to the doping level or defect level. Brezna et al. [86] pointed out that SCM can detect quantities as small as 10 –100 impurity atoms, other than dopants, per cubic micron (10^{13} – 10^{14} cm^{-3}). They had successfully used SCM technique to characterize the damage on silicon materials, induced by FIB (focused ion beam) milling, and revealed

that the actual damage depth, caused by FIB milling, is much greater than that proposed by other authors by taking the advantage of the higher sensitivity of SCM technique.

Another example is that a combination of AFM and SCM was used to investigate the relationship between the surface morphology and the near-surface electrical properties of GaN films grown on c-axis sapphire substrates by metalorganic chemical vapor deposition [87]. Local regions surrounding threading dislocations displayed a reduced SCM signal with applied voltage, comparing with the regions that contained no dislocations. The positive voltage shift in the capacitance–voltage (C-V) characteristics obtained in the areas surrounding the dislocations indicates the presence of negative charge in the vicinity of threading dislocations. They deduced the presence of deep accepterlike trap states near the valence band associated with threading dislocations. Moreover, they also state that the segregation of charged impurities or point defects may also play a role in determining the electronic structure of the GaN near the dislocations.

However, this technique is limited by the requirement that it needs special sample structure and the analyzing defects should be within a surface of less than 1 μm. MOS structure with a very thin layer of dielectric materials on semiconductors is required in order to have high sensitive SCM signal. The substrate also should have a good electrical connection with the SCM system. The second important factor is that the defects should have a columnar structure, perpendicular to the surface, in order to enhance the capacitance difference between the perfect and the defective crystalline Si.

Deep-level transient spectroscopy – Deep-level transient spectroscopy (DLTS) was introduced by Lang in 1974 [88]. After that, this technique has played a very important role in the characterization of deep level defects in semiconductors. The basic principle of DLTS is to agitate the occupancy of traps by changing the value of the reverse bias applied to a Schottky diode or a pn-junction resulting in a space charge condition. DLTS is highly suitable for such characterization due to its remarkable sensitivity up to $\Delta C/C = 10^{-6}$ for silicon. Very high concentrations of electrically active defects with values from 10^{13} to 10^{15} cm^{-3} were detected by DLTS in samples irradiated with pulsed lasers

[89 - 90]. These defects were considered to be trapped during the rapid quenching process at the end of laser-induced melting. Hartiti et al. [91] analyzed the electrical activity of point defects in Si after melting by excimer laser irradiation. They pulses a laser beam with size of 2×10 mm^2 with duration of 21 ns and scanned on the p- and n-type samples, which were covered by a 200 nm thick oxide. Following laser irradiation and oxide removal, metal dots with 1 mm in diameter were evaporated onto the sample surfaces to form Schottky diodes for DLTS measurements. They also indicated that the main parts of these traps were caused by the quenching process. The excimer laser-related point defects seems to be identical to those reported for solid ruby and Nd:YAG lasers, therefore, they deduced that the electrically activation of defects for all lasers working in the melting condition is only related to the resolidification velocity. However, for DLTS, a large area, e.g. 1 mm dots above, of samples is needed, which is not suitable for our case presented in the thesis.

3.1.2. EVALUATION OF DISLOCATION AND OTHER DEFECTS

Except point defects, some other defects, including line defects, area defects, volume defects, could also exist in Si crystals. Dislocations [26 - 27] may be edge dislocations, screw dislocations, or mixed dislocations containing both screw and edge dislocations. These are important defects existing in silicon crystals, and a full treatment of their properties, formation, growth, and movement is a complex subject. Area defects in single crystalline silicon include stacking faults, grain boundaries, and twin boundaries [92]. Stacking faults are the most important area defects that degrade the performance of integrated circuit components. Volume defects in crystals include voids and local amorphous regions, and precipitates, but the most important volume defects are precipitates of extrinsic or intrinsic point defects. The precipitate formation and growth is also a very complex subject. Precipitates first nucleate an intermediate crystal structure that is later transformed into the final structure. The initially formed particles are called nuclei. Once precipitates are formed the lattice, surrounding such precipitates,

is subject to large compressive stresses. This compression could be relieved in some ways, such as generation of other crystal defects, e.g. formation of Si self-interstitials, absorption of vacancies, and punching out of dislocation loops [25].

The detection of those defects, except point defect, in silicon has been performed with a variety of measurement techniques. Some common techniques, with high spatial resolution, for microelectronic materials and devices are summarized in Table. 3.2.

Table 3.2. Techniques for structural characterization and dopant evaluation for microelectronic devices.

Analysis Field			Analytical Techniques		Dynamic range (atoms/cm^3)	Spatial Resolution	Features	
							Advantages	Limitations
Structure	Surfa-ce		TEM		--	0.24 nm	High Resolution	
			SEM		--	< 5 nm	Easy sample preparation	
			AFM		--	1.5 - 5 nm		
Dopant Characterization	Relative Analysis Methods	2D	Methods combined with DSE technique	TEM	> 8×10^{16}	0.24 nm	High Resolution	Poor reproducibility
				SEM		< 5 nm	Easy sample preparation	Limited sensitivity
				AFM		1.5 - 5 nm		
			SCM		10^{15}-10^{20}	10-25 nm	Distinguish n-type/p-type	No mature system; uncertain at junctions
			SSRM			30 nm	Easy sample preparation	Cannot distinguish n-type and p-type
			SEM + EDX		> 5×10^{20}	1 µm		Is not sensitive to B
			FE-SEM		> 4×10^{16} (for p-type)	< 6 nm		Very low contrast for n-type
	Quantification	1D	SRP		10^{15}-10^{20}	Very low	Easy sample preparation	Cannot distinguish n-type and p-type
			SIMS		> 10^{14}	40 nm (Imaging) < 5 nm (Depth profiling)		

Electron microscopy – The morphology of microelectronic devices is generally determined by two electron microscopic techniques: a) scanning electron microscopy (SEM); and b) transmission electron microscopy (TEM) due to the capability of providing very high magnification (maximum magnification of 100,000 X for SEM and 1,000, 000 X for TEM), resolution (1 nm for SEM and 2.4 Å for TEM), and depth of field (e.g. 1 – 4 µm at 10,000 X for SEM) [93 – 95]. One example [96] is that TEM is used to characterize single electron memories with microstructures of metal-oxide-semiconductor capacitors with Si nanodots formed by silicon rich oxide. The size of the

dots and microtwins in the materials were observed and analyzed using bright field, dark field, high resolution TEM (HRTEM) and diffraction observations. The electrical properties of charge trapping and charge transportation through the dots are as results of the microstructures presented in the devices. Pan et al. [97] used plan-view and cross-sectional TEM to study {113} rodlike defects and {111} dislocation loops in implanted and annealed silicon materials.

Chemical etching techniques – Etching technique with the same chemical solution given in Table 3.1, followed by TEM, SEM and AFM analysis, is also used for dislocation and other defect analysis such as grain boundaries of polycrystalline silicon. There are mainly two factors allowing those defects to be revealed i) the higher chemical energy of the elastic strain field presents around a dislocation; ii) a high impurity concentration caused by gettering of impurities due to the presence of dislocations. Normally, dislocations, stacking faults, swirls, and saucer pit defects are detectable with chemical etching and inspection by electron/optical microscopy, etc. [72]. For example, Bourret et al. [98] used a mixture of HF:HNO3 with ratio of 10:90 to slightly etch dislocations and precipitates, therefore it made them easier to be found under bright field TEM and high resolution TEM observations. Another example is that Furukawa et al. [99] observed etching pits using optical microscopy and TEM technique after the samples had been etched using non-agitated Secco solution for 30 min, revealing point defects formed by self-interstitials. Bisero [100] had performed a preferentially chemical etch on the polycrystalline silicon, revealing the grain boundary and measuring grain size of the materials using SEM. On this delineation, an etchant comprising of hydrofluoric acid : nitric acid : acetic acid was used. The etching rates near and in grain boundaries are different from that in the grain body, resulting in a SEM contrast between the grain boundaries and the grain. However, overetching should be avoided when using this technique, and etching time as short as 3 s is used to optimize the results.

3.2. DOPANT AND IMPURITY EVALUATION

As it is well-known, the dopant evaluation techniques have not followed the shrinkage step of semiconductor devices to submicron levels since the mid 1980's. A number of techniques available for one-dimensional (1-D) dopant evaluation have not been effectively extended to two-dimensional (2-D) dopant characterization [101], especially with high spatial resolution. The design of modern device fabrication flows requires examination of comprehensive device properties including dopant distribution in both the lateral and vertical directions. Even process and device simulators are widely used in fabrication process development but the development of accurate 2-D process models is severely hampered by the lack of providing 2-D dopant profile information [102]. The National Technology Roadmap for Semiconductors pointed out that the large requirements for the 2-D and 3-D mapping of new-device-generations include a spatial accuracy below 5 nm and sensitivity to the doping concentration from 10^{16} to 10^{20} cm^{-3} as well as reproducibility of such results [103].

To address the requirements of highly accurate and high spatial resolution evaluation of dopant distribution, a number of dopant-profiling techniques are currently being developed in research labs [104]. However, in actual device characterization it is necessary to distinguish the difference between chemical or atomic and electrically active dopant profiles. Chemical profile is usually measured using secondary ion mass spectrometry (SIMS) [105]. Accurate determination of the electrically active dopant profile in microdevices such as LDRs is more important because it determines critical behaviour of those devices such as resistance values and three-dimensional (3-D) current paths. Therefore, there is a difference between the electrical resistance value, obtained by laser processing, and the data of dopant distribution, which can be modeled by analytical/numerical simulation and only reflect the chemical atomic dopant distribution. Table 3.2. lists some common techniques for 2-D and 1-D dopant profiling. Some techniques involving methods based on electrical measurements such as scanning capacitance microscopy (SCM), spreading resistance profiling (SRP), capacitance-

voltage (CV) measurements, potential and tunnelling currents, methods based on chemical selective etching in combination with TEM, SEM, AFM, and optical microscopes, and methods of field emission SEM (FE-SEM) and secondary ion mass spectroscopy (SIMS), will be outlined in the following sections. Some other techniques such as electron energy loss spectroscopy (EELS) and energy dispersive X-ray (EDX) analysis can also be used for impurity evaluation such as oxygen and metals; however, their sensitivity is still very low (about 1 at. %). On the other hand, TCAD also promises prediction of both structural and electrical parameters of advanced semiconductor devices. Therefore, circuit designers can design layouts and test new circuits without fabrication, in evaluating the probability that the circuits will work when they are manufactured [106].

3.2.1 METHODS BASED ON CHEMICAL TECHNIQUES

The characterization technique of doped silicon layers based on chemical behaviour, including chemical stain of doped silicon materials and dopant selective etching (DSE), had been discovered since the early days of the semiconductor device industry [85] [109 – 111]. Based on an electrochemical displacement reaction from a metal-ion-based solution, staining technique uses selective deposition of a metal such as Cu, Au, Ag or Pt on one side of the junction, generally the n-type side. Chemical selective etching techniques commonly use mixtures of HF with oxidizing agent such as HNO_3 and a dilute solution such as CH_3COOH or H_2O, to preferentially etch the highly doped area by comparing the etch rate on the area of low doped n-type or p-type Si. Moreover, HF (48%) solution could also induce Si etching action, which is most probably caused by the oxidation of silicon by the hydroxyl ions (OH⁻) in the aqueous solution [112]. However, this etching rate is relatively low even for heavily doped silicon materials. The etching reaction paths are summarized in Fig. 3.1.

For the delineation of p-type layers, alkaline solutions can also be used because the etch rate is significantly reduced for dopant densities in excess of 10^{19} cm^{-3} [85]. However, independent on the techniques used, the accuracy of chemical staining and etching techniques is often susceptible to error due to the reproducibility of factors such as quality of prepared sample surface, the concentration of the staining or etching solution, etching time, the volume of solution in contact with sample surface and the agitation of the solution on the sample, solution temperature, and illumination on the sample surface [113]. In this dopant evaluation technique, the dopant contours revealed by selective etching is normally calibrated by two methods. The first one uses a 1-D profile, directly obtained by other technique such as SIMS [114-120], SRP [116 – 117, 121-124] or numerical simulation [123, 121, 125-126], adjacent to the 2-D area of interest. In the SIMS and SRP measurement, a large window size is needed in order to have the depth dopant profile. For example, in the conventional profiling of lightly doped drain (LDD) of MOSFET, the lateral dopant profile is calibrated against the
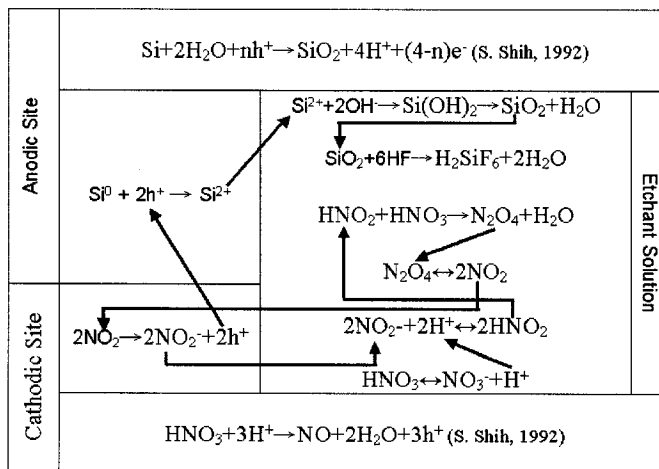
Fig. 3.1. Summary of chemical etching reaction for DSE [111].

known SIMS or SRP depth dopant profile by following the etching contours. The second method of calibration involves direct measurements of etching rate as a function of dopant concentration using homogeneously doped bulk silicon [126-127] or epitaxial silicon.[116, 123 – 124] The surface of the samples is normally covered with silicon

nitride, which serves as a reference for measuring the etched thickness. Chemical etching is indispensable because it is time efficient and gives a two-dimensional image. One important consideration, which should be mentioned, is that various defects such as point defects and dislocations also affect the etching behaviour. The characterization instruments which have been conventionally used for investigating selectively stained or etched samples are transmission electron microscope (TEM), atomic force microscope (AFM), scanning electron microscope (SEM) and optical microscopes.

Transmission electron microscopy – TEM image contrast obtained from doping-dependent etching was used to characterize p-n junctions in silicon [128]. The local variations of crystal thickness give rise to the appearance of thickness fringes which was interpreted as two-dimensional (2-D) iso-concentration profiles that illustrated the dopant distribution. Various mixtures of HF, HNO_3 and CH_3COOH with volume ratios of 1:1:6; 1:3:8, 1:6:16, 1:10:10, and 3:6:16 have been used with etching duration from 3 to 40 s. Yoo et al. [129] used TEM in combination with preferentially chemical etching for obtaining 1-D and 2-D dopant concentration profiles of metal-oxide-semiconductor field-effect transistor (MOSFET) with structures of n^+/p fabricated using 0.25 μm device technology. The thin cross-section TEM samples were dopant-selectively etched with 0.5% HF : 99.5% HNO_3 with an etching duration of 10 s. Local etch rates were determined from TEM thickness fringes and then converted to dopant concentrations using an independent SRP and SIMS data. The vertical ultra-shallow junction depth of ~51 nm and an effective gate length of ~161 nm were obtained based on those evaluations. Moreover, Spinella et al [116] have investigated two-dimensional boron distributions in n- and p-type Si substrate. They pointed out that an appropriate TEM sample preparation method was a fundamental issue to obtain good reproducibility and sensitivity of the dopant evaluation by this chemically selective etching technique. During investigation of boron-doped p-type silicon using HNA chemical selective etching, Spinella et al. [130] showed that the presence of point defects results in a decrease in etching rate. For the n-type regions, however, they did not clearly point out

the effects of defects on the etching behavior. Choi at al [131] also concluded that the defects observed in the heavily implanted sample can act as recombination centers for free carriers, leading to the reduction in the carrier concentration and hence etching rate, which is consistent with the TEM results.

Atomic force microscopy – The application of AFM on dopant evaluation using chemically selective etching needs calibration of silicon etch rates by etching different samples with different doping levels with a reference to non-etched coating materials [132 – 133]. In order to quantify the 2-D dopant distribution, two polished cross-section samples could be simultaneously performed by the chemical etching process [134]. One of them, having a dopant profile obtained by other techniques such as SIMS, serves as the calibration reference for the unknown doping profile. The potential issues in this method are: (i) in practice, the cross-section sample is not absolutely placed vertically and the topography measured by AFM might not correctly reflect the dopant profile and (ii) the AFM tip artifacts impedes the accuracy of the topographical information, especially on samples with a high dopant gradient. Alvis et al. [135] also reported that the limitation of this method involved the comparison of results from sample to sample. Variations in absolute etch rates made it difficult to achieve a good repeatability. Their approach to repeatability is to minimize surface variations of cross-section AFM samples by stacking the different samples together using epoxy, thus minimizing junction characterization variations [135]. This method allowed them to address practical aspects of the extension of cross-sectional AFM to junction determination. They measured that a 120 keV ion-implantation resulted in 60 – 80 nm deeper doping profiles than a 35 keV ion implantation. A junction shift of the source and drain regarding to the gate was also detected according to the change of the ion-implantation angle. They stated that the detection limit of pn junction by chemical etching was in the range of 10^{17}–10^{18} cm^{-3}. Epitaxially grown p- and n-type test structures with abrupt dopant concentration variations in the range of 10^{15}–10^{20} cm^{-3} were studied by Ukraintsev et al. using dopant selective etching and AFM [136]. The chemical solution

used is HF (49%):HNO$_3$(70%):CH$_3$COOH (100)=1:40:20 and etching time was varied from 3 s to 10 s.

Scanning electron microscopy – Etched cleaved or polished cross-sectional surfaces were observed by SEM in the previous studies. Wang et al. presented that SEM image was obtained from additionally Cr-coated cross-sectional surface of n-type MOSFETs with gate lengths from 100 to 200 nm after HNA etching [133]. The boundary between the etched region and the silicide layer with thickness fluctuations were better distinguished in the SEM images than those in AFM images. However, determined junction location from SEM images is about 23 nm less than the metallurgical junction determined from SIMS profiling. Alvis et al. reported using SEM imaging in conjunction with dopant selective etching technique to reveal the parameters describing junction depth and gate overlap of N-MOSFET devices [135]. Tseng et al. [137] reported that the effective channel lengths (L$_{eff}$) of transistors, revealed by SEM imaging from both etched and stained samples, are comparable with the data obtained from electrical measurements. Gong et al. [122] optimized dopant delineation method of chemical etching by using UV illumination and measured 2-D profiles based on short term etching. They were able to obtain the dopant evaluation down to concentration of 6.0×10^{16} cm^{-3} converted by 1-D data from SIMS measurement.

3.2.2. METHODS BASED ON ELECTRICAL TECHNIQUES

The electrical techniques which have been employed for dopant/carrier profiling involve 1-D profiling methods such as capacitance-voltage measurement and spreading resistance profiling (SRP) and 2-D methods such as scanning capacitance microscopy (SCM), scanning spreading resistance microscopy (SSRM), nanopotentiometry/ scanning voltage microscopy (SVM), scanning kelvin probe microscopy (SKPM), scanning surface harmonic microscopy (SSHM) and scanning tunneling microscopy (STM). Nanopotentiometry (or SVM), in principle, is a scanning probe microscopy

(SPM) technique providing the possibility of perception on the actual functioning behavior of semiconductor devices [138]. An electrically conductive SPM probe is used for potential detection by scanning on a cross-sectional sample surface in order to evaluate the distribution of the electrical potential of an operating device. Therefore, the information obtained in conjunction with simulation gives the knowledge of carrier distribution. In the study of Trenkler et al. [138], they had measured deep submicron complementary metal-oxide-semiconductor (CMOS) devices. The isopotential lines inside the drain region, indicating the potential gradients, give the idea of the carrier/dopant distribution of operating CMOS. Ban et al. [139] used SVM to map the voltage distribution across the InP p-n junction structure under forward and reverses biases. They suggested the detectable resolution of the variation of depletion width with the application of external bias, provided by the system, was one nanometer. However, large contact forces are needed in this measurement for the probe to mechanically penetrate through the native oxide on the Si surface in order to provide a reliable electrical contact. This not only induces damages of the cross-sectioned surface on the active devices but also causes additional surface leakage, which disturbs the measured data [140].

The scanning tunneling microscope (STM), with a metallic probe having a radius of curvature of the order of 50 nm [141 – 142], is a well-established surface probe that is routinely capable of spatial resolution of the order of 10 Å. The probe is located above the sample surface in air or in ultra-high vacuum at a distance of a few angstroms. A precise scanning system is used to scan the probe over a small area of the sample surface and the tunneling current or capacitance between the tip and sample surface topography are monitored simultaneously. A feedback loop controls the distance of the probe from the sample such that the measured current or capacitance is constant. Hessel et al. reported results of measurements of doping level and surface topography on doped Si structures with periodic and lateral modulations of dopant concentration [143]. The measurements were carried out in a UHV-STM system, equipped with a fast load lock for sample introduction. The pressure of the system was reduced to below 5×10^{-10} mbar.

Before annealing, the oxide on the sample surface was removed. The sample was degassed (< 400 ^{0}C) in a preparation chamber under the UHV conditions, and, then, transferred into a separate chamber containing the STM. During the period of measurements (usually 2 to 3 hours and even up to several hours), no fluctuation in the imaging quality was detected. Experimental comparison of two differently annealed samples showed that the displacement of n$^+$/n junction was much larger for a RTA-annealed sample (1100 ^{0}C, 30 s) than that for a furnace annealed sample (900 ^{0}C, 60 min). Hosaka et al. [144] performed STM on the surface of Si wafer with a structure of p-n junctions fabricated by ion-implantation and consequent thermal annealing. The samples were immediately chemically etched to remove oxide before they were loaded into the vacuum chamber of STM. Tunneling current characteristics between the probe and the substrate, as a function of bias, were monitored and an obvious difference in the current signal between the p- and n-type sides was detected under specific bias conditions. However, as Wolf et al. pointed out, the scanning tunneling microscope requires a conductive surface such that STM measurements on silicon cannot normally be performed in air due to the presence of the native oxide [113]. However, Kordic et al. [145] demonstrated that STM imaging of freshly cleaved Si pn junctions in air is possible. They pointed out that the junction localization down to 50 nm was limited by the long time effect of surface oxidation due to the required measurement, caused by the fact that the cleaved surface was exposed to air before the pn junction could experimentally be localized. Few years later, Kim et al. [146] presented a novel in situ sample cleavage technique, which can be used for preparing cross-sectional STM samples. This technique can be easily applied to any ultra-high vacuum STM and it has coarse motion and tip exchange capabilities. However, only {110} plans could be obtained because the breakage is usually along <110> directions for silicon. Thus, the structure of interest must be oriented exactly in those directions, which limits the flexibility of the STM technique. Moreover, it is not possible to determine the dopant profile with respect to the dielectrics edge as the STM cannot map the oxide location due to the insulating properties of the surface.

The scanning surface harmonic microscope (SSHM) is in fact a STM, in which a microwave (RF) signal is applied across the tip-sample tunneling gap and higher harmonics are detected by a microwave cavity. SSHM is sensitive to the capacitance and voltage characteristics of semiconductoring samples with nanometer resolution. Bourgoin et al. [147] verified this versatile technique may fulfill a high resolution of 5 nm and the sensitivity requirements to doped Silicon with a wide range of dopant concentrations. SKPM is another SPM based technique which is developed on a non-contact AFM. The principle of SKPM is that by measuring the electrochemical potential difference which minimizes the electrostatic force between the probe and the sample surface, one can estimate the work-function difference, which is a consequence of the dopant/carrier level at or near sample surface between the tip and sample surface [148]. In their study, Henning et al. demonstrated that this technique is sensitive to variations in dopant concentration from about 10^{15} to 10^{20} cm^{-3}. Finally, they applied this established technique on dopant evaluation of the LDD (lightly doped drain) region of silicon MOSFET. Moreover, some scanning probing methods for obtaining quantitative 2-D dopant profiles from p-n junction samples have been recently reviewed by Wolf et al [113]. They concluded that although the SCM and SSRM techniques are still in a development or optimization stage, those two techniques can be the leading candidates to become generally applicable as 2-D carrier/dopant mapping tools for the next generation of microelectronic devices because they can both satisfy the required resolution and dynamic range.

Capacitance-voltage technique and SCM – As described by Sze [149], the contact and non-contact capacitance-voltage (C-V) techniques have been well developed for one-dimensional carrier profiling. A simple but significant illustration about doping dependence of the C-V characteristics of an 1-D MOS (metal-oxide-semiconductor) structure was also shown by Taur et al. [150]. Poyai et al. improved the accuracy of extraction of carrier concentration and depletion width by considering the series resistance and the capacitance of the heavily doped regions [151]. Then, they applied

this method to evaluate the carrier concentration of n^+ region in p-well with very high accuracy.

Scanning capacitance microscopy (SCM) is an extension of conventional AFM, as schematically shown in Fig. 3.2 (a) [216]. It is a promising tool for modern semiconductor device characterization since its first use by Matey and Blanc in 1984 [152]. In brief, the principle of the SCM technique is based on the high-frequency response of the MOS micro-capacitor between a thin probe and a semiconductor. According to fundamental on C-V measurements on MOS structure

$$C = \frac{C_0}{\sqrt{1 + \frac{2K_o^2 \mathcal{E}_0}{e N_d K_s t_o^2}(V_{DC} + V_{AC})}}$$

where C_O is the thin oxide layer capacitance per unit area; K_O and K_S are the dielectric constants of the oxide and of the semiconductor, respectively; ε_0 is the permittivity; e is the elementary charge; t_O is the oxide thickness, N_d is the carrier concentration, and $V_{DC} + V_{AC}$ is the applied voltage. Therefore, in principle, the capacitance variation should depend only on the carrier concentration in the semiconductor surface. It should be mentioned that when the dopant concentration varies moderately over a scale comparable to the Debye length (Deby length is 10 nm and 0.4 nm at concentration of 10^{17} cm^{-3} and 10^{20} cm^{-3}, respectively.) the carrier concentration is in good agreement with the electrically activated dopant concentration [154]. If all the dopants are fully electrically activated, the obtained data is referred to dopant concentration.

Similar to the SCM measurement on defects, the magnitude of ΔC is defined as the difference between the capacitance C (V_+) at the highest bias voltage V_+ and the capacitance C (V_-) at the lowest bias voltage V_- used during the SCM operation. The carrier concentration is detected from the change in capacitance (ΔC). The sign of ΔC indicates the doping type and ΔC tends to increase with lower net doping level [153]. For example, Fig. 3.2 (b) shows the results [216], indicating the dopant profile (solid line) and simulated difference capacitance (ΔC) plot (solid squares) of a 1 D p^+-n junction with p-type concentration of 2.5×10^{17}cm^{-3} and n-type concentration of 1×10^{15}

cm^{-3}, which is obtained using a 2-D device simulator (MEDICI). The axis x represents the direction from the left side to the right side. During the increasing cycle of (V$_{dc}$+V$_{ac}$), ΔC is negative for p-type doped semiconductor materials and lower of absolute value, while it is positive for n-type Si and high of absolute value. On the other hand, in the depletion region of the p-n junction, the simulation result reveals the low-frequency C-V curve responding of the supply of minority carriers from the opposite sides of the junction.

There are two modes on SCM measurements and both could be taken in air. The first one is a constant voltage mode, consisting of applying a sine wave voltage with constant amplitude (dV) to the sample and, measuring the change of capacitance (dC). The lateral resolution is limited to twice the probe tip radius [148]. The main disadvantage of this mode is that the lateral depletion region under the probe is larger in lower doping level region and smaller in the higher doping level region [153]. This makes it difficult to interpolate the carrier concentration. The second mode of operation which consist of fixing the capacitance (dC) and measuring the change in potential (dV) was introduced by Y. Huang and C. C. Williams [155]. This new approach to SCM, in which the ac bias voltage is applied to the sample, can be adjusted to maintain a constant capacitance and, thus, nearly constant depletion width can be obtained. This might indicate that the expected spatial resolution is equal to the probe diameter. It was shown that the SCM results were in good agreement with lateral simulation profiles in the dopant concentration range of 10^{16} to 10^{20} cm^{-3} [148]. However, the control of the constant dC signal is complicated and is not well implemented in the software and hardware package available. Therefore, most results, presented in the literatures and applied in industrial flows, are obtained under constant-dV operation condition.

Even though many promising experimental SCM data on test structures and MOSFETs have been published, there are still some challenges to obtain reproducible an reliable SCM data [156 – 157]. The following parameters have to be carefully addressed: (i) quality of the insulating layer between the tip and semiconductor such as existing

traps in the oxide layer, (ii) the tip quality itself, (iii) mobile surface charges, (iv) sample itself, (v) parameters of the capacitance sensor, and (vi) dopant extraction model.

Spreading resistance profiling and SSRM – Since its introduction in the 1960s by Mazur and Dickey [158], the spreading resistance technique has been in use for the measurement of resistivity and carrier concentration variations in Si materials. Nowadays, spreading resistance profiling (SRP) has been developed and provides carrier/dopant concentration information on ultrashallow junctions [159] with high accuracy and resolution in one dimension. This technique is a two-point-probe technique which measures the local electrical resistance on initial or beveled semiconductor surface. The advantage, comparing with four-point-probe technique (4PP), is that SRP has much higher spatial resolution. The probe tips, usually made of a tungsten-osmium alloy, are separated by a distance of typically 40 to 100 μm and their contact areas with the semiconductor surface are usually 4 to 5 μm in diameter. The current between the two probes spreads over a small space region near the semiconductor surface, which is the reason of the so-called "spreading resistance". This technique is used for carrier concentrations in the range from 10^{12} to 10^{19} cm^{-3} [117]. However, with the application towards shallow junctions of less than 35 nm, the concurrent electrical resolution is affected by several artifacts such as carrier spilling, probe separation, large bevel stepsize, surface damage, probe penetration, 3-D current spreading, large correction factors, etc. Recently, to overcome the drawbacks Vandervorst introduced the Nanoprofiler^{TM} (NP) based on a two probe version of SRRM technology with small tips of 10 to 20 nm in diameter and low force [160]. This system can reduce correction factors back to <10 and has minimal probe penetration and extremely small stepsize with simultaneous topography imaging. In principle, profiling with high resolution such as 0.1 to 0.2 nm is feasible. Furthermore, Eyben et al. [161] showed doping structures of complementary metal-oxide-semiconductor (CMOS) and bipolar transistors by SSRM imaging using diamond probe with sub-nm spatial resolution.
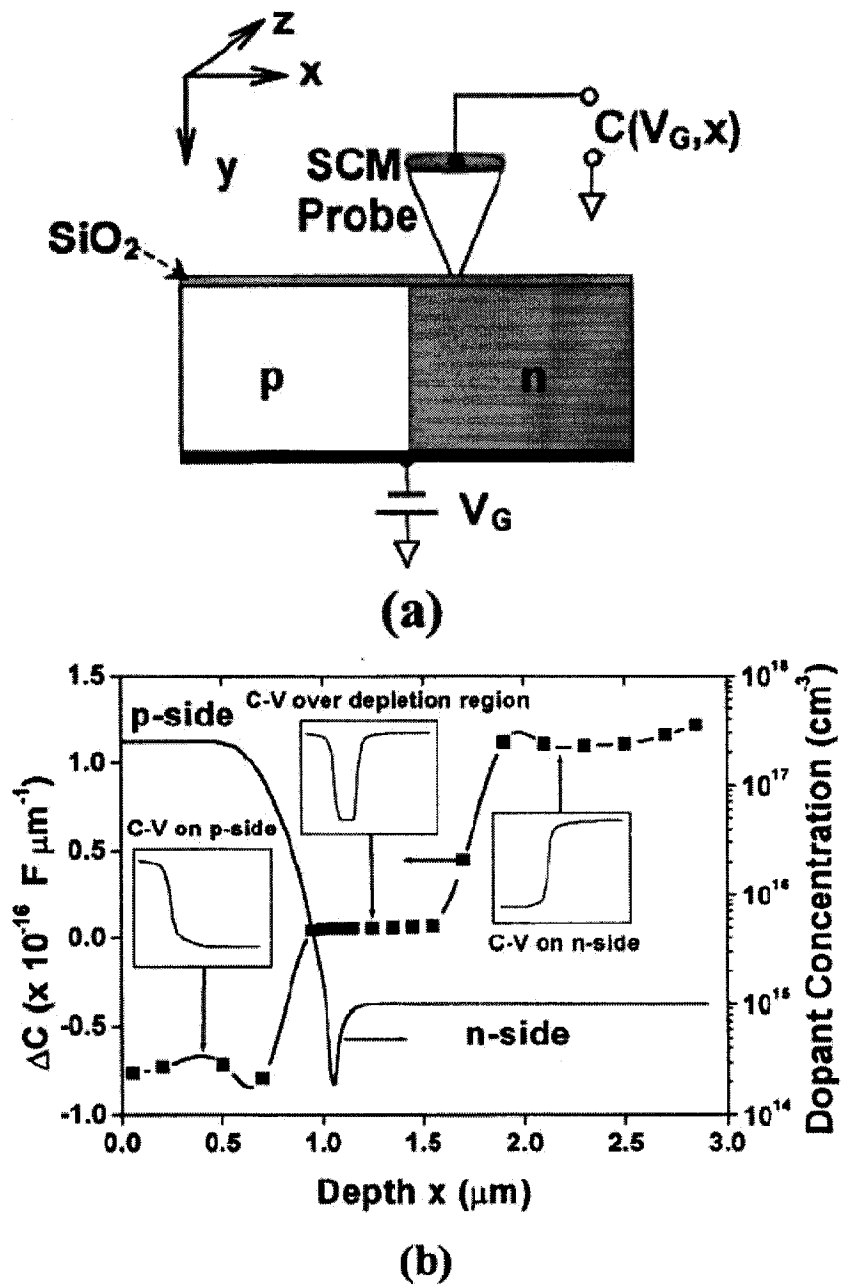
Fig.3.2. (a) Schematic setup for SCM measurement. A bias of $-V_{DC}$ (corresponding to the tip bias voltage of V_{DC}) is applied to the sample. (b) Dopant profile (solid line) and simulated capacitance difference (ΔC) plot (solid squres) of a 1-D p-n junction.

3.2.3. SECONDARY ION MASS SPECTROSCOPY

Secondary Ion Mass Spectroscopy (SIMS) is the mass analysis of secondary ions ejected from the surface by ion sputtering. By bombarding the surface of a solid, the energetic ion beam generates a variety of secondary transitions, including electrons, photons and ions. Detection of any of these secondary events could serve as the basis for any analytical probe. However, SIMS equipment is optimized for the detection of positive and secondary ions.

In SIMS technology family, dynamic SIMS technique is used for profiling one-dimensional (1-D) chemical dopant distribution. Bryan et al. [162] for the first time reported 3-D chemical profiling of a npn bipolar transistor, carried out by digital imaging SIMS system. In their measurements, a rastered beam was used for obtaining complete 2-D images of vertical slices through the sample surface. The depth resolution and the widths of the transient regions at the surface and at buried matrix interfaces limit the information content of a SIMS depth profile. The primary beam energy was normally from 2 to 15 keV up to 1980s. In order to improve the SIMS sensitivity, Dowsett et al used a specially fabricated sample which allows material to be collected from a large number of similar volumes [163]. Dowsett et al. suggested that reducing the primary beam energy would significantly improve the SIMS properties [165]. Stevie [166] presented that abrupt dopant profiles were obtained with low energy primary beams. Furthermore, a quantitative 2-D boron dopant profiling for submicron technology has been demonstrated using SIMS by Ukraintsev et al [167]. They realized even 2-D imaging with a lateral resolution of 10 nm and a sensitivity of 3×10^{17} cm^{-3} can be obtained on commercial SIMS equipment. Various SIMS profiles would contain information about the 2-D dopant distribution and a tomography algorithm could be used to extract the dopant profile. However, the SIMS measurement is destructive, time consuming, and requires multiple samples to achieve a single profile.

3.2.4. SCANNING ELECTRON MICROSCOPY

In the early period, researchers [164] [168] studied 2-D pn junctions by SEM imaging in electron beam induced current (EBIC) mode. For example, Roberts et al. [164] had localized the n^+p junction of a NMOSFET from cross-sectional samples. Even the depletion region, which appeared as a uniform bright area, limited the spatial resolution of this technique. However, due to the small width of the depletion region on the heavily doped side of the junction, an estimated junction depth might be obtained by measuring the distance from the surface to the bright area. Recently, it was shown that doped areas in silicon materials could give rise to contrast in secondary electron imaging. Perovic et al. [169] suggested that the contrast might arise from changes in the surface barrier, through which secondary electrons would get away from the solid. The surface energy barrier variations are a result of Fermi level pinning at the interface between vacuum and semiconductor. Castell et al. [171] pointed out that p-type dopants, which provide holes, decrease the potential and n-type dopants, which provide electrons, increase the potential. Electrically inactive dopants have no effect at all on the ionization potential. This potential difference can be revealed through secondary electron imaging in SEM measurements [170] [172 – 173] and allow dopant type and electrical activity to be two-dimensionally mapped rapidly. Elliott et al. [174] demonstrated that contrast can be detected from heavily p-doped areas of metal-oxide field-effect transistors (MOSFET) using secondary electrons with spatial resolution of one nanometer. Based on their study, the concluded that applying a reverse bias across a p-n junction enhances the contrast between the p- and n-type Si, while a forward bias decrease the contrast. Turan et al. [175] suggested that the image contrast and the resolution from active dopants can be enhanced by using field emission SEM (FE-SEM) due to the introduction of field-emission electron guns with high electron intensity coupled with the design of relative detector systems. Venables et al. [176] reviewed the issues related to sensitivity, spatial resolution, calibration methodology, p/n junction effects, sample preparation, and complexity. They concluded that the highest sensitivity for boron detection is about

4×10^{16} cm^{-3} and the spatial resolution is roughly 13 – 19 nm. In order to avoid the drawback of which the contrast from differently doped n-type regions is extremely low and, thus, to avoid instability of detection of p-n junctions, Schonjahn et al. [177] introduced energy-filtered FE-SEM to enhance the contrast of n-type regions with different dopant levels. However, up to now by using this technique, most research groups have only studied test structures but not real microdevices and they have mostly concentrated on p-type Si materials because the sample preparation often limits the mapping of dopant levels.

It should be mentioned that no enhanced contrast from B-doped regions, in the heavily doped area and resistive links in LDRs, was observed in our FIB-prepared TEM samples. The reason maybe is the fact of which the surface layer, with thickness of 10 to 20 nm, of the FIB-prepared samples was amorphized by Ga beam.

3.3. TECHNIQUES USED IN THIS STUDY

In this study, characterization of microstructure, of LDRs related to 0-D, 1-D, 2-D, and 3-D defects, and impurities, including dopants and oxygen, are carried out by transmission electron microscopy (TEM), scanning electron microscopy (SEM), atomic force microscopy (AFM), scanning capacitance microscopy (SCM) analyses in combination with etching process with different chemical solutions. These methods are selected because of their high spatial resolutions and/or high sensitivities. Some specific samples, e.g. for TEM analysis, were prepared by focused ion beam (FIB) technique due to its high precision of localization on the devices. Other techniques on defects, such as deep-level transient spectroscopy (DLTS), are not used here because of low signal/noise ratio due to very small dimension of LDRs. Some methods for impurity/dopant analysis, EELS, EDX and SIMS, are also not employed for characterization of LDRs in this thesis because of their limitations in sensitivities or spatial resolutions. However, SIMS is used to evaluate the dopant profile on standard samples for dopant calibration of LDRs

because it can be assumed that all the dopants were electrically activated after annealing at 900 ^{0}C for 30 s.

CHAPTER 4 2-D DOPANT DETERMINATION IN LASER DIFFUSED SI RESISTORS USING DOPANT-SELECTIVE ETCHING (ARTICLE 1)

Y. Liao,[a] J.-Y. Degorce, J. Belisle, and M. Meunier[b]

Laser Processing Laboratory, Ecole Polytechnique de Montreal, Case Postale 6079,

Succursale. Centre-ville, Montréal (Québec), Canada, H3C 3A7

4.1 ABSTRACT

Two-dimensional (2D) dopant profiles, in the range of 9×10^{16} to 3.6×10^{18} atoms/cm^3, in laser diffused silicon resistors were obtained using dopant selective etching (DSE) in combination with cross-sectional transmission electron microscopy (TEM) method and focused ion beam (FIB) technique. Compared with conventional DSE/TEM dopant evaluation, the properties of this technique, related to the reliability, reproducibility and accuracy of quantification of dopant concentration from 9×10^{16} to 6×10^{19} atoms/cm^3, have been improved by considering a vector instead of a scalar etching rate as determined by an etching model, and by a novel calibration method. Those evaluated profiles were accurately compared with a numerical simulation based on heat transfer and diffusion equations.

[a])Corresponding author: Electronic mail: liao.yougui@polymtl.ca

[b])Corresponding author: Electronic mail: michel.meunier@polymtl.ca

4.2 INTRODUCTION

The National Technology Roadmap for Semiconductors[103] pointed out that requirements for the two-dimensional (2D) dopant mapping of new-device-generations includes a spatial accuracy below 5 nm, and a sensitivity to doping concentrations from 10^{16} to 10^{20} cm^{-3}, as well as reproducibility of the results. In addition, for laser diffused resistors (LDR), which are fabricated with small laser spots (1 ~ 4 μm in diameter), the depth distribution of dopants, strongly determining the values of the resulted resistances, is not constant, depending on temporal and spatial temperature distribution, melting time and dopant distribution of source and drain [4]. Many techniques available for one-dimensional (1-D) dopant evaluation have not been extendable to 2-D dopant characterization due to their limitations [101]. For example, SIMS (secondary ion mass spectroscopy) and SRP (spreading resistance profiling) are limited by spatial resolution and some 2D techniques, such as SCM (scanning capacitance microscopy), could not be used for some practical microdevices, such as LDRs produced by laser fine tuning (LFT) technology [4] with small laser spot sizes, limited by the difficulties of sample preparation.

The technique of dopant-selective etching (DSE) has been used to evaluate two-dimensional (2-D) dopant profile for several decades, even with shrinking device size. The chemical solutions were prepared by mixing oxidizing agent and HF aqueous solutions typically consisting of a mixture of HF, HNO_3, and CH_3COOH to preferentially etch exposed regions with high carrier concentrations in Si-based devices and materials. The underlying responsible mechanism is complex [178] and not completely understood, with an especially poor understanding of the etching process and the correlation between carrier concentration and the observed topography. Therefore, the accuracy and reproducibility are still very low and very often different from laboratory to laboratory. A large number of etching experiments were repeated by many authors in an attempt to find suitable etch recipes and special attention paid to the preparation of the initial samples, using conventional mechanical polishing and ion milling. Samples with initial thickness of up to 1.5 µm [179] were commonly etched for 1 – 40 s [116] [179] [124] at selected temperatures prior to topographical measurements.

The sample topography, after the etching step, can be imaged using transmission electron microscopy (TEM), secondary electron microscopy (SEM), or atomic force microscopy (AFM). In particular, the high spatial resolution of TEM allows one to measure small changes in the thickness of material removed by the etching process to reveal many details, which are not detectable by other techniques. However, there are some uncertainties in conventional DSE methodologies: (i) the etching rate was considered as a constant scalar as a monotonic function of dopant concentration. In fact, the etching rate should be considered as a vector with the change of direction of etching

rate according to the microstructure of the exposed etched surface during the etching process; (ii) in calibration, the silicon nitride or silicon dioxide often serves as a reference for measuring the etched Si thickness [124] [116] [123]. In fact, those dielectric materials are also etched by the chemical solution even if the etching rate is lower than those of doped silicon; (iii) in calibration, the etching properties were postulated such that the silicon etching rate for both standard and testing sample depends on dopant concentration only under similar etching conditions, including sample surface preparation, temperature, concentrations of the etching solution, time, light illumination, agitation, etching time, sample thickness, etc. Actually, the etching behaviors could be very different even when the conditions used have only small differences.

In this paper, in order to address the requirement on device characterization in our study, as well as to improve the accuracy, reliability and reproducibility of dopant concentration extraction, several considerations related to the mechanism of the DSE/TEM technique are addressed: (i) the chemical etching behavior has isotropic properties and the etching rate is considered as a vector; therefore the direction of the absolute etching rate is assumed to be perpendicular to the local exposed surface of doped and undoped silicon material. (ii) The etching time and TEM sample thickness are optimized, in order to obtain highly accurate doping evaluations by doping-dependent etching. The initial TEM sample thickness, prior to DSE processing, was directly measured at the end of the FIB-TEM sample preparation. (iii) The successive maxima and minima in intensity, the bright and dark fringes, are plotted; and finally this

technique is applied to evaluate dopant concentrations of LDRs in comparison with numerical simulations.

4.3 EXPERIMENTAL DETAILS AND PROCEDURES

In this section, all experimental details, including a detailed modeling and calibration, are given. The technique developed will be used to profile the dopant distribution in LDRs and could also be used for any actual CMOS microdevices.

4.3.1 EXPERIMENTAL DETAILS

The calibrating standards were made using an n-type Si (100) wafer starting with a resistivity of 10 ohms•cm, implanted with boron (B) at 20 KeV at a dose of 5.0×10^{14} atoms/cm^2; followed by rapid thermal annealing (RTA) at 900 ^{0}C for 30 s. Those specific fabrication parameters were similar to the processing conditions for fabricating heavily doped regions of CMOS devices, the nominal source and drain regions, used in producing the LDRs.

TEM samples, with a wide range of uniform thicknesses were prepared by a HITACHI FB-2000A focused ion beam (FIB) instrument, using Ga ion beam milling. There are several principle advantages in this sample preparation in combination with DSE technique for dopant calibration and thus distribution quantification. First of all, as opposed to conventional sample preparation, the initial foil thicknesses can be directly

measured during FIB-sample preparation before DSE and TEM imaging. As we had shown, this step is very important because the chemical solution could attack all of the materials in IC devices, including silicon nitride and silicon oxide, at different etching rates, which will affect the reliability and reproducibility of dopant analyses. Secondly, starting thin films with accurately equal thicknesses and high surface quality can be prepared and reproduced. In highly accurate and highly reproducible dopant evaluation, a TEM sample film with equal starting thickness, which should be 600 nm or less as will be shown below, is important to avoid initial fringes which might be created by Ar^+ milling caused in the conventional sample preparation process. The thickness fringes raised from initial TEM samples, if present, will interfere with the interpretation of the thickness fringes created by selective chemical etching in regions being analyzed. Thirdly, wedge-shaped samples with exactly equal wedge angles can be prepared, which is used for dopant calibration. Using the lift-out technique [180] of FIB-TEM sample preparation, two wedged samples were mounted in the same molybdenum (Mo) TEM sample grid prior to the final milling steps. This calibration method has higher accuracy than that used in conventional dopant calibration by AFM [124] due to tip shape effects in the latter. Finally, FIB can be used to prepare a specific site in a microdevice such as laser locally diffused areas with high precision.

The selectively etched samples were analyzed using a Philips CM30 TEM system operating at an accelerating voltage of 300 kV. Due to the marked dependence of the effective extinction distance (ξ_{eff}) on the transmission diffraction condition, the multi-beam excited zone axis condition is used to obtain high spatial resolution. In this

study, all TEM images were taken on the <011> zone axis and the diffracting condition

for such thickness fringes are typically seven beams selected by the objective aperture.

Therefore, the number of equal thickness fringes and, hence, the capacity to measure

very small variations of thickness, may be maximized by the reduction in ξ_{eff} resulting

from on-axis imaging. As a consequence of the 1D SIMS boron profile taken from the

standard wafer, the 2D dopant concentration profiles of LDRs were then extrapolated by

following the equal thickness fringes far from the laser-diffused areas.

4.3.2. ETCHANT CHEMISTRY AND SURFACE QUALITY

HNO_3 drives the oxidization of silicon to form SiO_2, while HF attacks oxide with

a lower activation energy, so that the selectivity is mainly controlled by the HNO_3

solution. A wide range of mixture ratios of hydrofluoric acid (HF), nitric acid (HNO_3)

and acetic acid (CH_3COOH) (collectively, HNA) were tested before the final analysis.

When the concentration of CH_3COOH in the solution is too high or when the chemical

etching process occurs under dim illumination, the etching rate becomes very low and

the dynamic range of dopant-reflecting selectivity is reduced; furthermore, Si was

mainly amorphized with the probable introduction of porosity under stain-etching

process [181]. Therefore, TEM images taken from those etched samples are not ideal for

dopant concentration evaluation. The experimental results reported here are obtained

from a mixture of HF (49%), HNO_3 (70%) and CH_3COOH (80%) with ratio of 1:3:8,

under standard clean room conditions involving ambient illumination and a temperature

of 21±1 ^{0}C. The reproducibility of the DSE process is ensured by maintaining constant ambient conditions.

The etching behavior of doped silicon may also be significantly affected by the initial surface conditions, including surface roughness and damage. The etching selectivity depends only on the electrically activated boron [182], and it is lost when silicon is amorphous. In order to avoid Ga deposition and Si electrical damage on the prepared FIB-TEM sample surface, cross-sectional observation should be avoided and the milling beam should be aligned [183] and parallel to the surface being milled. Moreover, one low current beam (0.346 nA) should be used at the final milling step. Before final dopant selective analyses, AFM indicated that the root-mean-square (rms) surface roughness was less than 0.7 nm over a scan area of 1×1 μm^2 for each sample, better than that of a sample surface prepared by conventional mechanical polishing with 0.05 μm colloidal silica. The Ga contamination on the surface that could affect the DSE process is minimal, since no Ga signal was detected by EDX (Energy-dispersive X-ray spectroscopy), having a sensitivity of ~ 0.1 at. %, and no Ga precipitates were formed on the sample surface, as verified by TEM observation.

4.3.3. DETERMINATION OF ETCHING TIME AND TEM SAMPLE THICKNESS

In this study, the model by considering the etching rate as a scalar is called the scalar model and the model by considering it as a vector is called vector model. Based

on the simulation study of the chemical etching behavior related to the vector model, one knows that the etching time and TEM sample thickness are two important factors affecting the reliability of non-uniform dopant extraction.

The thinned thickness due to selective etching was measured by wedge-sample preparation and TEM imaging. Concerning TEM sample preparation, a notched Mo TEM sample grid, shown in Fig. 4.1 (a), is first milled to obtain one concave hole (two holes for calibration), following which, the TEM sample, obtained by lift-off from the IC, is mounted in this hole, using W deposition by FIB. Then, the TEM sample is thinned to various shapes, as shown in Fig. 4.1 (b) and (d), for different experimental purposes. In order to measure the etched thicknesses related to the etching rates, TEM samples, as shown in Fig. 4.1 (b), was wedge-shaped, with the angle $\beta=10^0$ after final milling. Fig. 4.1 (c) shows one example (taken from the heavily doped regions of non-irradiated device as indicated in the frame part of the inset schematics at the right top corner) of the etched shape after the selective etching process. As expected, the hole in the doped region also shows a wedge shape. At the thin side of the samples, both the heavily doped region and the low doped regions are completely etched by the chemical solution; however, at the thick side, only the heavily doped regions were completely etched away. Those different behaviors reflect the variation of the dopant concentration as a function of depth, considering that for a given depth the dopant concentration remains constant. Along the hole edge in Fig. 4.1 (c), (indicated by the dots) the measurement of l, which is the distance between the dots and edge of the initial sample, permits the calculation of the etched thicknesses d by using the equation
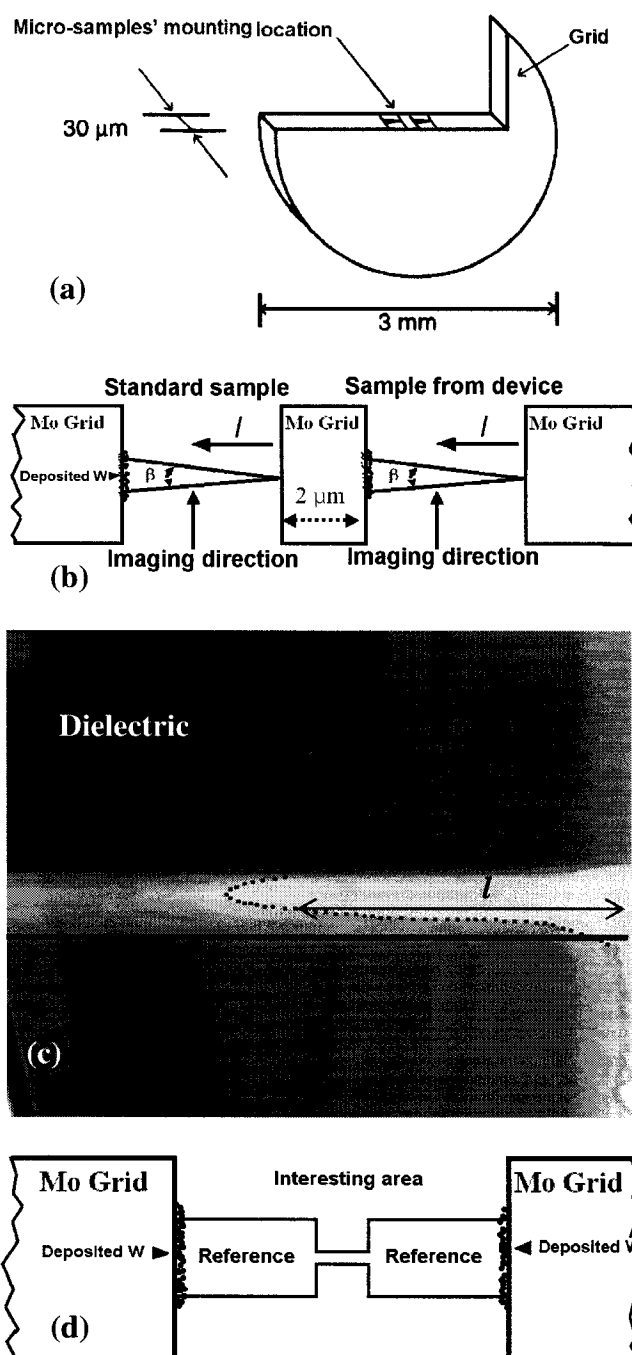
Fig. 4.1 Schematic illustration of etched thickness measurement method due to chemical selective etching: (a) Side view of notched TEM sample grid for micro-sampling; (b) Top view of TEM samples mounted in the grid after wedge-shaped milling process; (c) Cross-sectional TEM image of wedge-shaped sample after selective etching for evaluating thickness as a function of depth; (d) Top view of TEM sample used for dopant evaluation of microdevices.

$$d = 2l \bullet \tan(\beta/2) \qquad\qquad (1)$$

Here, d is the total etched thickness from the two sides, and l is the vertical distance from the initial edge of the wedge sample. This calculation takes into account the 3-D attack of the etching solution on the TEM samples.

Fig. 4.2 (a) shows the dopant profile from the boron concentration peak to the silicon bulk of the standard wafer, described in the section on experimental details, above, obtained by SIMS measurement. We assume the etching rate is a vector, perpendicular to the local etching surface and the vector direction changes in two-dimensional plan (f and g coordinates). At the beginning of the etching process, the rate vector is normal to the FIB-prepared flat sample surface, expressed as $v_\perp$; however, the etching direction changes depending on the etched surface shape related to the etching history of each etching site and its adjacent sites in g-f plan. Therefore, the etching rate vector can be transformed into two components, $v_\perp$, perpendicular and $v_{//}$, parallel to the sample surface, which may be express as following:

$$v_{//} = \frac{\partial g}{\partial t} = V(c,t,\mu)\sin\alpha \qquad\qquad (2)$$

$$v_\perp = \frac{\partial f}{\partial t} = V(c,t,\mu)\cos\alpha \qquad\qquad (3)$$

where α is the angle between the tangent line, corresponding to the etching interface between the silicon and the chemical solution, of the local etching site and the initial surface of the cross-sectional sample, as shown in Fig. 4.2 (b). $V(c,t,\mu)$ is the absolute etching rate at position (g) reflecting the dopant concentration (c), the etching time (t)
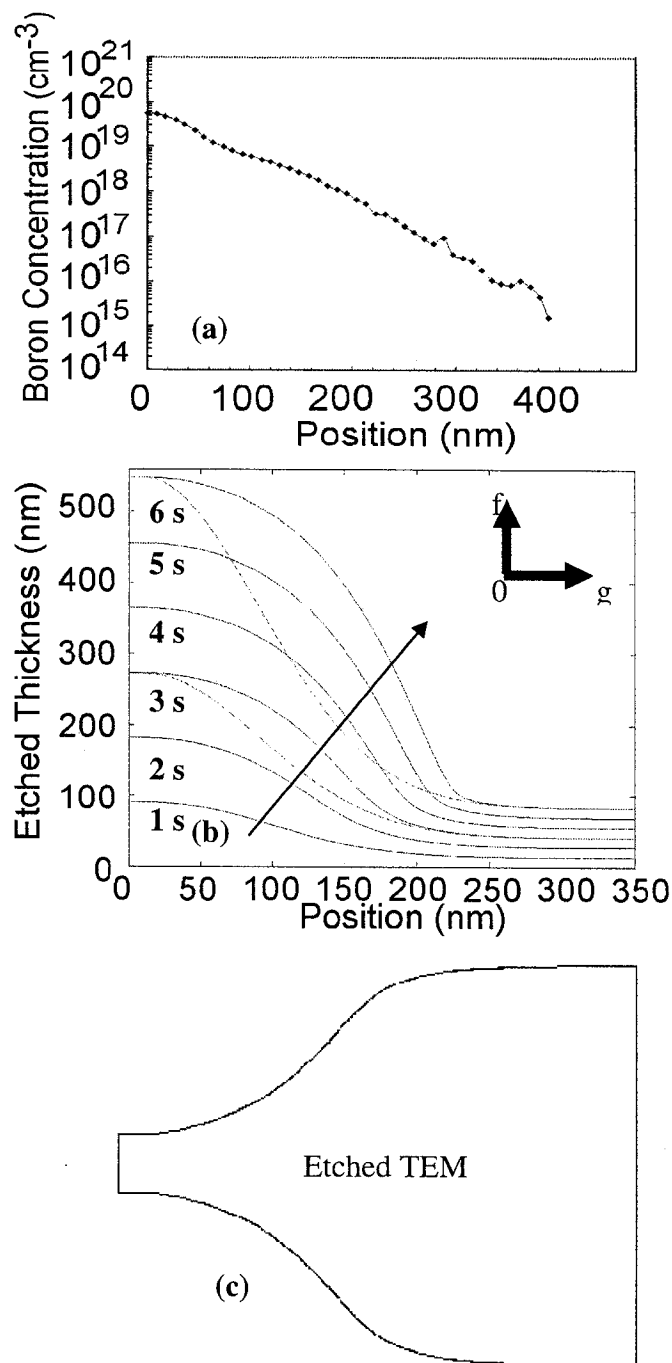
Fig. 4.2 Simulation of DSE behaviour performed on a cross-sectional standard sample: (a) partial SIMS boron concentration profile of the standard sample from the distribution peak towards the bulk silicon.. (b) The solid curves along the arrow indicate the etched thickness after 1, 2, 3, 4, 5, and 6 s chemical etching simulated by the vector model using two differential equations, and dash-dot curves along the arrow indicate the etched thickness after 3 and 6 s chemical etching simulated by the scalar model. (c) Schematics of TEM sample after DSE-etched from both sides.

and other parameters (μ) such as the chemical solution, the temperature, etc [179] [124] [116] [114]. The calculations of this simulation are based on the absolute etching rate, which is extracted, using a vector model and equation (1), from the etched structure and dopant profile in Fig. 4.2 (a), after 3 s of chemical etching.

By solving the two differential equations above, the time-dependent etching thickness at each position can be obtained. We assume that the absolute etching rate under certain etching conditions is independent of etching time. Therefore, the absolute etching rate is only a function of position corresponding to the dopant profile under certain etching condition. In order to clearly illustrate the simulation data of the etching behaviour, as shown in Fig. 4.2 (a), only the dopant profile from the concentration peak toward the bulk silicon, extracted from Fig. 4.3 (a), is used. The positions in Figs. 4.2 (a) and (b) represent the depth of the local point from the dopant distribution peak. The simulated curves, using this dopant profile, are shown in Fig. 4.2(b).

The solid lines following in the arrow direction reflect the etched silicon thickness based on a vector model, containing $v_\perp$ and $v_{//}$ factors determined by equation (2) and (3), respectively, after 1 to 6 s of chemical etching. The two dot-dash curves along the arrow direction indicate the etching thickness after 3 and 6 s chemical etching simulated using the scalar model with conventional scalar etching rate $V(c,\mu)$. All those calculations are based on the assumption that the absolute etching rate can be extracted from the measured thickness profile after 3 s of chemical etching. As shown in the Fig. 4.2 (b), the difference of the computed etched thickness obtained from the two models becomes greater with increasing etching time. The most significant difference is

in the middle region, between the two locations with the highest and lowest dopant concentrations. Furthermore, the sensitivity of the dopant selective etching technique for electrically activated boron atoms, indicated by the deepest visible thickness fringe close to the undoped bulk Si side, is 9×10^{16} atoms/cm^3 in concentration, located at a depth of 254 nm. However, the last possible thickness fringe after 6 s or longer etching time, deduced from the simulation, moves to the right side, leading to a bigger etched hole. Another issue, which should be considered, is that the etching time should be long enough to have final thickness variations, among areas with different doping levels, greater than the extinction distance for observing the fringes. In practice, for the dopant characterization of industrial shallow junction and LDRs, the optimized etching time is 3 s, which gives a good compromise between the reliability of the dopant extraction and the fringe formation. It was verified, by vector simulation, that the inaccuracy of the extracted dopant profile due to the etched hole is less than 1% when the etching time is 3 s. The etching time is controlled by using a tenth-second timer with an error of less than 5%, which is reasonable to ensure a uniform and reproducible wet etching process.

A further consideration is the TEM sample thickness. As is well-known, the dopant concentration extraction technique is based on the etched TEM shape and thickness fringes observed under electron diffraction. Because of the decrease in intensity, due to factors such as inelastic scattering [184], with an increase in sample thickness, the TEM sample cannot be too thick. The acceptable range of the initial TEM sample thickness for dopant concentration analysis for the LDRs is around 600 nm. For an etching time of 3 s and an initial TEM sample thickness of 600 nm, the sensitivity of

boron evaluation based on this technique is 9×10^{16} atoms/cm^3, by considering that the TEM samples are etched from both sides as indicated in Fig. 4.2 (c), which can satisfy the LDRs, as well as other microdevices.

4.3.4. Calibration

In order to determine the quantitative dopant concentration in the resistive link formed by laser technology, it is necessary to calibrate the dopant concentration in the nominal source/drain regions. For highly accurate calibration, the samples must have similar structures and similar dopant concentration gradients. The 1D dopant profile of the standard sample as shown in Fig. 4.3 (a) was obtained using SIMS.

As schematically shown in Fig. 4.1 (b), two TEM samples, one taken from the standard wafer and one from the source/drain regions in a non-laser-irradiated device, with a small distance of about 2 μm between both samples, were prepared and mounted on the same notched Mo grid, shown in Fig. 4.1 (a), using tungsten (W) deposition by FIB. The two TEM samples were then wedge-shaped, with the same angle ($\beta=10^0$) after final milling. These TEM samples were used to calculate the etched thickness, by using equation (1), for dopant calibration. In addition, according to the principle of our vector simulation analysis, the etching behavior of any local point is affected by the adjacent points. Therefore, in order to have a high accurate calibration, the two TEM samples should have similar dopant concentration gradients. In this way, the related etched thicknesses are accurately obtained under the same chemical etching conditions,
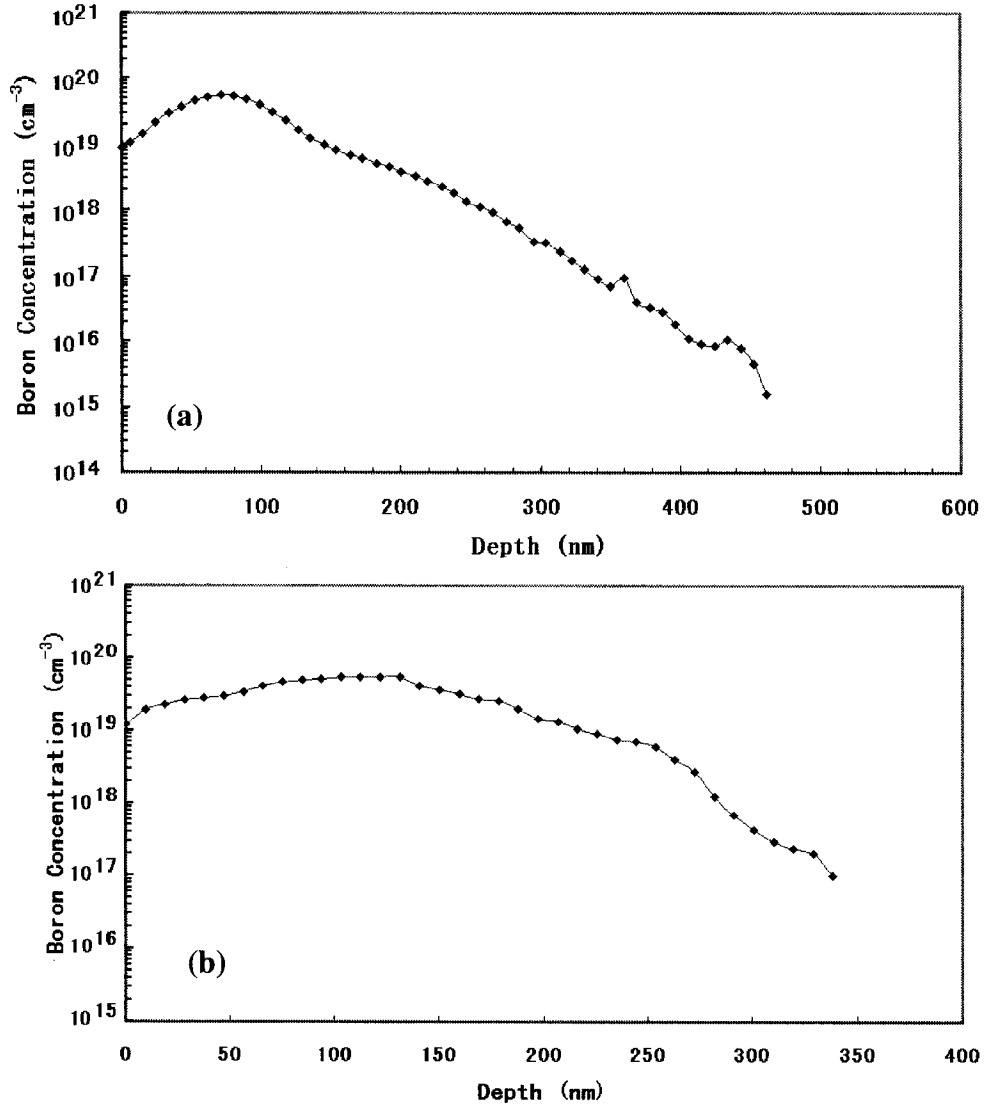
Fig. 4.3 (a) SIMS profile shows the 1D boron distribution in standard

sample; (b) Calibrated 1D boron profile in the heavily doped regions

of non-irradiated devices.

including HNA components, temperature, illumination, and 3 s of etching time, by

following the method described above. The dopant profile, from low dopant

concentrations to high dopant concentrations, in the non laser irradiated source and drain regions of the LDRs (which will be discussed in next section) are calibrated by the 1D SIMS dopant profile of the standard sample shown in Fig. 4.3 (a) and quantified as shown in Fig. 4.3 (b). The reason that the profile contains a smooth peak is possibly that boron atoms, in the high dopant concentration region, are not fully activated and/or the etching rate is saturated. From the dopant profiles, it can be deduced that the ranges of the dopant concentrations between the sample taken from our device and the sample taken from the standard wafer are almost the same; however, the doped depths between them are different. Based on our experiments, it should be mentioned that the calibrated data, obtained by our novel method, are more reproducible, reliable and accurate than those obtained by other techniques such as scanning capacitance microscopy (SCM), limited by sample structure, and atomic force microscopy (AFM) in combination with DSE, limited by the tip shape. Our calibration measurements have been repeated four times and all the profiles are similar, with an error of less than 5 %.

4.4. DOPANT PROFILING OF LDRS

Fig. 4.4 shows the cross-sections of two different types of gateless transistors with a nominal source to drain distance of 0.6 μm. The rounded shape of the oxide layer in Fig. 4.4 (a) is caused by the field oxidation process and was used to mask the implants (boron atoms) due to the absence of the gate between the highly doped regions. Fig. 4.4 (b) shows one flat device with two heavily doped regions. The doping atoms diffuse

from the highly p-type doped regions to the lightly n-type doped gap region when a laser beam is focused on the center of the gap region and the edges of the adjacent heavily p-type doped regions connecting to the gap [4]; thus a resistive link with a medium dopant concentration is formed. Field-effect and flat LDRs, with resistances of 500Ω and 230Ω, respectively, are produced with 100 laser pulses, 3.0 W of power, and 80 ns of a pulse width, and are analyzed in this study.

Before dopant analysis, the TEM samples taken from LDRs were observed using TEM and had not significant structural differences from the non laser irradiated devices shown in Fig. 4.4. It should be mentioned that, during DSE, the Si material close to the dielectric/Si interface in the heavily doped source and drain regions, adjacent to the resistors, would be completely etched away, losing the reference for measuring the etched depth. To overcome this problem, two very thick areas in source and drain regions as shown in Fig. 4.1 (d), were also prepared by FIB; since these thick areas were essentially not affected by the 3 s of chemical etching process, they can be used as references for measuring the depth of all the fringes. Following 3 s chemical etching, Fig.
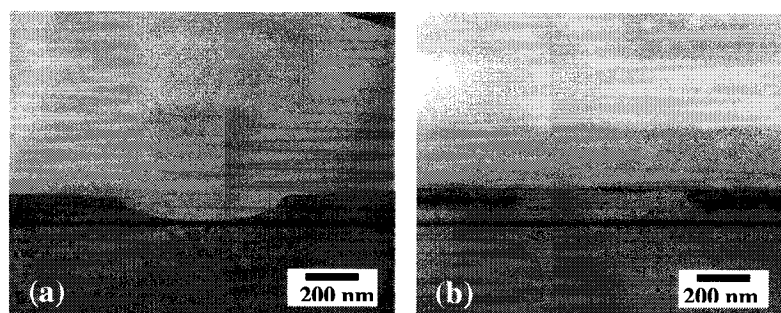
Fig. 4.4 Two different types of microdevices before
LFT process: (a) field-effect device; (b) flat device.

4.5 (a) shows the multi-beam TEM image of one LDR. Corresponding to the structure of

Fig. 4.4 (a), the micro-resistor formed is located underneath the dielectric and between

the two heavily doped regions. In the resistance region, there are 6 dark fringes observed

after DSE process. The last equal thickness fringe indicates that the laser-molten depth is

113 nm underneath the interface, between the dielectric and the diffused resistor. In this

device, the effective resistance length, which is considered to be the region with a

dopant concentration lower than that along the dotted curves, between the hole and

silicon material left, with a boron concentration value of 5.9×10^{18} atoms/cm^3, is 417 nm.

By following the equal thickness fringes in the heavily doped regions without laser

irradiation, far from the laser-molten areas and indicated as dash-dot curves in Fig. 4.5

(b), iso-concentration profiles, corresponding to the equal thickness profiles in the

diffused resistance link, are obtained. Iso-concentration curves, delineated as solid lines,

were plotted from the dark fringes of the original TEM micrograph shown in Fig. 4.5 (a).

Moreover, as shown in Fig. 4.7, the dopant concentrations corresponding to from the

first to sixth solid curves marked by the direction of the arrow in Fig. 4.5 (b), are 3.6, 1.8,

0.65, 0.36, 0.36 and 0.24×10^{18} atoms/cm^3, located at depths of 0, 8, 38, 83, 101, and 113

nm, respectively. The reason that curve 4 has the same dopant level as curve 5 is that

both of them are extended from the same dopant level curve in the heavily doped region,

which could be seen on the left side of the resistive link. The grey area marked A, has an

almost uniform dopant concentration, with a value of 1.8×10^{18} atoms/cm^3, determined

by following the dark fringe 2.

Fig.4.6 (a) shows one multi-beam TEM image, after selective etching performed on a flat LDR with the initial structure shown in Fig 4.4 (b). The dash-dot curve in Fig. 4.6 (c) obtained from the last fringe, which is a white equal thickness fringe in Fig. 4.6 (a), indicates that the maximum molten depth along the arrow is 270 nm. The dopant concentration along the boundary between the etched hole and the left silicon materials is 8.9×10^{18} atoms/cm^3. Along the arrow, there are four areas: two grey areas, one shaded area and one fringed area. Fig. 4.6 (b) was taken from one beam imaging condition; there is no diffraction contrast and, thus, the contrast reflects mainly the material thickness. This image shows that the material thickness in the three upper areas (two grey areas and one shaded area) is almost uniform, indicating that the net electrically activated dopant concentrations in these three areas are nearly uniform. The two grey areas in Fig. 4.6 (a) do not present diffraction contrast and, in the shaded area, dark contrast is visible under multi-beam diffraction conditions. It is believed that the materials in the two grey areas are very thin and amorphized after chemical etching [185]. The upper grey area was etched at a high rate due to the high concentration of vacancies formed under laser irradiation. The lower grey area contained electrically activated boron atoms with a little higher concentration than the fringed area. The shaded area contained thicker silicon material than the lower grey area, revealed by diffraction contrast from the local crystalline film, probably because acceptors were partially compensated by oxygen-related donors [68] formed due to oxygen diffusion from dielectric layer during laser irradiation. Because the thicknesses of the two grey areas and the shaded area were almost completely etched, the dopant concentration in

these three areas could be considered the same as that of the boundary between the hole

and the left silicon material of the fringe area, which is 8.9×10^{18} atoms/cm^3. The dopant

concentrations of the solid curves 1, 2 and 3 in Fig. 4.6 (c) are 7×10^{18}, 3.4×10^{18} and

2.6×10^{18} atoms/cm^3, respectively. The dopant concentration of the dot-dash curve,

plotted according to the white fringe in Fig. 4.6 (a), is 2.2×10^{18} atoms/cm^3.

4.5. DISCUSSION

Previously, our research group [18] have studied laser induced melting and

solved the heat transfer equation to obtain the three-dimensional out-of-equilibrium

transient temperature field (T(r,t)). It has been shown that the actions of heat transfer

from laser to materials as well as from molten pool to solid Si substrate can be described

accurately with the modeling. Knowing T(r,t), one can use Fick's law $\partial C/\partial t = -D\nabla C$

to obtain the boron profile by considering that the dopants diffuse in the liquid with a

diffusion coefficient of $\sim3.8\times10^{-4}$cm^2/s in liquid Si [19] and assume that B doesn't

diffuse in the solid phase because the maximum diffusion coefficient in the solid at

melting temperature is $\sim 4\times10^{-11}$cm^2/s [186], leading to a negligible diffusion distance

$\sqrt{Dt}$ of ~0.03 nm with a typical melting time of 200 ns. In order to confirm the physical

mechanism of the LFT process, numerical simulations were performed on dopant

diffusion. Fig. 4.5 (c) and Fig. 4.6 (d) show the simulated 2D dopant distribution

obtained by considering the processing calibration given in the last section with an initial
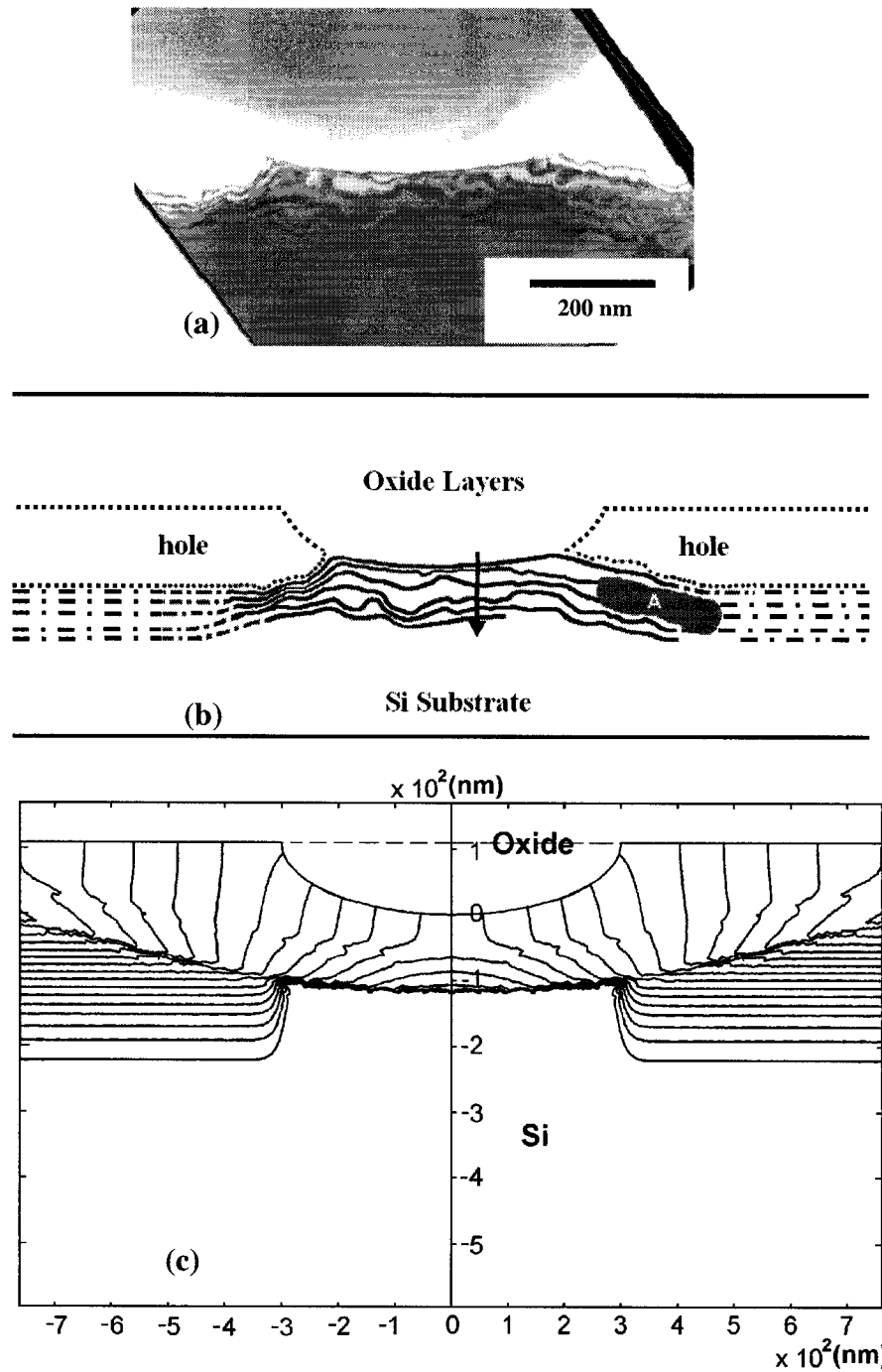
Fig. 4.5 (a) TEM image revealing thickness fringes as a result of dopant-level-dependant etching for 3 s. (b) Skeletonized micrograph showing the extracted dopant iso-concentration contour of the LDR. (c) Simulated 2D dopant profile.

doping profile in the source/drain regions given by the Fig. 4.3 (b). The spatial

resolution of the developed methods for dopant calibration and 2D evaluation is 1 to 5 nm, depending on the local dopant concentration gradient. Using these methods, the plotted data, extracted from the dark fringes along the arrow shown in Fig. 4.5 (b), are indicated by the points shown in Fig. 4.7. In addition, the plotted data, extracted from the boundaries of the areas with different contrasts, shown in Fig. 4.6 (a), dark and bright fringes shown in Fig. 4.6 (c) along the arrow positions, are shown in Fig. 4.8. The arrows represent the average values of dopant concentrations for all the iso-concentration curves in each device. Fig. 4.7 and Fig. 4.8 also show simulated 1D profiles, plotted along the center of Fig. 4.5 (c) and Fig. 4.6 (d), respectively. Obviously, iso-concentration lines in the resistive links, as shown in Fig. 4.5 (b) and Fig. 4.6 (c), are not straight lines; thus we use error bars, calculated by considering the dopant concentrations along each arrow as references, to indicate the dopant concentration variations inside the links. These dopant variations in the resistive links are first due to the diffusion of a non uniform dopant distribution during the laser-induced melting process as revealed by Fig 4.5 (c) and Fig. 4.6 (d) and, second, due to the local non-uniformity of heat absorption and diffusion in the actual Si materials. These profiles, after considering the reasonable error, are reproducible and reliable for different fabricated resistors based on the same initial structures and laser conditions, which cannot be obtained by conventional dopant evaluation techniques. It is also verified by resistance simulation (not shown here) that the evaluated dopant profile is highly accurate. Clearly, the entire quantified experimental dopant profiles, described in Fig. 4.7, and the one, in the deep region in Fig. 4.8, match the simulated dopant profiles,

200 nm

200 nm

(a)

(b)

Dielectric Multilayers

1   3

1   2

Link

(c)   **Si Substrate**

x 10^2(nm)

-1
0
Oxide
-1
-2
-3
-4
-5
-6
(d)   -7   Si
-8

-10   0   10   x 10^2(nm)
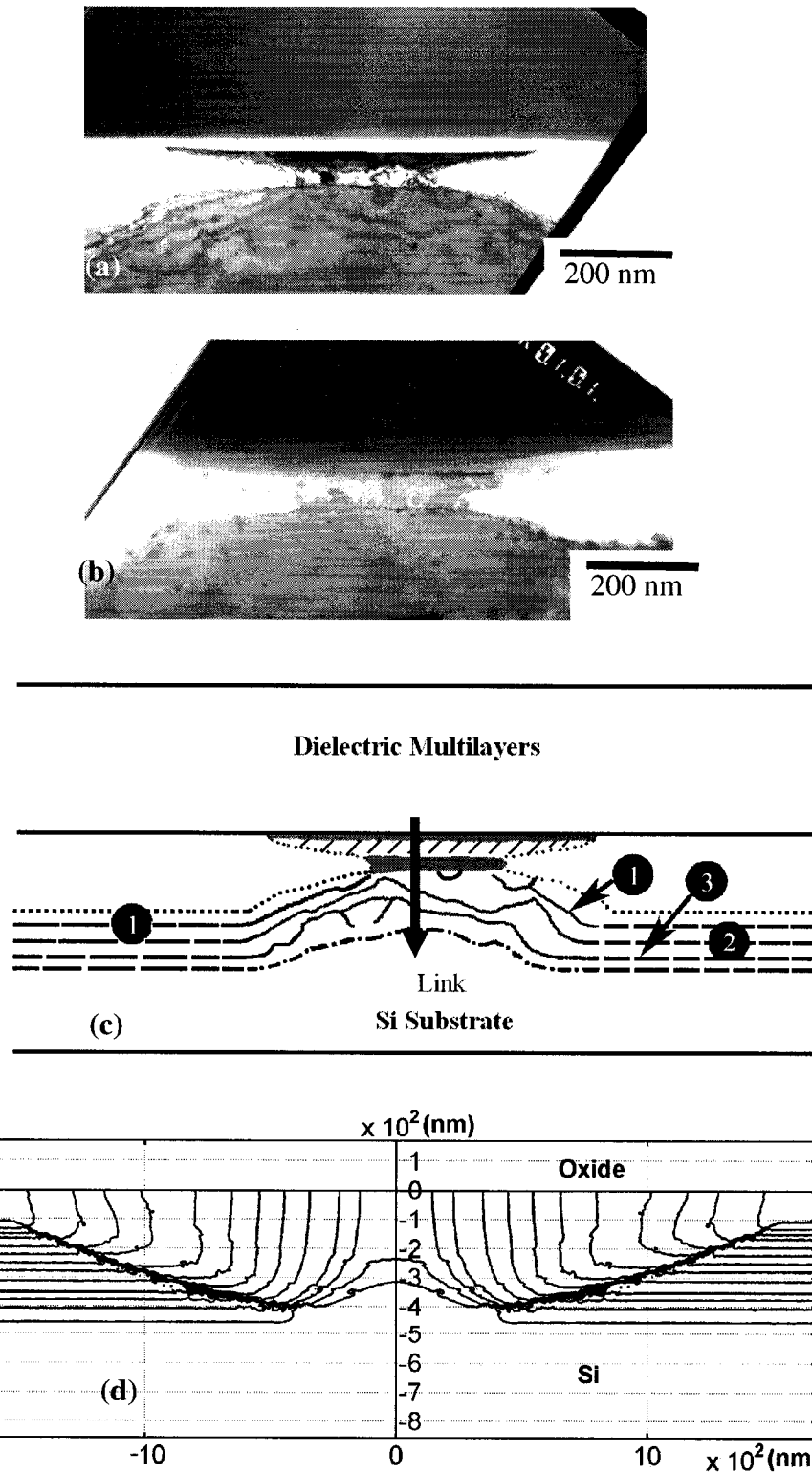
Fig. 4.6 (a) TEM multi-beam image taken from one flat LDR after DSE, (b) one beam TEM image showing the left etch-amorphized material in the upper part of the resistive link, (c) plotted dopant profile corresponding to the TEM images, and (d) simulated 2D dopant distribution.
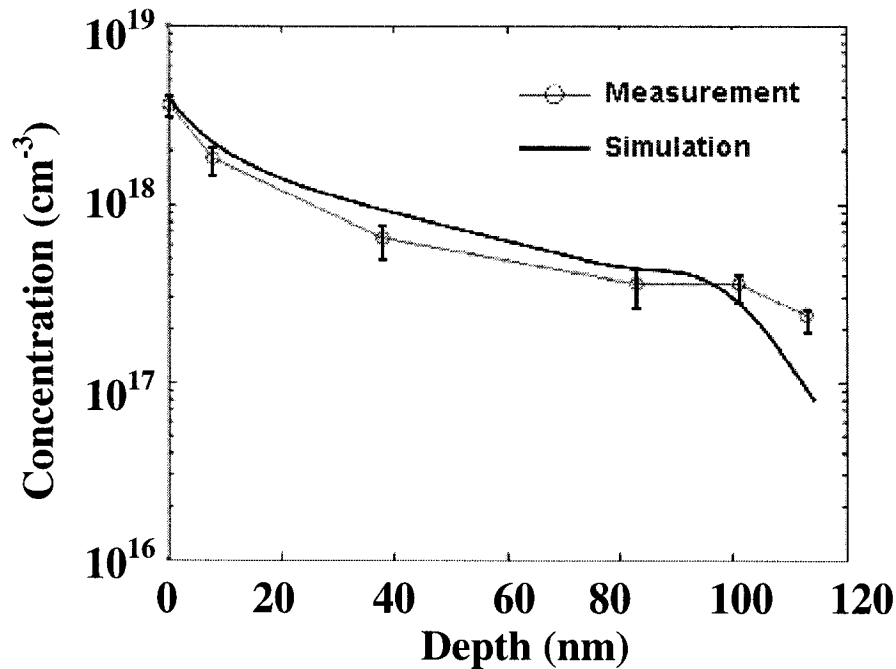
Fig. 4.7 1D experimental dopant profile along the arrow in Fig. 5.5 (b)
and simulated depth profile along the melting center in Fig. 5.5 (c).

which indicates that the dopant concentration decreases in this melting volume when it

becomes deeper. However, as indicated in the 2D dopant distributions as shown in Fig.

4.6 (c) and (d) and the 1D profiles in Fig. 4.8, experimental data are different from

simulated data in the near interface region probably due to oxygen-related donor

compensation. Furthermore, from the simulations, it could be understood that under the

same laser-processing conditions, the molten depth and volume in the flat LDRs are

deeper and larger, respectively, than those in the field-effect LDRs, due to the light

reflection difference caused by the shape difference of the laser-irradiated interface

between the dielectric and Si gap. Finally, the dopant concentrations decrease with

increasing depth for both LDRs, because the melting duration is shorter with increasing
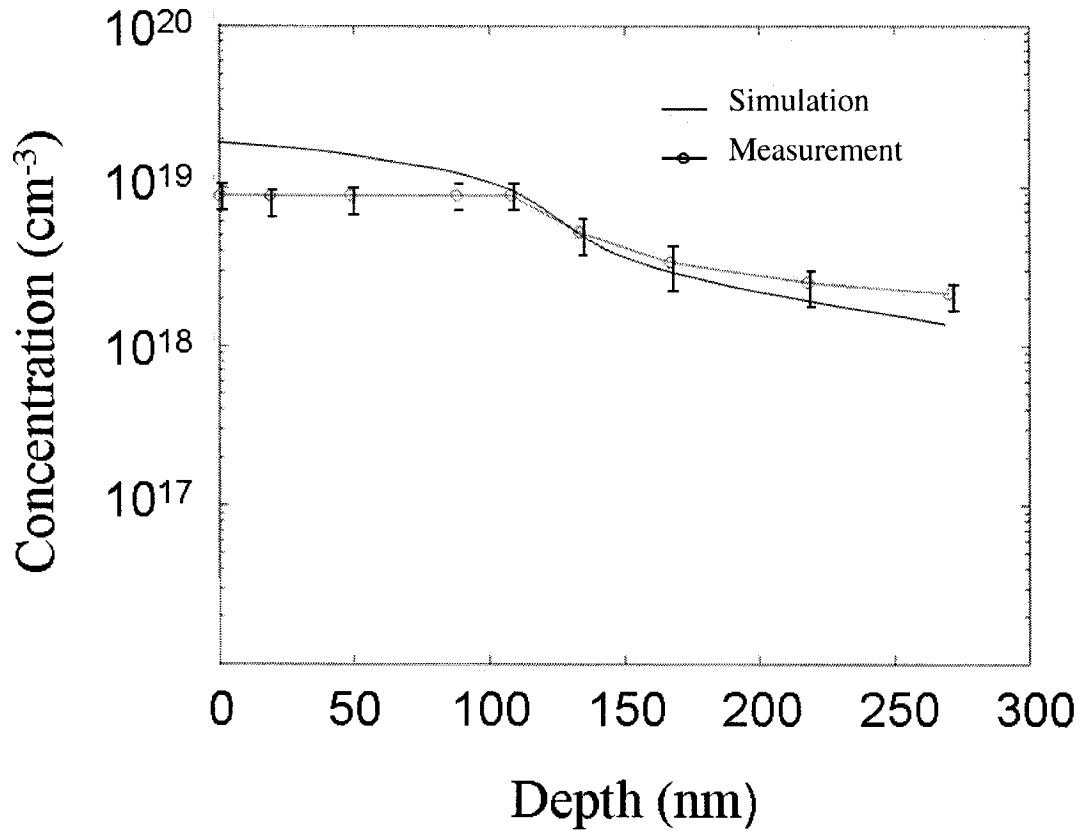
Fig. 4.8 Quantified dopant depth profiles (1D) along the arrow and along
the melting center in Fig. 5.6 (c) and Fig. 5.6 (d), respectively.

depth since the heat released from the molten silicon into the dielectric was much less

than that into the silicon.

4.6 CONCLUSION

The selective etching process was, for the first time, modeled so that the

reliability, accuracy and reproducibility of dopant extraction by DSE have been

improved. It is pointed out that when the TEM sample thickness is around 600 nm and

the etching time is 3 s, the etched camber shape in the doped regions may be considered to be plane, parallel to the initial surface of TEM sample and, thus, the etched profile can be directly measured for extracting credible dopant concentration. A novel FIB sample preparation allows one to obtain TEM samples for dopant calibration under the same chemical selective etching conditions. Finally, developed quantification technique had been used for dopant evaluation on LDRs, fabricated with small laser spot size, and the results are in good agreements with numerical simulation obtained by solving heat transfer problems and diffusion equations. It seems reasonable to consider the role of acceptor compensation by oxygen-related donors due to laser-induced oxygen diffusion and activation. The excellent dopant delineation shows that the improved DSE technique is a practical technique for the highly accurate quantification of 2-D dopant distribution of LDRs and we believe that it has a good potential to be effectively used for other types of micro-devices.

Acknowledgments

CHAPTER 5. LASER INDUCED FORMATION OF PERIODIC NANOSTRUCTURES IN SILICON COVERED BY SiO_2 (ARTICLE 2)

Yougui Liao, Jean-Yves Degorce and Michel Meunier*

Laser Processing Laboratory, Ecole Polytechnique de Montreal, Case Postale 6079,

Succursale. Centre-ville, Montréal (Québec), Canada, H3C 3A7

Fax :   1-514-340-3218

Tel :   1-514-340-4711 x 4971

Email: *Michel.Meunier@polymtl.ca

5.1 ABSTRACT

Three-dimensional (3-D) and two-dimensional (2-D) periodic silicon nanostructures formed by polarized focused Nd:YAG laser irradiation (532 nm) with spot size less than 3 μm on Si covered by SiO_2 are presented in this paper. We observed that at a low laser intensity I range, from I=0.9 to 1.08 W, 2D periodic coexisting of liquid and solid exists, while for 1.08<I<1.44 W, 3D periodic ripples were formed. However, when the light intensity is out of those ranges, either no melting was created (I<0.9 W) or the periodicity was destroyed (I>1.44 W). The periodicity of these periodic structures is 360 nm related to the wavelength of frequency doubled Nd:YAG laser and the index of refraction of SiO_2. We propose a model based on the fact that as the oxygen is diffusing locally from SiO_2 into the melted Si, thus forming SiO_β with a lower melting

point, successive pulses melt preferentially these regions giving rise to a positive feedback. This dynamic nanoscale modeling, based on variations of melting points of Si and dielectric and reflection coefficient, confirms the experimental results.

PACS numbers: 81.07.–b, 81.10.Fq, 61.80.Ba, 66.10.Cb

5.2   INTRODUCTION

Spontaneous ripples [187-192], formed after intense irradiation of a single or multiple laser beam(s) operating at wide optical wavelengths, with pulse durations ranging from continuous wave (cw) to femtosecond pulses [191-194] [205-207] [196-198], were frequently observed on the blank surface of a variety of materials [188-189] [194-196] [198] [208-214], such as dielectrics, semiconductors and metals, and were considered as a mixture of solid and liquid at a temperature close [187] to the melting threshold. Emmony et al. [189] for the first time proposed that a scattering center on the surface might be responsible for the observed periodic topography. It has been suggested that theses ripples [189] arise from standing waves produced by one instability and developed as a result of interference of incident laser light with scattered electromagnetic waves from a surface disturbance [188] [197-198]. When the light intensity is sufficiently high, the melting threshold of the surface is periodically exceeded, and thus rapid regrowth of a thin layer of molten material induces a constructive topography. The ripple periods are mostly found to follow Rayleigh's diffraction criterion [196] [198].

In this paper, we report the formation of periodic nanostructures in Si covered by SiO_2. In our case the polarized laser beam is normal to the sample surface, therefore, the periodicity of the nanostructures, including coexisting of liquid and solid as well as ripples, is $\Lambda = \lambda/n$ [196], where Λ is the wavelength of the standing wave and thus the

periodicity of our nanostructure, λ is the laser wavelength, and n (~1.5) is the refractive index of SiO_2. It is found that the polarization is vertical to the formed ripples or the melted strips. We observed not only ripples but also flat coexisting of solid and liquid, formed by a focused (in diameter of 3 μm) Nd:YAG frequency doubled laser (λ=532 nm) under different light intensities schematically shown in Fig. 5.1. The proposed formation mechanisms of the two phenomena with periodicity of 360 nm, which is different from the previous studies [217], are based on a locally and spatially periodic oxygen diffusion induced by the laser irradiation as it is clearly revealed by chemically selective etching. A model, supported by a three dimensional (3-D) numerical simulation, is proposed to explain the formation mechanisms of the periodic nanostructures.

5.3 EXPERIMENTAL DETAILS

Samples were obtained by conventional microelectronics fabrication flow and consisted of a gateless field effect transistor where the silicon is covered by many dielectric layers, including SiO_2, SiO_xN_y, and Si_3N_4. Two heavily doped p-type regions (boron concentration at ~ 5×10^{19} atoms/cm^3) have a doped depth of 170 nm and are separated by a lightly As doped gap (concentration at ~ 10^{15} atoms/cm^3) with a distance of 600 nm. This structure is more commonly used in the laser induced dopant diffusion to form a highly accurate resistance for analogue microelectronics [4]. This structure is also helpful to reveal the nanostructures based on oxygen diffusion. The TEM (transmission electron microscopy) and SEM (scanning electron microscopy) samples

were prepared by a HITACHI FB-2000A focused ion beam (FIB) instrument using Ga ion beam milling. The main advantage in this sample preparation is that the interesting area, involving the interface between the oxide and the Si substrate (for TEM observation) and, the gap location (for SEM observation), can be precisely located. After FIB preparation, the samples were etched using HF (49%) and HNA [HF (49%):HNO$_3$ (70%):CH$_3$COOH (80%)=1:3:8] for TEM and SEM observations. For AFM imaging, the dielectrics layers above Si in the samples were etched by HF (49%). The etching rate of Si in solution of HNA is extremely higher than that of dielectric materials.

5.4   RESULTS AND DISCUSSION

We observed two types of topographic phenomena, as shown in the AFM images in Fig. 5.2 taken after etching the dielectric multilayers using HF solution. The laser intensities, irradiated on two samples, were 3 and 4 watts, respectively, and the pulse number (100 pulses), pulse width (80 ns), and irradiation duration (100 μs) and diameter of the focused laser beam (3 μm) are the same for both cases. Using light reflection measurement, we estimated that for this sample structure, 36% of the laser energy was absorbed by the top thin Si layer. Therefore, the flat and 3-D topographies shown in Figs. 2 (a) and (b) were created under irradiation of 1.08 W and 1.44 W, respectively. We suggest that these two cases represent two different mechanisms.

It is important to note first that it can be extracted from a Si-O phase diagram [39], the melting point of silicon with a composition of SiO$_\beta$ decreases from 1417 ^{0}C for pure   Si   to   a   eutectic   temperature   of   1300 ^{0}C   with   dependence   of
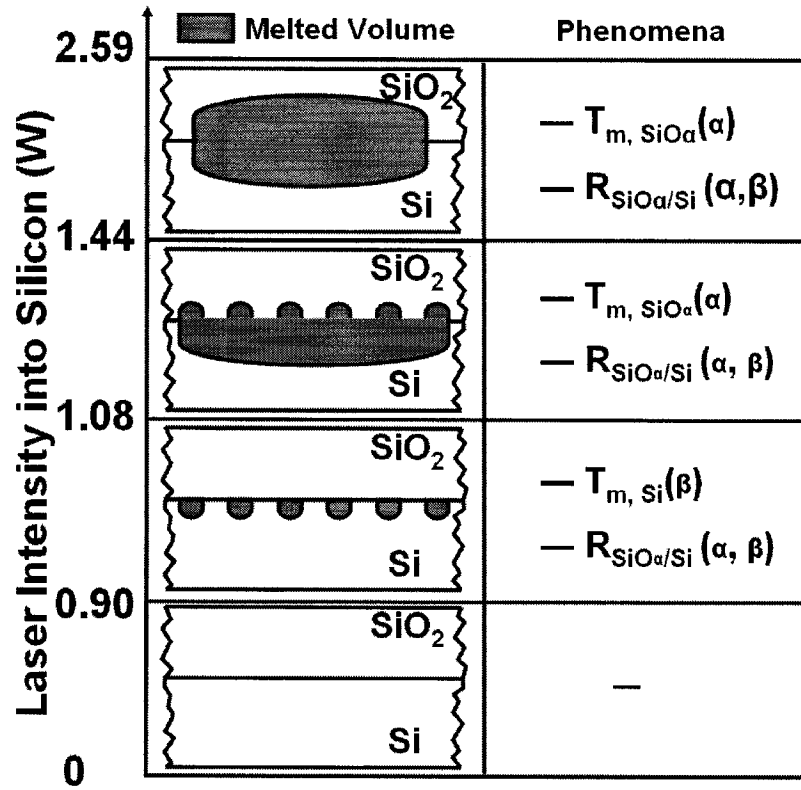
Fig. 5.1 Schematics of formation of periodic structures depending on laser intensity and positive feedback factors. See the text for the explanation on the phenomena.

$T_{m,Si}(\beta) = 914 + 503/(1+\beta)$ for $0<\beta<0.3$ and the melting point of oxide with a composition of SiO_α decreases from 1725 ^0C to 1450 ^0C with dependence of $T_{m,SiO_\alpha}(\alpha) = 3022 - 3929/(1+\alpha)$ for $1.5<\alpha<2$ when O concentration decreases. Note that the melting temperature dependence on boron was neglected because the B concentration was relatively low [39]. While all previous studies [192] [194] [218 -219] were carried on topographic formation by laser irradiated on blank material surfaces, we propose that the gateless MOSFET structure having a SiO_2 layer and B implanted

regions has a special contribution by furnishing oxygen diffusion, yielding to a local lower melting point and reflection coefficient that enhances the periodic nanostructure formation. Since no ripples were observed by AFM in Fig. 5.2 (a) for I<1.08 W, we performed plan-view TEM sample on 170 nm thick defective Si surface to investigate the microstructure generated under those laser conditions. The TEM bright-field image as shown in Fig. 5.3 (a) indicates the phenomenon of the coexisting of liquid and solid during laser irradiation process. The white gap along the y axis corresponds to the lightly n-doped region without defective contrast. The 6 white stripes along the x axis were formed because the implantation-induced defects were removed after laser annealing. Further verification was carried out using RTA (rapid thermal annealing) technique. This strain contrast due to implantation-induced defects cannot be removed even if a RTA had been performed on similar initial devices at a temperature close to Si melting point for 1 sec. Therefore, those strips with white contrast were due to periodic melting but not solid phase annealing. However, the alternate areas beside the regrown stripes remained in their solid phase during irradiation, revealed by the fact the strain contrast maintained there. This laser induced coexisting of liquid and solid did not cause ripple topography as indicated in our AFM measurement above (Fig. 5.2 (a)), which is different from those suggested by some authors for laser irradiation on blank silicon materials [187-191].
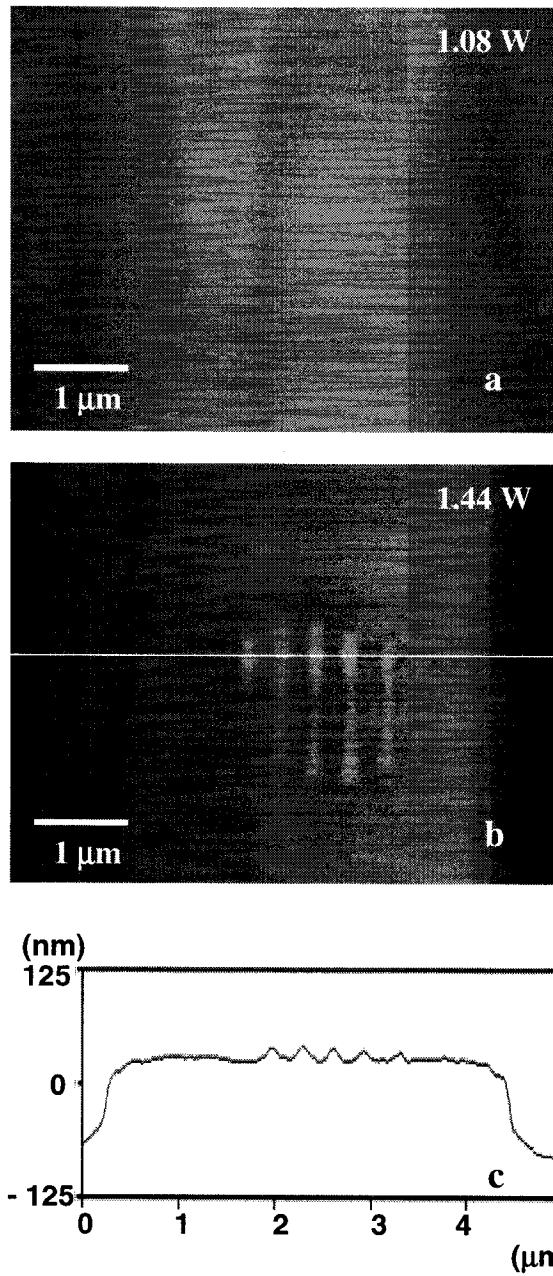
Fig. 5.2 (a) and (b) AFM images taken after etching dielectrics layers using HF solution show topographies of laser irradiated samples. Those topographies were formed at laser intensities of 1.08 W (a) and 1.44 W (b); figure (c): height delineation along the line as shown in (b).

Fig. 5.3 (c) shows a cross-sectional SEM images of a FIB-prepared sample,

along the y axis shown in Fig. 5.3 (b), taken after 2 seconds of HNA etching. The sample was produced with the same laser parameters as that shown in Fig. 5.3 (a). In Fig. 5.3 (c), because the As and diffused B concentrations at the Si surface of the gap are much lower than O concentration, the difference of etching rate mainly depends on the O profile. The 4 periodic white meniscus-like shapes indicated the regrowth regions where O atoms highly diffused from the SiO_2 into Si. The melting stripes close to the edge of the laser beam, containing less O atoms, are not revealed by SEM imaging.

The formation of aligned coexisting of liquid and solid depends mainly on the variations of the Si melting point $(T_{m, Si}(\beta))$ and reflection coefficient $(R_{SiO_\alpha\text{-}Si})$ of the liquid, related to the chemical components of dielectric and the liquid. Under laser irradiation with relatively low intensity (e.g. 1.08 W) and based on standing wave theory [188] [197-198], the Si material under the dielectric layer is periodically melted and O atoms diffuse into the molten stripes, caused by a light intensity variation. After the first few laser pulses, the melting point of the regrown strips is lowered, favoring the O atoms to diffuse from the hot dielectric into the melt faster than those into hot solid Si because the diffusion length of impurities in liquid Si is four orders of magnitude higher than that in solid Si [20]. The O impurities lower both the melting point of solid Si and the reflectivity of Si liquid. Consequently, this constitutional supercooling [215] act as positive feedback factors, leading to a periodic coexisting of liquid and solid.

In order to verify our suggestion on the formation mechanisms of the periodic coexisting of solid and liquid, a 3-D numerical simulation of the temperature field and
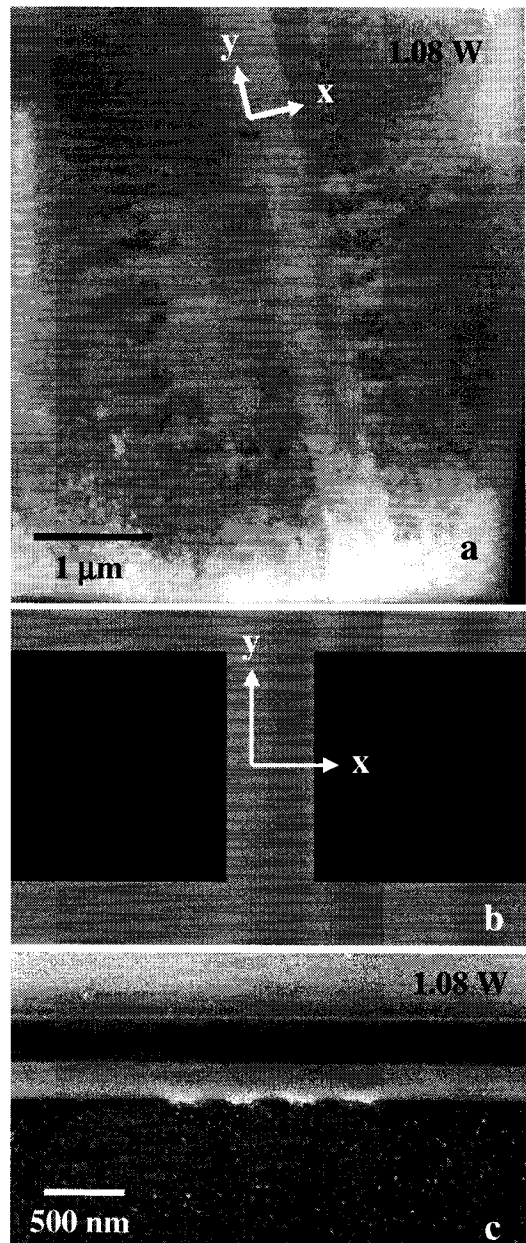
Fig. 5.3 (a) Plan-view TEM image taken from a laser irradiated sample, (b) top-view

schematics of Si substrate used in (a) process, where the areas with dark contrast are

heavily doped regions, and (c) SEM image taken from a laser irradiated sample and

FIB-prepared along y axis, The two samples were generated with laser intensity of

1.08 W.

optical reflection [18] was performed in combination with diffusion equations of oxygen

atoms. Due to the high thermal conductivity of the Si substrate at high temperature, even with a maximum intensity of about 20 % [196], we found that it was impossible to obtain any periodic nanostructures if the Si melting temperature is independent of the O concentration. However, as shown in Fig. 5.4, periodic nanostructures due to periodic melting are obtained when the melting temperature depends on the O concentration. The areas with grey contrast at Si surface represent the periodically melted regions, while the areas, in the Si substrate, with dark contrast remain in solid state. The gradient contrast in the melting strips indicates the O concentration level, which is consistent with the results observed experimentally.

As shown in Fig. 5.1, at higher laser intensity, a different periodic pattern is observed. From the TEM observation (not shown here), it is confirmed that for the case of I=1.44 W, Si material in the entire laser irradiated area was melted. After the radiation of the first consecutive laser pulses, the light reflection from the liquid of the periodically highly O diffused areas was weakened as a result of O gain in the liquid Si and O loss in the dielectric close to the interface. Therefore, the temperature in the liquid is periodically higher than the melting point of pure Si whereas the temperature in the stripes with lower O concentration is maintained at the melting point by considering the energy input from laser beam and output to the Si substrate. The melting temperature in these dielectric areas ($T_{m,SiO_\alpha}(\alpha)$), where O atoms were extremely lost, is lowered so that these thin SiO_α stripes were periodically melted. The gradients of temperature and chemical components between the two type areas with higher and lower O concentrations lead to a difference of surface tension, pushing individually each stripe,

where O concentration is higher, forming semilunar shapes (so-called periodic convection), which is similar to the case suggested by Anthony et al.[220]. By further increasing the laser intensity (I>1.44 W), the periodic formation is destroyed, as indicated in Fig. 5.1, since O atoms almost uniformly diffuse into the entire laser-melted area. In these conditions, a large liquid convection occurs in the entire molten volume involving both liquid Si and liquid dielectric.

Based on our numerical simulations, it is shown that the melting time, caused by
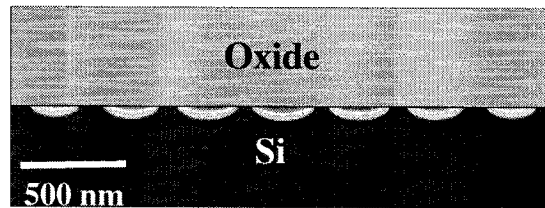
Fig. 5.4 Cross-sectional (along y-axis) image, showing the solid/liquid coexisting of the laser irradiated area, was obtained by numerical simulation.

each laser pulse, is ~ 200 ns and, since the time between two consecutive pulses is 1 μs the interval between two adjacent melting periods is about 800 ns. Even though the interval is pretty long to let the molten Si resolidify, both periodic liquid/solid coexistings and ripples, with spacing of 360 nm, can still be created by considering the decrease of Si melting point due to O diffusion.

5.5 CONCLUSIONS

We suggest that the major positive feedback factors of the formations of solid/liquid coexisting and ripple are oxygen diffusion and reflectivity variation. In our

experimental study the periodic melting is more prominent at a low intensity range while ripples are obvious at a relatively high intensity range. According to the mechanisms above, we suggest both periodic coexisting and ripples can be formed not only by many laser pulses with certain pulse interval but also by a single laser pulse with adequately high energy intensity. The final steady-state structures depend on the competition between positive feedback factors and the removal or redistribution of energy due to thermal conduction. Generalizing this fabrication of nanostructures, coexisting could occur for any material A covered by an alloy AB if it presents an eutectic temperature for AB_x, lower than the melting temperature of A point. The periodicity will be destroyed once melting time is too long due to too high power or too many laser pulses.

CHAPTER 6. ARRAY OF PERIODIC SUBMICRON CONDUCTIVE LINKS IN SI COVERED BY SIO₂ FORMED BY POLARIZED LASER IRRADIATION

(ARTICLE 3)

Yougui Liao* and Michel Meunier**

Laser Processing Laboratory, Department of Engineering Physics, Ecole Polytechnique

de Montreal, Case Postale 6079, Succursale. Centre-ville, Montréal (Québec), Canada,

H3C 3A7

6.1. ABSTRACT

Arrays of periodic submicron conductive links were fabricated in silicon, covered by SiO_2, when a polarized frequency doubled Nd:YAG pulsed laser irradiation is focused on the gap between two highly doped regions. The principle of the process is based on the fact that the laser forms a periodic melting in silicon, thus inducing a preferential dopant diffusion and creating an array of fine conductive links between the highly doped regions. Scanning capacitance microscopy (SCM) was employed to detect these submicron structures and to measure their electrical properties. It was found that between 2 to 7 submicron conductive links are observed in the focused spot size of 3 μm and their number depends only on laser intensity ranging from 3.10 W to 3.75 W, while their average width (151 – 300 nm) and depth (108 – 147 nm) strongly depends on both laser intensity and number of laser pulses. The resistances of these links are between 363 – 493 Ω and the effective average doping levels are from 1.5×10^{18} to 2.4×10^{19} cm^{-3}.

Contact authors: * liao.yougui@polymtl.ca

                    ** michel.meunier@polymtl.ca

6.2. INTRODUCTION

For many years, ripples [187-191] formed under intense laser irradiation on silicon materials have been considered to be formed at a temperature close [187] to the melting threshold. This spontaneous periodic surface structures formed after irradiation of a single or multiple uniform laser beam(s) [192] operating at optical wavelengths from the infrared to the ultraviolet region, with pulse durations ranging from continuous wave (cw) to femtosecond pulses [191-194] were frequently observed on the surface of a variety of blank materials such as dielectrics, semiconductors, and metals. The spatial orientation and distribution of the crests and valleys of the ripples are always found to be related to the wavelength (λ) [195] and the incident electric field [196] such as polarization, and the angle of the laser radiation. Emmony et al.[189] for the first time proposed that a scattering center on the surface might be responsible for the observed periodic topography. It has been suggested that theses ripples arise from standing waves produced by instability and developed as a result of interference of incident laser light with scattered electromagnetic waves from a surface disturbance [188] [197-198]. When the light intensity is sufficiently high, the melting threshold of the surface is periodically

exceeded, and thus rapid regrowth of a thin layer of molten material induces a constructive topography. The ripple periods are mostly found to follow Rayleigh's diffraction criterion [196] [198].

As recently noted by our research group [199], periodic coexisting of liquid and solid can be formed in Si material covered by SiO_2 during a polarized laser irradiation with specific laser power range and highly controlled sample surface conditions. Following the suggestion of Guosheng et al. [196] and by considering that the laser beam of wavelength λ is normal to the sample surface, the periodic spacing should be scaled and becomes to about $\Lambda = \lambda/n$, where n is the index of refraction of the surrounding media. For instance, a periodicity of about 360 nm was recently observed by TEM (transmission electron microscopy) on these SiO_2/Si systems due to oxygen diffusion into liquid silicon [199] (where $n_{SiO2} = 1.5$), when the sample was irradiated by a focused (diameter of $\sim$ 3 μm) Nd:YAG frequency doubled laser ($\lambda = 532$ nm).

Recently, a laser fine tuning (LFT) technology [4] has been developed to fabricate highly accurate resistors in silicon with a visible focused pulsed laser beam irradiating the gap between two heavily doped regions of a gateless MOSFET structure covered by SiO_2. When the laser power is as large as normally used during LFT fabrication, the dopants, such as boron atoms [200], in the heavily doped nominal source and drain, diffuse into the uniformly melted regions of the gap caused by laser irradiation and thus, form a "large" conductive link with certain resistance value depending on the temporal and spatial temperature distribution and initial dopant distribution in the source and drain regions. In this paper, we use this laser induced

periodic melting, in silicon covered by SiO_2, to form an array of submicron conductive links by focusing the laser in the gap between the heavily doped regions, as shown in figure 1. Now, in a particular laser power range, we will show that periodic melting will lead to a periodic dopant distribution and the formation of an array of submicron conductive links joining the two heavily doped regions. These structures were detected and analyzed by SCM (scanning capacitance microscopy) technique, which has been developed as a reliable analysis tool for two-dimensional (2D) dopant evaluation during the scaling of microelectronic devices [157]. The electrical behaviours related to dopant and oxygen distribution is also characterized by analyzing the dC/dV~V dependence.

6.3. EXPERIMENTAL DETAILS

The polarized laser induced periodic melting processes were carried out with a frequency doubled Nd:YAG laser (λ=532 nm) at a pulse width of 80 ns irradiating the samples during 100 μs with 30 to 100 pulses. The incident laser power, focused on the surface of the chips, was maintained at either 3.75 W or 3.10 W and its polarization is oriented perpendicularly to the p^+-n-p^+ structure as shown in Fig. 6.1. According to light reflection measurements during laser irradiation on our samples, only about 29 % of the incident laser intensity was absorbed by the thin Si layer close to the interface between the dielectrics and the Si substrate. Therefore, the intensities absorbed by Si materials were about 1.08 W and 0.9 W, respectively, for the two laser energies above.

The initial gateless MOSFET devices were fabricated by a conventional CMOS

process and consisted of two heavily doped p-type regions (boron concentration at ~

5×10^{19} atoms/cm^3) having a doped depth of 170 nm and separated by a lightly As doped

gap (concentration at ~ 10^{15} atoms/cm^3) with a distance of 600 nm. In order to remove
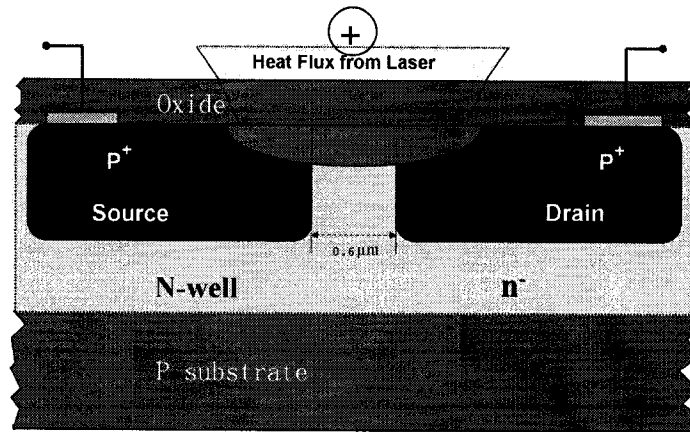
Fig. 6.1 Schematics showing the principle of laser fine tuning technology with gateless MOSFET structure. Upon silicon melting induced by laser irradiation, dopants diffuse from the source and drain, thus creating of a conductive link. The polarization orientation is also shown.

the very thick dielectric multilayers with thickness of ~8 μm, including SiO_xN_y, Si_3N_4

and SiO_2, covering the interesting laser irradiated area, the samples were first of all

dipped into 49% HF solution for 10 min under a standard clean room condition at a

temperature of 21 ^{0}C. This etching condition was chosen to rapidly remove most but not

all dielectrics to prevent affecting the silicon surface by the aggressive solution. To

complete the removal of the remaining dielectrics, the samples were cleaned with

deionized (DI) water and, then, dipped immediately into 1% HF solution for 6 min.

Before SCM measurements, the samples remain in a clean air condition for more than 10

days in order to grow a thin native oxide layer of ~1-2 nm [201] covering the samples'

surface. It should be pointed out that the thin oxide layer is important as it forms a MOS

structure and enhances the SCM signals [202].

Measurements were carried out, in ambient conditions, by a SCM system

(Digital Instruments, Dimension 3100 Model), using a standard AFM (scanning atomic

force microscope) with a metallized probe. The metallic probe tip, scanning on

semiconductor samples in contact mode, forms a MOS structure together with the thin

oxide layer as shown in Fig. 6.2. The DC bias voltage (V_{DC}) is applied to the sample and

the tip is grounded. All SCM measurements were performed with a 90 kHz AC

modulation voltage. In dC/dV~V measurements, the V_{DC} was swept between -12 V and

+12 V when the probe was fixed at one position. When a negative DC offset is applied

to the sample, there are three capacitors as shown in Fig. 6.2 (a), including a capacitance

(C_0) formed with the oxide layer, a capacitance (C_{d1}) formed due to depletion at the Si

near surface, and a capacitance (C_{sub}) formed due to the depletion in the pn junction

between the n-well and p-substrate. The SCM imaging principle is based on the fact that

the tip-sample capacitance decreases due to the depletion layer generated in the SCM

structure [154]. When a negative V_{DC} is applied, the overall capacitance (C_T) is formed

by three capacitances in series and then the overall ΔC_T can be calculated as

$$\frac{\Delta C_T}{C_T^2} = \frac{\Delta C_{d1}}{C_{d1}^2} + \frac{\Delta C_{sub}}{C_{sub}^2} + \frac{\Delta C_0}{C_0^2} \qquad (1)$$

Since C_0 is relatively small and constant, it does not contribute to the measurements.

Now since the capacitance area A_C for C_{sub} of 100 μm^2 is approximately 10^6 times larger

than the one for C_{d1} and since the effective dopant concentration N_B given by
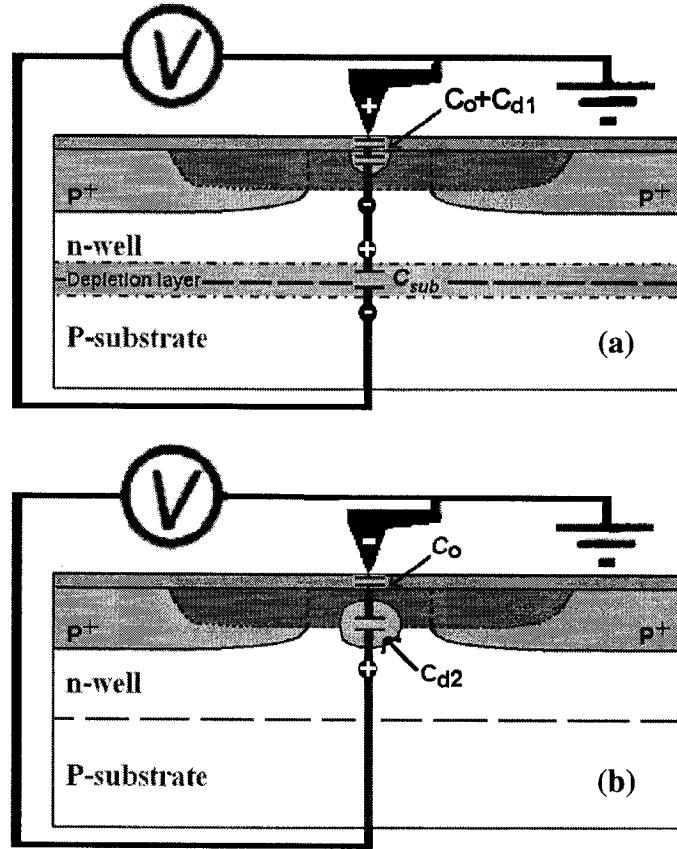
Fig. 6.2 Schematics of the SCM measurements: (a) when a negative DC bias voltage is applied on the sample, there are three capacitors, including C_O, C_{d1} and C_{sub} in series, reflecting dopant distribution of the upper part of the p-type Si; (b) when a positive DC bias voltage is applied on the sample, there are two capacitors, including C_O and C_{d2} in series, reflecting the dopant distribution of the lower part of the p-type Si.

$N_B^{-1} = N_A^{-1} + N_D^{-1}$ is $N_{B,sub} \approx 10^4 N_{B,d1}$, one can estimate that $C_{d1} \approx 10^{-4} C_{sub}$ for typical

DC and AC applied voltages by using $C \propto A_C \sqrt{N_B}$ for an abrupt pn junction [41].

Therefore, the measured SCM signal, as a result of the variation of the overall

capacitance (ΔC_T) at constant voltage mode of SCM measurement is $\Delta C_T \cong \Delta C_{d1}$ and reflects the dopant distribution in the *upper* part of the p-doped layer. On the other hand, when a positive DC bias voltage is applied on the sample as shown in Fig. 6.2 (b), since there are only two capacitors, including C_0 and C_{d2} in series, $\Delta C_T \cong \Delta C_{d2}$ and the measurement reflects the dopant distribution in the *lower* layer of the p-type Si in the n-well.

AC bias voltage was set to the maximum value of the SCM system (10 V) to ensure to have sufficient potential drop [203] on C_{d1} and C_{d2} for negative and positive V_{DC}, respectively. We also verified that this high voltage did not cause degradation of the SCM signal. SCM imaging has been observed during AFM scanning along the sample surface. The same probe tip and identical instrument settings were used except that DC bias voltages were set at -5 V and +5 V. Moreover, it was confirmed that those measurements were performed before any significant probe wear occurred by comparing the experimental results on uniformly step-doped epitaxial Si wafer before and after the measurement of the devices.

6.4. RESULTS AND DISCUSSION

One major point of the SCM detection on our devices is that the obtained SCM contrast of the gaps left after the laser irradiation is different from that obtained in the boron doped links of the laser irradiated area. For the gap without laser melting, for example, when a negative V_{DC} is applied on the sample (see Fig. 6.2 (a)), carriers

(electrons) accumulate at the upper Si layer close to the interface between the dielectric and the Si, and then the large capacitance of the pn junction, formed by the p-type substrate and n-type well, has only very small variations, yielding to a very low SCM contrast. However, when measuring the laser tuned area, a higher SCM contrast appears due to a larger capacitance variation from the additional micro-capacitor of C_{d1}. Those two different contrasts give the chance to measure the dimension of the submicron conductive links. It should be pointed out, as mentioned previously by other researchers [202], that the effect of carrier movement from a region with one dopant type into an adjacent region with a different dopant type will yield to a detectable pn junction movement. Therefore, the measured widths of the submicron conductive links and gap between the two heavily doped regions would be widened ($|V_{DC}| > 5$ V) or narrowered ($|V_{DC}| < 5$ V). In order to avoid those artifacts, the gap width of 600 nm was first measured independently by chemically selective etching in combination with TEM (transmission electron microscopy) technique [200]. Then, a wide range of V_{DC} were tested and finally the V_{DC} values of $- 5$ V and $+ 5$ V were adopted for 2D SCM imaging on our devices because it can reproduce the measured gap of 600 nm.

Due to the importance of topography on SCM measurements, the surface roughness of the microdevices was measured by AFM at the same time that SCM imaging was performed. All the surface morphology of the reoxidized devices, e.g. as shown in Fig. 6.3 (a), is uniform with a root mean square (RMS) roughness of less than ~ 0.5 nm, indicating that no deformation was caused by laser irradiation. Therefore, the submicron conductive links cannot be detected by AFM and this very good flatness is

ideal for reliable SCM measurements. Fig. 6.3 (b) shows a SCM image, obtained from a
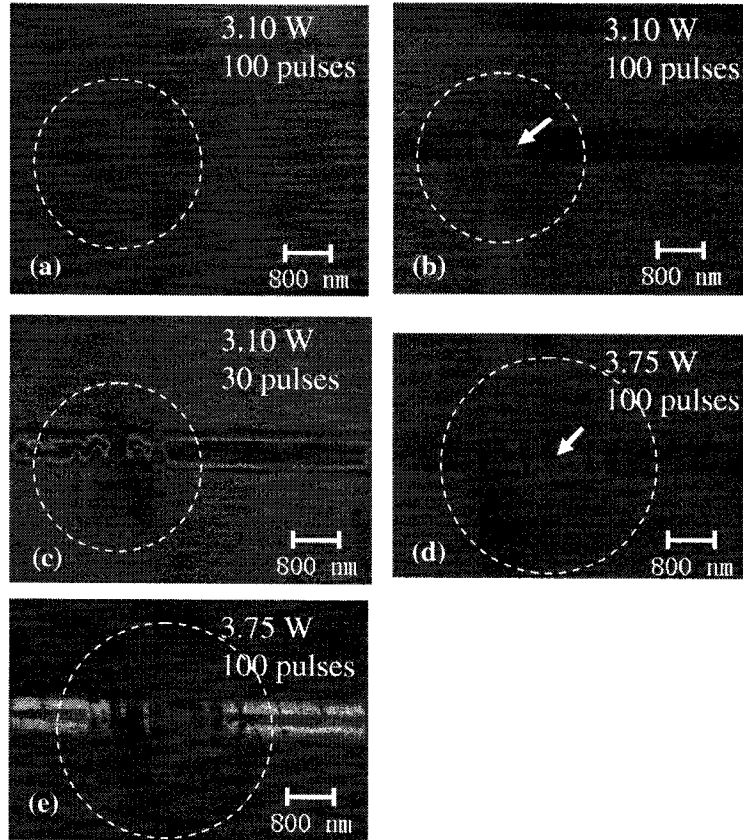
Fig. 6.3 (a) AFM image was taken from a device irradiated with laser power of 3.10 W and 100 pulses, (b) SCM images were taken with DC bias voltages of -5 V from the same device as in (a), (c) SCM images taken, by applying DC bias voltages of -5 V, from a device irradiated by a laser power of 3.10 W and 30 pulses, (d) and (e) are SCM images obtained from a device irradiated by a laser power of 3.75 W and 100 pulses by applying DC bias voltages of -5 V and +5 V, respectively. The dashed circles represent the melted ranges.

device produced by laser irradiation with power of 3.10 W and 100 pulses, taken with V_{DC} of -5 V. An array of three submicron conductive links is revealed. The center one of the three has lower contrast, probably indicating that the dopant concentration in the

local upper regrown region, close to the interface between dielectric and Si, is higher than the other ones which have probably the same level of dopant concentration. On a side, uncompleted link is probably caused by a misalignment of the laser beam yielding to a shorter diffusion time of the dopants [18] [222]. Fig. 6.3 (c) shows an SCM image taken from a device irradiated by 30 pulses at a power of 3.10 W. There are two completed links formed with a distance of about 700 nm apart. Figs. 6.3 (d) and (e) show an array of 6 submicron conductive links, fabricated by irradiating the sample with 100 pulses of laser power of 3.75 W. Both images indicate that the central links are slightly wider than those far from the center. In addition, there is one uncompleted diffused stripe on the left and right side, respectively, of the conductive array. The reason of this phenomenon is probably that the melting of the Si materials in these areas with sub-maxima of interfering light is not uniform; causing a non-uniform diffusion. For all the micro-devices fabricated by polarized laser irradiation with intensity of either 3.1 or 3.75 W, the separation (Λ) of submicron resistive links, including uncompleted links, is about $\Lambda=360$ nm. This is reasonable if we consider $\Lambda=\lambda/n$ with values of laser wavelength (λ) of 532 nm and oxide refractive index (n) of 1.48 [199].

The SCM images, taken under V_{DC} of -5 and + 5 V, have similar patterns of dopant distribution for all laser diffused devices. Fig. 6.4 shows the average width of conductive links, extracted from SCM images, in the micro-devices fabricated with laser power of 3.10 and 3.75 W and for 30, 50 and 100 pulses. Note that all average widths are lower than $\Lambda=360$ nm corresponding to a uniform melted pool and to the disappearance of the array of submicron links. Error bars were deduced from

measurements on many devices (up to 12 devices for $V_{DC} = -5$ V), each of them having

from 2 to even 7 submicron links. The variation of the number of conductive links in

different devices fabricated in the same conditions of laser intensity and pulse number

maybe due to the instability of laser interaction with materials which depends on specific

delectric/Si interface and the exact characteristics of multilayer materials. The depths of

the melted region as determined by performing dopant selective etching in combination

with TEM imaging [200] are also given for reference. As the laser power increases, both
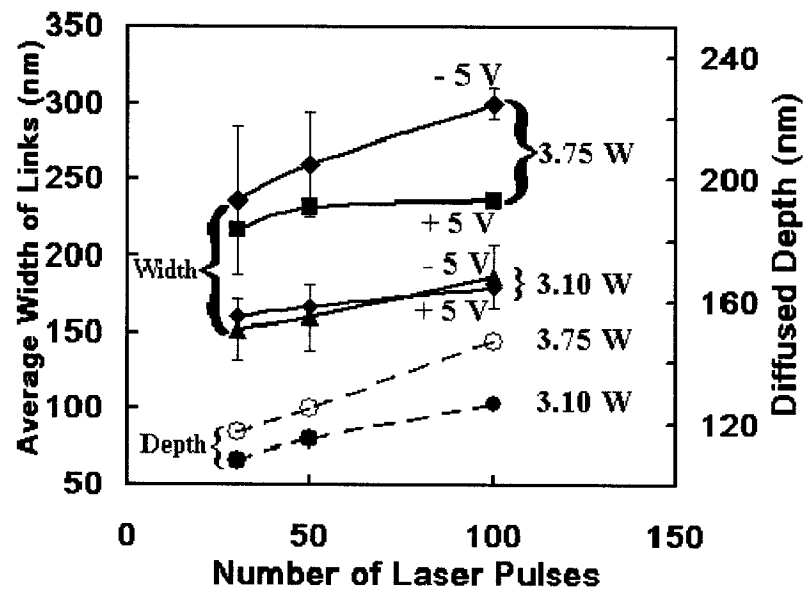
Fig. 6.4 Average width of the upper side (DC = - 5 V) and
lower side (DC = + 5 V) of the submicron conductive links
formed by laser irradiation with light intensities of 3.10 W
and 3.75 W together with the maximum melting depth for
both cases.

the depth and the width increase as the melting time and consequently the dopant

diffusion time are longer due to the larger energy absorbed by the materials [18]. The

increase in the number of laser pulses has a similar effect as from pulse to pulse the accumulated dopant diffusion time increases. Fig. 6.4 also indicates that the upper (V_{DC} = -5 V) and lower (V_{DC} = + 5 V) widths of the links are almost the same for the devices fabricated with lower laser power (3.10 W) but are clearly different for higher value (3.75 W) and as the number of laser pulses increases. As it will be discussed below, oxygen which is an n-type dopant in silicon, is probably diffusing from the SiO_2 toward the silicon melted poll as the power increases, thus affecting the effective dopant distribution and SCM measurements.

In order to characterize the electrical properties, measurements of dC/dV vs sample bias V_{DC} were carried out in the center of submicron conductive links and results are shown in Figs. 6.5 (a) and (b) for microndevices fabricated at laser powers of 3.10 W and 3.75 W respectively. For comparison, the dC/dV~V_{DC} curves taken at the heavily doped regions far from the laser irradiated area are also shown. For all those measurements, when the sample is negatively biased, SCM signals in the laser irradiated conductive links are lower than those in the initially heavily doped regions without laser irradiation. Those results indicate that the net carrier concentration in the upper parts of the submicron regrown Si links was higher than that in the initially heavily doped regions. This phenomenon can probably be explained by the fact that the concentration of the net electrical activated dopants that diffused into the upper regions of the submicron conductive links, is higher than that in the heavily doped regions without laser melting, probably due to the higher electrical activation under laser irradiation [204] or boron segregation towards the dielectric multilayers during resolidification. This is in

good agreement with the observed higher dopant concentrations, revealed by the lower contrast, in the regrown areas in both the formed conductive links and the laser-irradiated parts of heavily doped regions as shown in the SCM images of Figs. 3 (b), (c) and (d), measured at a fixed V_{DC} of $-$ 5 V. Moreover, it is very interesting to note that the SCM images (not shown here), obtained from microdevices fabricated by laser irradiation under power of 3.10 W and 30 pulses with V_{DC} bias of $+$ 5 V, had the same contrast difference, between conductive links and non-irradiated heavily doped regions, as that shown in Fig. 6.3 (c). The origin causing these results might be related to the possible fact that the dopant concentration in the regrown conductive links are almost uniform, yielding to similar ΔC with the same AC bias modulation as measured with V_{DC} of - 5 V and $+$ 5 V. Furthermore, for both cases with laser intensities of 3.75 W and 3.10 W, the SCM signals with negative V_{DC} reveal that the net carrier concentrations in the depth range of the conductive links close to the interface between the dielectric and the Si substrate decrease during the irradiation of additional 70 pulses following the irradiation of the first 30 pulses. The reason of this phenomenon might be related to the presence of oxygen in the upper part of the conductive links. Indeed, as either the number of pulses and/or laser power increase, more oxygen atoms diffuse from the SiO_2 into the melted Si, thus compensating the effect of the acceptors, because O is know to be a n-type dopant [68].

On the other hand, as shown in Fig. 6.5, the shift of SCM signals in the positive V_{DC} range, directed by the arrows from non-irradiated heavily doped region to conductive links, suggests that the net p-type carrier concentration close to the bottom of
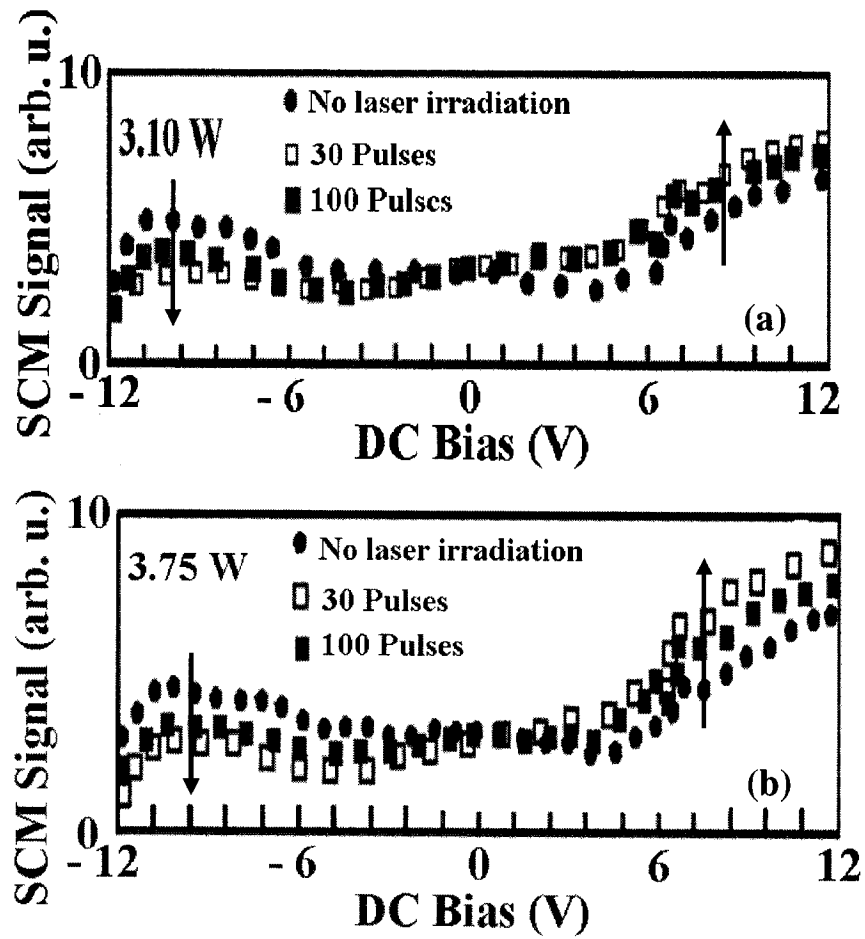
Fig. 6.5 dC/dV vs sample bias V_{DC}, taken in the center of submicron resistive links in the microndevices fabricated with laser power of (a) 3.10 W and (b) 3.75 W. Results taken in the heavily doped region far from the laser irradiated area (No laser irradiation) are also shown in figures.

the melting pool increases and becomes "box-like" distribution with the increase of pulse number from 30 pulses to 100 pulses. In addition, the net carrier concentration in these depth regions of the conductive links with laser irradiation of 3.75 W is less than that with 3.10 W probably because the melted pool is deeper yielding to a lower dopant concentration at the bottom of the link where the SCM probes at $V_{DC} = +5$ V.

Fig. 6.6 (a) shows resistance R as obtained by four-point probe measurement as a function of the number of pulses for 3.10 and 3.75 W of laser power. The resistances are between 363 and 493 Ω and decrease when more pulses and/or higher power are applied, mainly due to the increase in both the molten width and depth as shown in figure 4. Assuming an uniformly dopant distribution, an average resistivity can be evaluated using $\rho = RA/l$ where A is the total area of N_L half ellipses ($A = N_L \pi wd / 8$ where N_L is the number of links and w and d are the width and the depth, respectively, given in figure 4) and l the length taking as the initial gap width of 600 nm. Figure 6(b) shows that, on average, ρ are 2.8±0.3 and 10.6±0.6 mΩ•cm for links fabricated at 3.1 and 3.75W respectively. On the same figure, the effective dopant concentration is also given by using the experimental relationship between the resistivity and the dopant level [41]. The range of effective dopant concentration between 1.5×10^{18} and 2.4×10^{19} cm^{-3} is quite reasonable as it must be slightly lower on the average, after diffusion, than the doping level of 5×10^{19} acceptors/cm^3 of the heavily doped regions. The difference between the links made at 3.10W and 3.75W and the slight increase in ρ as the number of pulses increases are again probably related to the presence of oxygen contaminants in the links, as proposed by SCM results above.
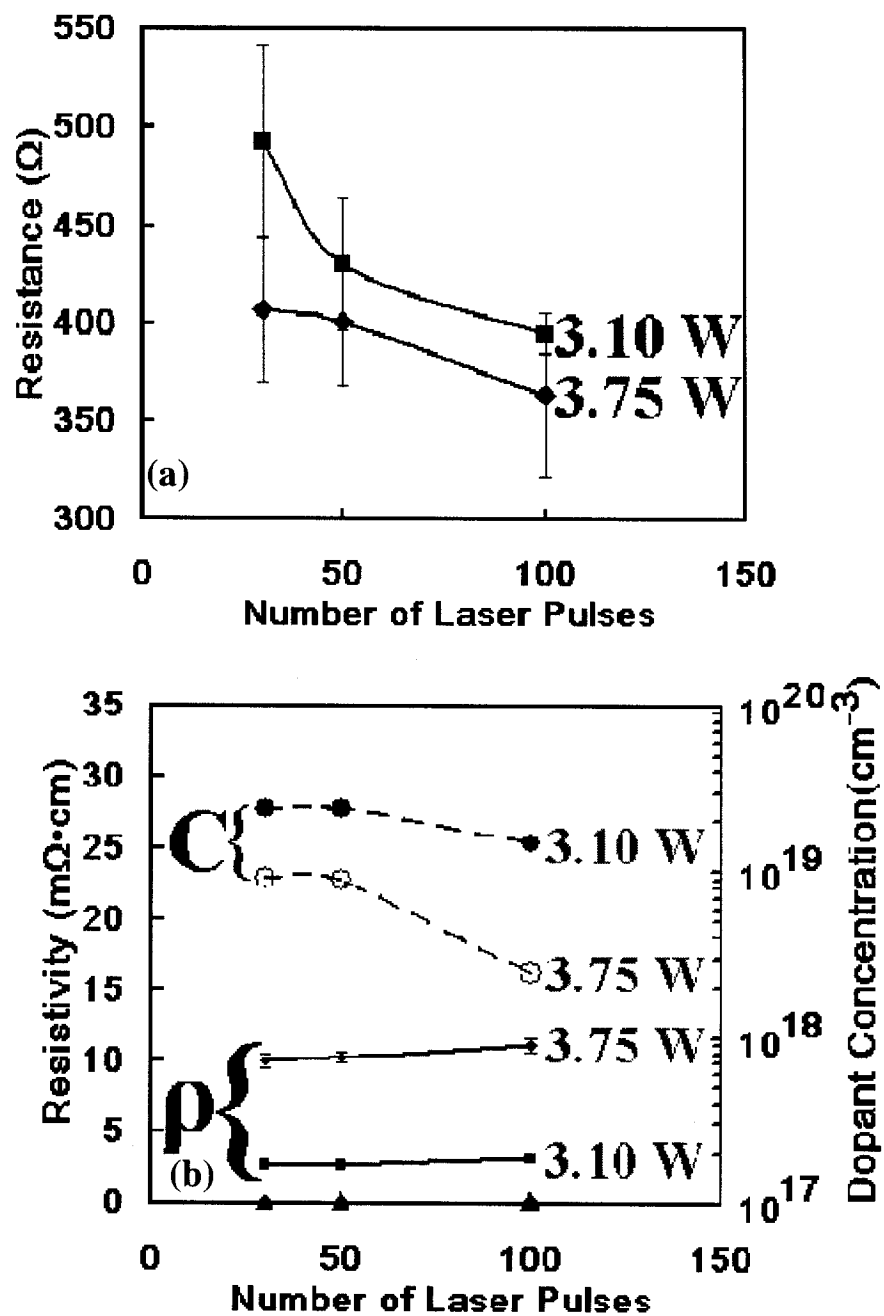
Fig. 6.6 Resistance (a), resistivity and dopant dependence (b) on laser power and pulses.

6.5. SUMMARY

Array of submicron conductive links was formed in the silicon covered by SiO_2 by laser induced periodic melting. In this process, at specific polarized laser conditions, the dopants present in the two highly doped regions diffuse into the periodic melt thus forming an array of conductive links joining the two doped regions. As characterized by four-point probe and SCM measurements, the resistors with submicron conductive links have resistances ranging 363 – 493 Ω and their values are related to width and depth of the links as well as to the dopant and oxygen concentrations. All these characteristics depend on laser intensity and pulse number. The number of submicron conductive links depends mainly on the laser intensity, while the width (151 – 300 nm) and depth (108 – 147 nm) of the links depend not only on the laser intensity but also on the pulse number. The quality of the dielectric/Si interface and of the multilayer materials should be well controlled in order to produce arrays with specific resistance value, number, width and depth of conductive links.

ACKNOWLEDGEMENTS

CHAPTER 7 STRUCTURAL CHARACTERIZATION OF LASER DIFFUSED RESISTORS

7.1. INTRODUCTION

Even if the property of the LDRs is mainly controlled by dopant distribution [221-223], it also depends partially on microstructure including defects. The work presented in this chapter focuses on such a comprehensive investigation of microstructure of LDRs created under various laser conditions in order to completely understand the physical nature of the fabrication process and, thus, improve the accuracy and long-term stability of these devices. In previous studies[34 – 35][65][224], it was pointed out that, under certain laser conditions, laser-induced melting generated microdefects and deep trapping centres, which caused a deterioration of the electrical properties of the semiconductor devices. Therefore, the reduction of the grown-in defects is a fundamental requirement to obtain the necessary device quality. Those defects could agglomerate to form (i) point defects[65][224] such as vacancies, extra-interstitials and self-interstitials, (ii) extended dislocations[34 – 35], (iii) diffused impurities, e.g. oxygen, and (iv) impurities transferred due to convection [225 – 226]. In this chapter, we suggest the formation mechanisms of various defects observed in LDRs and discuss the effect of convection occurring during the laser induced heating of silicon.

7.2. FABRICATION OF LDRS

Microstructures presented in this chapter and listed in Table 7.1 were taken from LDRs fabricated with various parameters approaching those potentially used conditions in industry. The laser power was fixed at 4 W, which induce the temperatures of the heated Si materials in the temperature window between the melting points of the Si materials and the SiO_2. The numbers of the laser pulses used were from 10 to 150 pulses in order to reveal the effect of accumulations to number of identical laser pulses on the microstructures. The laser pulse duration of 80 ns have been selected in order to have sufficient melting depth to create the resistive links, while minimizing the liquid convection during laser irradiation. Laser beam spot size of 4 μm, the same as the width of heavily doped regions, is used to facilitate FIB-TEM sample preparation and reduce the effects of the possible laser beam dis-alignment. In order to study the effect of the point defects, laser-induced thermal annealing, induced by setting the light intensity at half of the melting threshold of silicon materials, is also used for certain LDRs. Finally, it should be pointed out that the processing period of 100 μs is the period from the beginning of the first laser pulse to the end of the last laser pulse.

Table 7.1. laser processing conditions used in this chapter.

Fabrication Condition	Power (watts)	Number of laser pulses	Pulse duration (ns)	Processing period (μs)	Diameter (μm)	Laser induced thermal annealing
FC #1	4	10	80	100	4	Yes
FC #2	4	50	80	100	4	No
FC #3	4	100	80	100	4	No
FC #4	4	150	80	100	4	No
FC #5	4	100	80	100	4	Yes

7.3. CHARACTERIZATION METHODS

It is well-know that TEM (transmission electron microscopy) and AFM (atomic force microscopy), both having high spatial resolution, can be used for microstructural and topographical analysis. Dislocations and morphology can be obtained using bright field TEM, weak beam imaging [98] [227] and diffraction. In this study, TEM sample preparations were performed using the FIB (focused ion beam) technique, by taking advantage of highly precise localization and highly accurate control of TEM sample thickness. In order to have flat and clean TEM sample surfaces, a Ga ion beam with low current in an available HITACHI FB-2000A system was employed in the final milling step to polish the TEM slices. The TEM samples were obtained along two perpendicular directions, as shown in Fig. 7.1. The TEM samples along the x axis, with thicknesses less than 600 nm, were used for the concentration estimation of point defects. However,
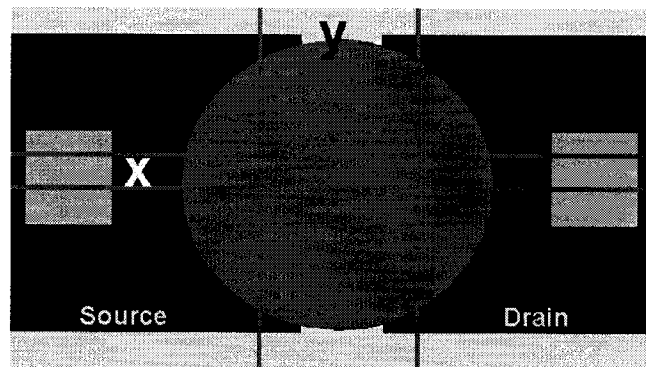
Fig. 7.1 Top-view of the laser-diffused resistors showing that TEM samples were obtained along the two directions, which are along x axis and y axis, respectively.

the TEM samples along the y axis were prepared thicker (about 1.2 μm), than those

along the x axis, for qualitative defect evaluation of the entire LDR including all the dielectric multilayers (about 7 μm of thickness).

Concerning the evaluation of point defects, neither vacancies nor interstitial concentrations in silicon can be directly measured [228]. Moreover, the direct determination of the oxygen diffusion in silicon is impossible even using electron energy-loss spectroscopy (EELS), because the number of oxygen atoms in the silicon materials is small when compared to the native oxide layers (1.5 to 2.0 nm thick) on both surfaces of the TEM samples [98]. In our study, we used chemical etching to evaluate the point defects and oxygen diffusion caused by the laser irradiation on the microdevices. A mixture of hydrofluoric acid (HF, 49%), nitric acid (HNO_3, 70%) and acetic acid (CH_3COOH, 96%), the so-called HNA solution, with a ratio of 1:3:8 was employed to evaluate defects due to their sensitivity to point defects in Si crystals [85]. However, it must be pointed out that this solution and hydrofluoric acid (HF, 49%) are also sensitive to different dopant levels in Si materials [128] [131]. That is, the higher the concentration of point defects and/or the dopant concentration, the higher the chemical etching rate. Moreover, HF solution was used to etch the dielectric multilayers, followed by deionized water cleaning. In our study, it was also found that the etching rate of Si materials with high vacancy concentrations was much lower than that with high dopant concentration, when the samples were dipped in HF (49%) solution.

7.4. POINT DEFECT FORMATION IN LDRS

The bright-field cross-sectional TEM image in Fig. 7.2 shows a LDR fabricated with the initial structure of a gateless field effect transistor with a nominal source to drain distance of 0.6μm. This device had a resistance value of 500Ω and was produced with identical 100 laser pulses, 3.0 W of power, and 80 ns of a pulse width. The rounded shape of the oxide layer at the center of the device is due to a field oxide that was grown in the absence of the gate between the two highly doped regions. Based on TEM imaging methods, including bright-field as well as dark-field and weak-beam imaging in combination with chemical etching, no detectable defects, including no impurity inter-diffusion between the dielectric multilayers and the regrown Si and no dislocations in the regrown Si, were found. The reason might be the temperatures, during laser irradiation, is exactly in the temperature window between the melting points of silicon and silicon dioxide. On the other hand, as expected, using TEM technique in combination with dopant selective etching (DSE), dopant concentration profiling revealed that a resistive link with a medium dopant concentration between the regions of the source and the drain is formed. Note that in this chapter, all the results were carried out on flat LDRs (without the field oxide) because of its potential application in next generation of microelectronics industry.
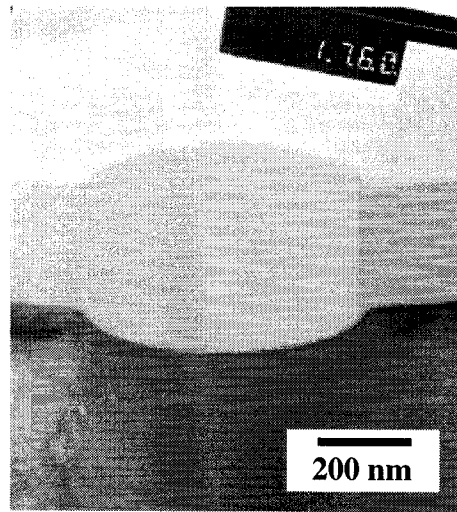
Fig. 7.2. TEM image shows the microstructures of a LDR fabricated with the initial structure of a gateless field effect transistor with 100 laser pulses, 3.0 W of power, and 80 ns of a pulse width.

7.4.1. POINT DEFECT FORMATION IN SI CLOSE TO THE DIELECTRIC-SILICON INTERFACE

Fig. 7.3 (a) shows a bright field TEM image taken along the x axis of a TEM sample prepared under FC #1. The Si side, within a depth of 15 nm underneath the interface between the dielectrics and the Si, has a higher contrast than the bulk Si. In order to investigate the origin of this contrast, this TEM sample and a device, after laser tunning with the same parameters as Fig. 7.3 (a), were etched in various chemical solutions. Fig. 7.3 (b) shows a bright field TEM image taken after etching the TEM sample of Fig. 7.3 (a) using HF (49%), indicating that the 20 nm surface layer of Si material is etched at a lower etching rate than the heavily doped source/drain areas. The most heavily boron-doped Si in the link and the source/drain regions, together with the

dielectrics multilayers, are almost completely etched away. Fig. 7.3 (c) shows an AFM top-view image taken from a device, produced under FC #1, after HNA chemical etching subsequent to HF solution etching.

Fig. 7.3 (c) implies that either the dopant concentration at the Si surface or the concentration of point defects or both are very high because the local HNA etching rate at the Si surface at the laser irradiated region is higher than those in the heavily doped regions and the rest of the resistive link, revealed by the blacker contrast. However, as shown in Fig. 7.3 (b), the black contract at the Si surface indicates that the dopant concentration in this area is relatively low; we can conclude that the concentration of point defects at that area is relatively high as compared to the rest of the device. We can explain this phenomenon from the point of view of vacancy generation under laser irradiation. During laser-induced thermal annealing (without melting the Si) with many laser pulses, the Si surface, beneath the dielectric, locally experiences a temperature, close to Si melting point, during a very long time (a total of about 100 μs). Some silicon atoms and almost all the diffused boron atoms, which are smaller than Si atoms, are ejected from the Si surface area into the bulk silicon or the dielectric, thus creating a large number of vacancies. This is in good agreements with the conclusions of other researchers [229], who pointed out that even for perfect semiconductors, after the accumulation of consequent heating due to successive local irradiation pulses without melting, point defects at the interface can be generated. This process creates isolated vacancies, similar to the process using electron irradiation [71]. Furthermore, it should also be pointed out that in Fig. 7.3 (b) the blacker contrast, than the contrast in the non-
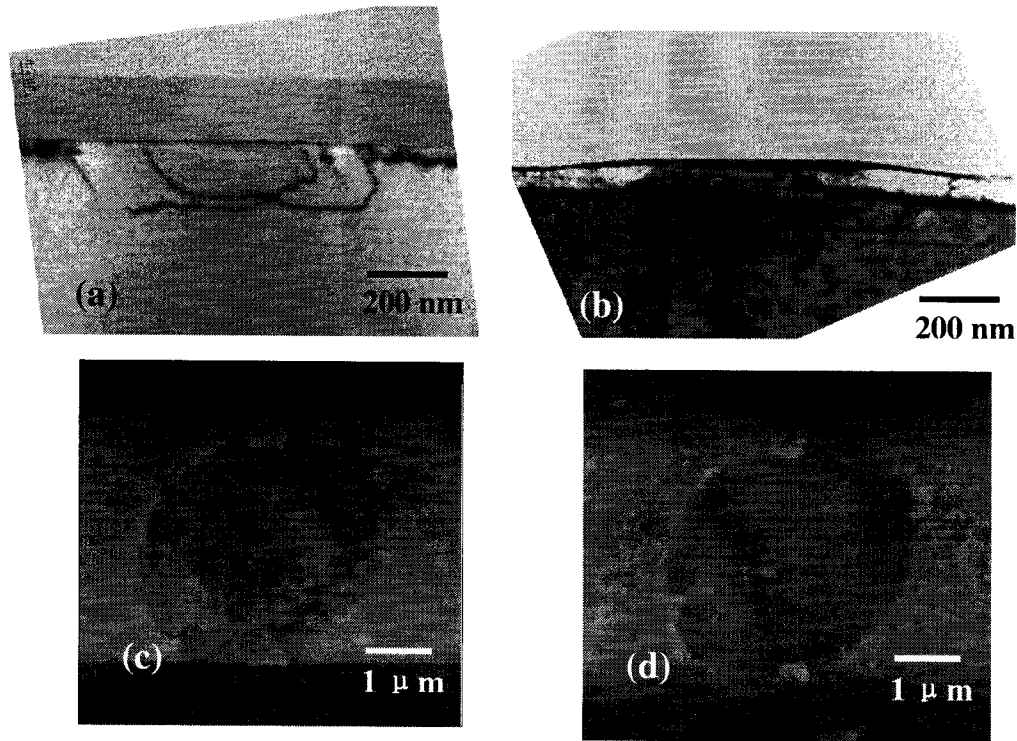
Fig. 7.3 (a) TEM image taken from a LDR produced under FC #1; (b) TEM image taken from the TEM sample in (a) after it was etched by HF (49%) solution; (c) AFM image taken from a LDR, produced with the same fabrication condition as that of (a), after HF and HNA etching successively; (d) AFM image taken from a LDR produced with the same LFT conditions but without laser induced thermal annealing process, after HF and HNA etching consequently.

melted Si, maybe is also partially due to disorder of crystalline Si atoms with various clusters.

Furthermore, Fig. 7.3 (d) shows an AFM image obtained from a LDR, produced with the same LFT conditions but just without laser induced thermal annealing process. This image, taken after HF and HNA etching processes, indicates a similar phenomenon

as the one revealed in Fig. 7.3 (a) - (c). These results suggest that these vacancies were formed within the regrown silicon located at the dielectrics/silicon interface because of its higher temperature lasting the longer time during cooling

7.4.2. POINT DEFECT FORMATION IN LASER IRRADIATED BULK SILICON

Fig. 7.4 (a) shows a TEM image of a LDR processed under FC #3. In this device, the center area has a higher contrast than the off-center areas, as shown by the arrows, respectively. This higher contrast was caused by the amorphous phase of local silicon material.

The question of the concentration of point defects remains open and cannot be answered by HRTEM (high resolution TEM). In order to estimate the concentration of point defects inside the laser irradiated area, the sample shown in Fig. 7.4 (a) was etched using an HNA solution. Fig. 7.4 (b) reveals the areas in the source and drain regions with the highest B concentration located at a depth of about 150 nm. The central area of the laser-irradiated melting pool, within a depth of 600 nm and a width of 800 nm, is completely etched away. According to the dopant evaluation (see chapter 4), the dopant concentration at a depth of 150 nm is about 10^{19} atoms/cm^3. If we assume that the etching rate is mainly dependent on the concentration of dangling bonds and weak bonds, the concentration of point defects inside the completely etched regions should be greater than 10^{19} atoms/cm^3 (> 200 ppm).

The perfection of grown Si crystal is partially determined by several factors, which are directly or indirectly related to the solidification rate. The first factor is the cooling rate. Due to the significant temperature difference between the substrate and the melting zone, the extremely high cooling rate, towards the end of the laser-induced
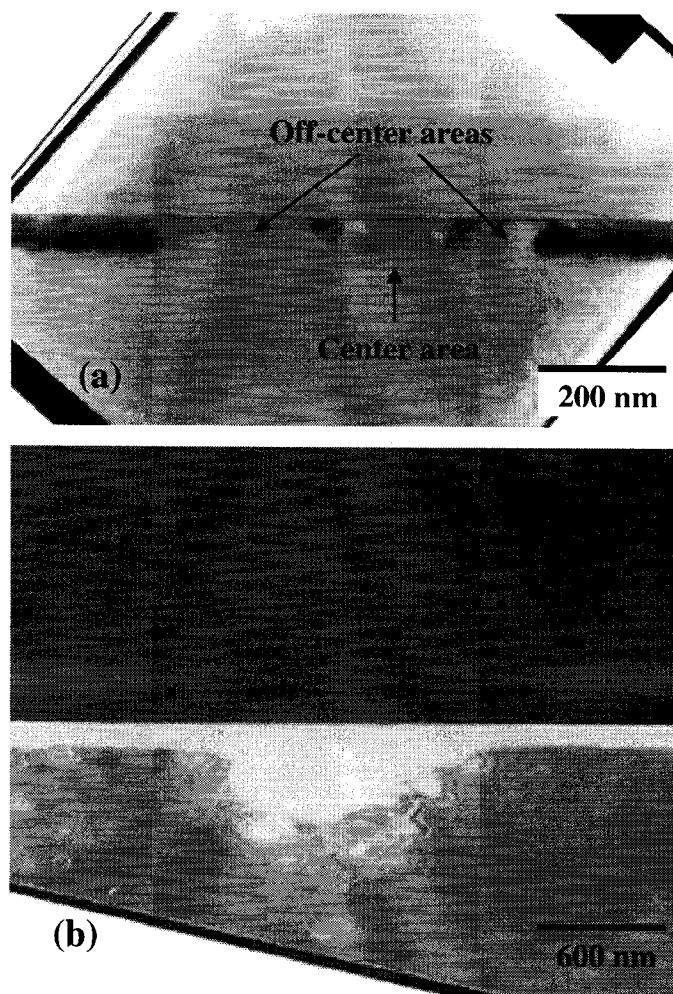
Fig. 7.4 (a) TEM image taken from a LDR processed under FC # 3. The sample was prepared along x axis. (b) TEM image taken after the sample in (a) was etched in HNA solution.

melting cycle, can result in the development of non-equilibrium solid solutions. Using a thermodynamics model, we calculated the depth dependence of the cooling rate, along the center of laser beam, during the solidification step following the laser induced melting. Fig. 7.5 (a) shows the depth dependence of the cooling rate at the center position of the laser beam. The value of the cooling rate relates to the rates of generation
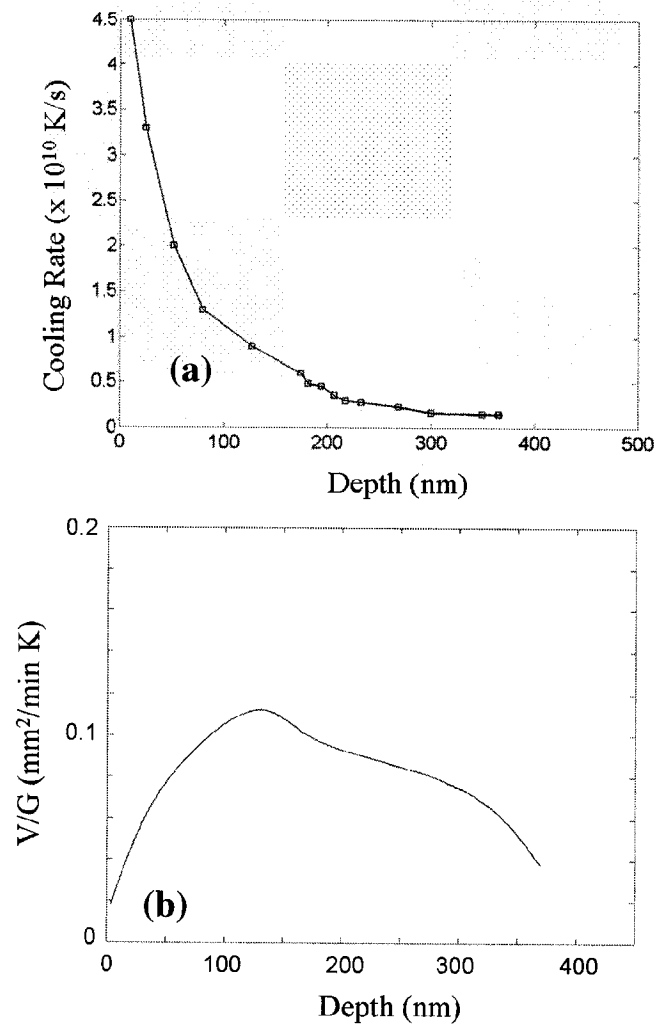
Fig. 7.5 (a) Simulation of cooling rate, at the center position of laser beam, as a function of depth, and (b) V/G value, at the same location as that of (a), as a function of depth.

and accumulation of native point defects. According to Fig. 7.5 (a), the cooling rate in silicon is higher at the dielectric/Si interface; thus, a large concentration of defects, such as vacancies and/or interstitials in the Si lattice, can be trapped in the quenched and recrystallized Si. A similar phenomenon was reported previously [54].

Fig. 7.6 (a) and (b) shows bright field TEM images taken from two microdevices, FIB-cut along y axis, produced under FCs #3 and #5, respectively, after HNA etching for 2 seconds. Both TEM samples had initial thicknesses of 1.2 μm prior to chemical etching. The etched areas for both devices have dimensions of about 2.1 μm in diameter. The device shown Fig. 7.6 (a) was produced with only laser tunning process under melting condition, while the device shown Fig. 7.6 (b) had the same process but was further annealed by laser non-melting irradiation, with a power of half the melting threshold. The etched profile shown in Fig. 7.6 (a) disagrees with the numerical simulation results, as given in Chapter 4, of which indicates that the highest dopant level is located at the center of laser-irradiated Si surface due to the longest melting time. In order to interpret this phenomenon, we must consider the etched profile from the point of view on point defects.

Silicon has metallic bonding in the liquid state but covalent bonding in the crystalline solid and amorphous solid states [231]. After laser-induced melting, quenching occurs during rapid solidification [232], inducing a large quantity of dangling bonds in the silicon. Crystalline Si has a lower etching rate than Si materials containing a high concentration of point defects. On the other hand, the presence of amorphous Si also increases the etch rate. The type of point defects in the regrown Si volume can be

determined, as indicated in the previous theoretical and empirical studies [224] [230], by

considering the second factor controlling the perfection of grown Si, which is the V/G

ratio. Here V is the crystal growth rate and G is the temperature gradient at the interface

between the solid and the liquid, during solidification. In principle, almost perfect

crystalline silicon can be obtained when the regrown materials are produced at a critical

ratio of V/G, namely $(V/G)_{critical}$, of about 0.1 $mm^2/min \cdot K$ and at a very low cooling rate,

e.g lower than 10^9 K/s, even no exact value is known up to now. Fig. 7.5 (b) shows the

V/G dependence at the center position of the laser-irradiated Si surface as a function of
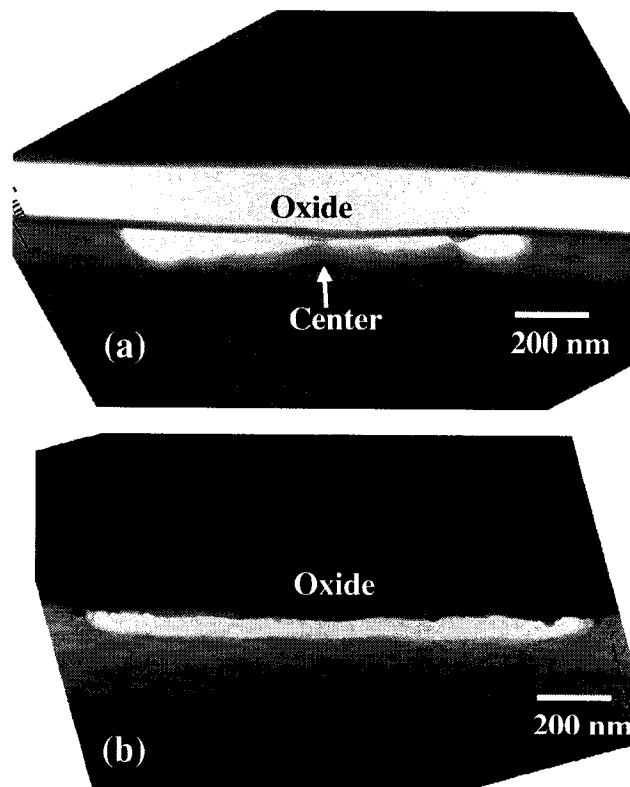
Fig. 7.6 TEM images were taken from LDRs produced under FCs #3 (a) and #5 (b) after HNA etching. The TEM samples were prepared along y axis.

depth. In the depth range of 90 to 160 nm, V/G > (V/G)$_{critical}$ and, thus, this region could

contain vacancies, enhancing the etching rate there. Fig. 7.6 (a) also shows that Si

materials at the two sides of the laser irradiated region, with lager area than at the center

location, were completely removed (indicated by the holes) during etching process. The

reason for this phenomenon might be that vacancy-type grown-in defects or voids with

very high concentration were generated in these locations, with larger area, because of

(V/G) > (V/G)$_{critical}$. For the LDRs without non-melting laser annealing, the entire region,

which contain point defects due to melting of the Si materials, are within 2.2 μm in

diameter, indicated by region I in the top-view schematics shown in Fig. 7.7. However,

the annulus indicated by region II, with a diameter from 2.2 μm to about 2.5 μm

(maximum melting diameter as revealed by dislocations in other LDRs), the V/G is
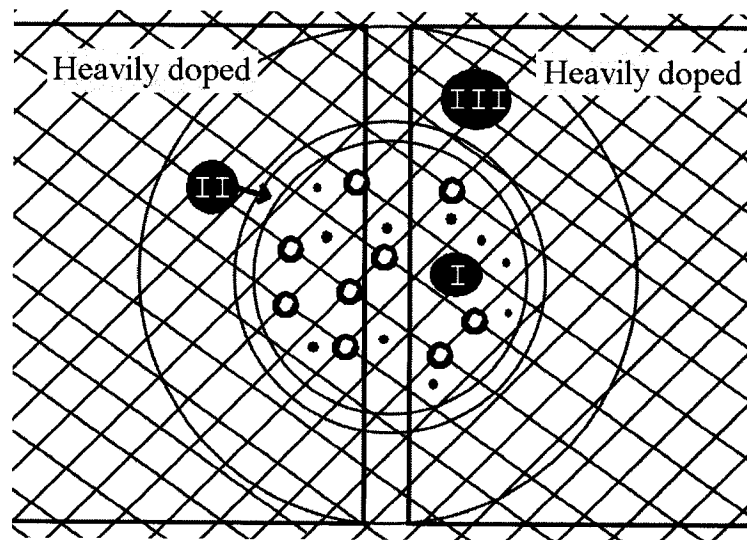
Fig. 7.7 Area I contains point defects, including vacancies and interstitials; Area II was melted but does not contain point defects; Area III was laser-irradiated but not melted.

smaller than (V/G)$_{critical}$ and, thus, the larger diffusivity of vacancies, than that of

interstitials, causes depletion of the vacancy before the crystal cool down [228]; therefore, the interstitials probably are supersaturated and could not be revealed by the HNA etching process. The later case suggested that the materials in the region close to the melting edge have almost the same etching rate as that of bulk Si. Therefore, the etched hole is smaller than the melting dimension.

Fig. 7.8 summarizes the relative distribution of point defects when LFT process is performed. As sown in Fig. 7.8 (a), for LDRs with only laser-induced melting process, point defects, as represented by open (vacancies) and closed (interstitials) circles, only appear in the laser-melted area. As discussed above, the vacancy rich regions have a high cooling rate and a V/G, higher than 0.1 $mm^2/min \cdot K$, while the interstitial rich regions have a high cooling rate and a lower V/G. On the other hand, as shown in Fig. 7.8 (b), when non-melting laser-induced thermal annealing is performed after laser-induced melting process, only the vacancies accumulate at the SiO_2/Si interface and almost perfect crystalline Si in the regrown bulk Si is produced. Moreover, it should be pointed out that the two factors of cooling rate and V/G are controlled by laser parameters and, generally, the shorter the duration of the laser-induced melting, the higher the density of point defects. Of course, any specific defect concentrations depend on the number of laser pulses, tuning duration, etc.

Furthermore, as expected, Fig. 7.6 (b) reveals that laser heating, so-called non-melting laser annealing, with substantially lower irradiation energy densities, can dissolve most of the point defects caused by the quenching recrystallization process. In this case, the etched profile becomes understandable when compared with experimental
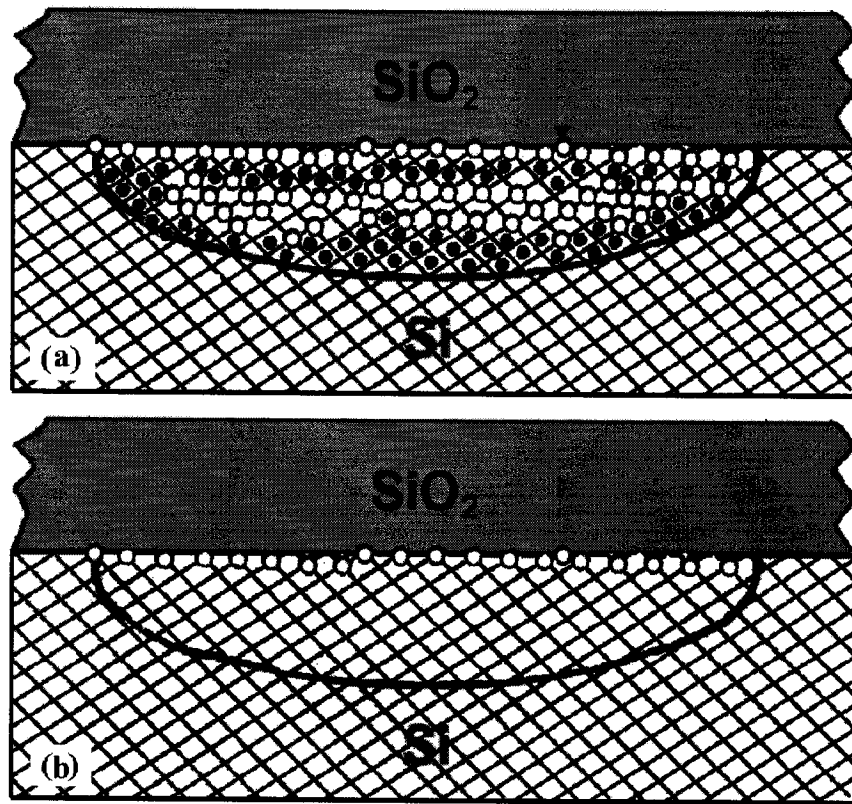
Fig. 7.8 Schematics of distribution of point defects after LFT only, namely without (a) and with (b) non-melting laser induced thermal annealing. The empty circles represent vacancies and the solid circles represent interstitials.

results and numerical simulation on dopant diffusion which are similar to dopant profile shown in Fig.4.6. The schematics shown in Fig. 7.8 (b) indicates almost perfect crystalline Si, except vacancies located at the dielectrics/Si interface, formed after LFT and laser induced thermal annealing processes, consequently.

7.5. MATERIAL INTERDIFFUSION BETWEEN LIQUID SI AND DIELECTRIC

In order to study the inter-diffusion of species between the dielectrics and the liquid Si, TEM observations were carried out in combination with chemical etching.

Figs. 7.9 (a) and (c) show TEM images taken from LDRs, produced under FC #2 (50 pulses) and #3 (100 pulses), respectively. The TEM images were obtained after HNA etching for 2 s on samples prepared by FIB along the y axis. Fig. 7.9 (d) shows the center area of Fig. 7.9 (c) at a higher magnification. Figs. 7.9 (a) and (c) present gradient of dark contrast underneath the dielectrics after HNA etching. Because the contrast depends on the etching rate, namely the lower the etching rate the darker the contrast, and oxygen atoms in silicon strongly suppress the etching process, those TEM figures suggest that oxygen atoms with a high concentration were diffused from the dielectric into the molten Si within a depth of ~50 to ~70 nm close to the interface between the dielectric and the re-solidified Si. The difference between the two devices is that the oxygen concentration from the interface to the bulk silicon gradually decreases in the device fabricated under condition #2 (50 pulses) as indicated in Fig. 7.9 (b), while the oxygen concentration within the same depth increases, from the dielectric/Si interface, in the device fabricated under FC #3 (100 pulses), as shown in Fig. 7.9 (e).

The absorbed light energy is reduced by a factor of 2 when the top Si layer becomes liquid [187]. The temperature of the silicon dioxide layer close to the interface rises rapidly because not only the optical energy absorption of the bottom dielectric thin layer increases due to the increased reflected light illumination but also the heat transfers from the liquid silicon into the oxide. Once the temperature of the bottom dielectric layer exceeds a certain chemical energy threshold, the bonds between silicon and oxygen will be broken and, then, the oxygen, as well as the silicon, will become highly mobile. Therefore, there are several factors that control oxygen atom diffusion into top layer of
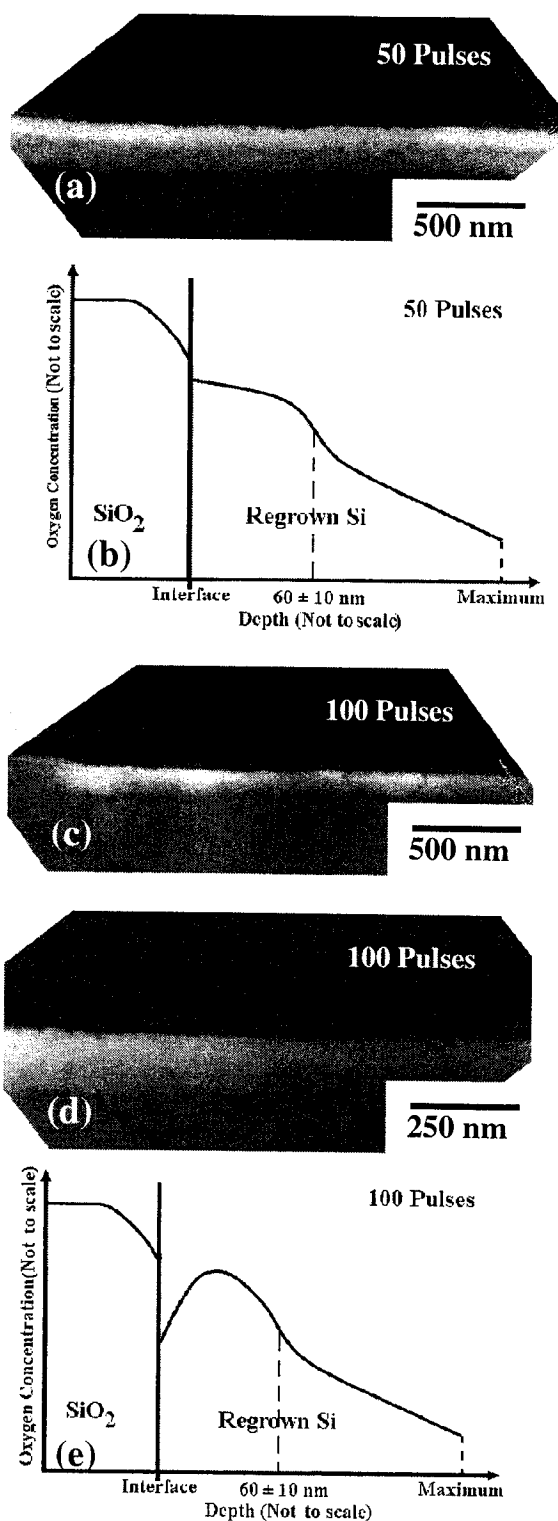
Fig. 7.9 (a) TEM image taken from a LDR fabricated by FC #2; (b) Schematics showing oxygen depth profile of (a); (c) and (d) TEM images, at lower and higher magnification, taken from a LDR produced by FC #3; (e) Schematics showing oxygen depth profile of (d).

Si melting pool during the first 50-pulse irradiation: (i) impurity diffusivity on melting is several orders of magnitude higher than that in solid; (ii) the melting time increases from the bottom of the melting pool to its top; (iii) some oxygen atoms in the dielectric become mobile because Si-O bonds are partly broken. As a result, the mobile oxygen atoms diffuse rapidly into the Si melt lamella during the first 50 laser pulses and, thus, the oxygen concentration gradually decreases with depth, because the liquid Si re-solidified from the liquid/solid Si interface and the oxygen segregation coefficient is very high depending the growth velocity from liquid Si, which is exhibited by the contrast difference around the interface between the dielectrics and the Si revealed by HNA etching, in Fig. 7.9 (a).

Following the loss of mobile oxygen atoms at the bottom layer of the dielectric, the oxygen concentration there gradually decreases with increase of depth in this dielectric layer. On the other hand, during additional irradiation following the first 50 laser pulses, the oxygen atoms further diffuse from the dielectrics into the liquid, dramatically increasing the oxygen concentration in the regrown Si. Moreover, as it will be noted below, silicon atoms simultaneously diffuse from the liquid Si into the dielectrics, resulting in a thicker SiO_2/Si interface with intermediate composition SiO_x ($0<x<2$), presenting a lower reflectivity coefficient, a lower melting point and an increase of thermal conductivity at the bottom of the dielectric layer. Due to the higher thermal conductivity of the bottom oxide and the more heat dissipation there, at the end of the last pulse of 100 pulsing laser irradiation, the liquid Si grows not only from the interface between the liquid and the solid but also from the interface between the

dielectrics and the liquid, which is different from the liquid growth after the irradiation of the first laser pulses, e.g. 50 pulses above. Following this mechanism, it is very easy to understand why the TEM image in Fig. 7.9 (d), with higher magnification, presents white contrast at the dielectrics/Si interface (with a thickness of about 20 nm), and a dark contrast underneath the interface with depth variation between 40 ~ 70 nm. This dark contrast layer, with the highest oxygen concentration as shown in Fig. 7.9 (e), represents the location where oxygen atoms accumulated due to segregation during the Si re-growth from the up and down interfaces as discussed above.

Conversely, silicon atoms from the liquid can also diffuse into the bottom dielectric layer. Fig. 7.10 (a) shows a TEM image, taken from a LDR processed under
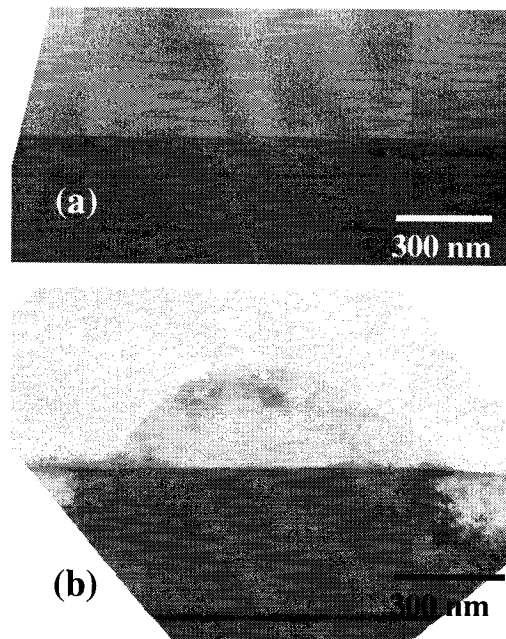
Fig. 7.10 (a) TEM image shows the microstructure of LDR under FC #3. The TEM sample was prepared along x axis. (b) TEM image shows the microstructure of sample (a) after HF etching for 22 seconds.

FC #3. This image does not show any movement of the interface between the dielectric and the resolidified silicon. After HF etching for 22 seconds, a TEM image was obtained, as shown in Fig. 7.10 (b). Above the resistive link, a Si semicircle of a radius of 300 nm suggests that the original material in that semicircle area has a lower etching rate than the SiO_2 material when it is dipped into HF solution. Therefore, in the actual LDRs, a hemisphere, containing a higher volume density of Si atoms than that (~33 at. %) in SiO_2, exists above the formed resistive link. To diffuse to a distance of ~ 300 nm in the solid oxide during the overall melting time of about 20 μs (by considering about 200 ns of melting time for each laser pulse and totally 100 pulses for this device), a diffusion coefficient (D) of ~ 10^{-5} cm^2s^{-1} should been employed. However, obviously this D is too large for Si diffusion coefficient in solid dielectrics, which should be less than ~10^{-13} cm^2s^{-1}. Therefore, this hemisphere could be not reached by the Si atoms within so short laser heating time under a usual diffusion mechanism. The possible origin for this phenomenon is that some liquid Si atoms, with high diffusivity, based on a transient-enhanced diffusion mechanism, diffused into the highly defective (mainly vacancy-rich) and hot Si dioxide materials under very high pressure during Si evaporation [204] of the top layer of the melts within the highest temperature period.

Finally, the impurity inter-diffusions, including oxygen diffusion from the dielectrics into the liquid Si and silicon diffusion from the liquid Si into the dielectrics, are summarized in Fig. 7.11. During the first laser pulse, surface silicon is melted and, then, silicon and oxygen atoms start to inter-diffuse between the dielectrics and the liquid Si as schematically shown in Fig. 7.11 (a). As the number of pulses increases to

50 pulses and then to 100 pulses of laser irradiation, the dielectrics close to the

dielectrics/Si interface becomes SiO_x and the regrown Si becomes SiO_y as schematically

First Pulses

SiO₂

O

Si   Si

(a)

50 Pulses

SiO₂ $SiO_x(1.97<x<2)$

Si $SiO_y(y<0.01)$

(b)

100 Pulses

SiO₂ $SiO_x(1.97<x<2)$

Si $SiO_y(y<0.01)$

(c)
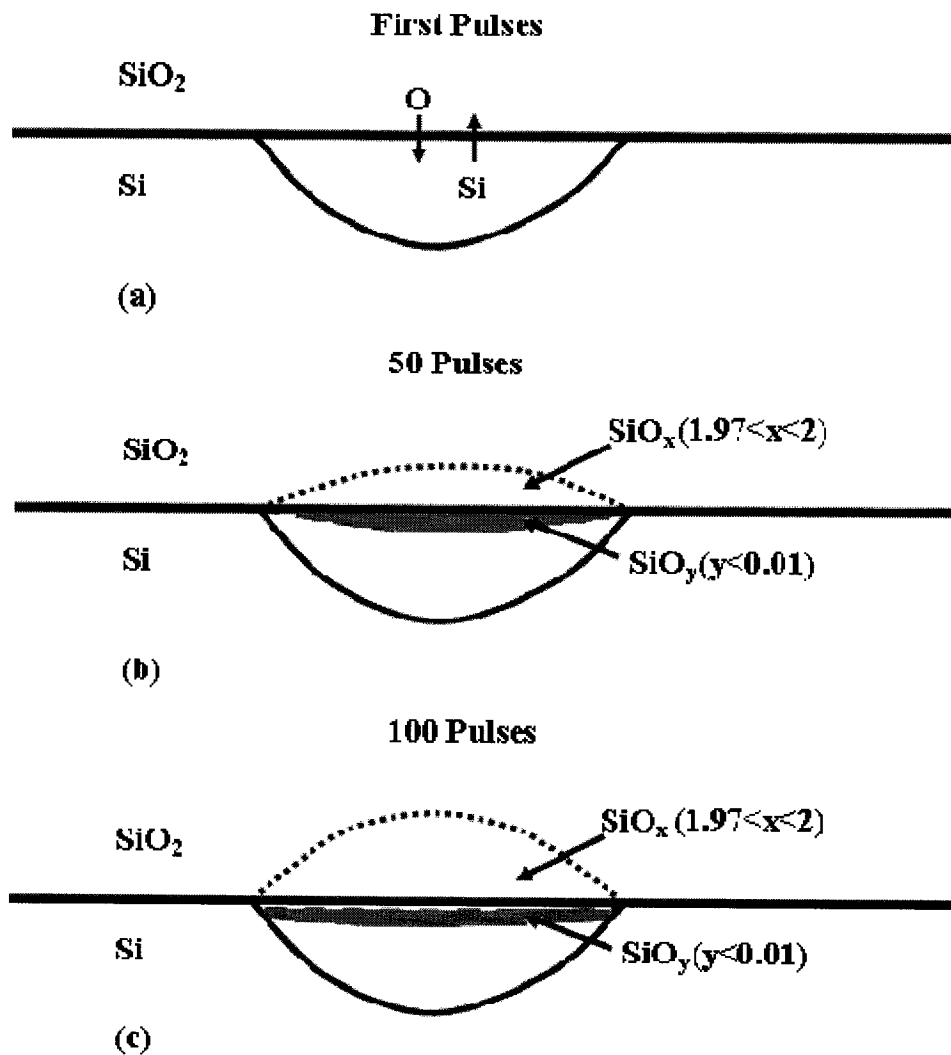
Fig. 7.11. Schematics showing oxygen and silicon inter-diffusion after first (a), 50 (b), and 100 (c) laser pulses. The figures are not scaled. The maximum horizontal dimension of the hemisphere of the melted Si can reach about 2.5 μm with laser beam of 4 μm in diameter and the maximum vertical dimension of the hemispheres of the melted Si and modified SiO_2 can reach about 500 nm and 300 nm, respectively, depending on the light intensity and pulses.

shown in Fig. 7. 11 (b) and (c). Results suggest that this is the case, even when the laser intensity is not high enough to melt the dielectrics. The values of x and y can be estimated as $1.97 < x < 2$ and $y < 0.01$, respectively, by considering the sensitivity (~ 1 at. %) of EDX (energy dispersive X-ray) analysis because no impurity differences in the laser irradiated dielectrics and Si are detectable.

7.6. DISLOCATIONS

There are several mechanisms of dislocation formation in laser-processed Si and all findings are summarized in Fig. 7.12. Each mechanism will be discussed below.

Dislocation formation due to clustering of point defects during thermal annealing -- Dislocations, which do not propagate during the LFT, are formed during laser-induced thermal annealing. It is different from the phenomenon, as shown in Fig. 7.4 (a) and Fig. 7.10 (a). Fig. 7.13 (a) shows threading dislocations, on a flat device and a field oxide device, after LFT and laser-induced thermal annealing processes, based on FC #5. The TEM samples were prepared along x axis. This type of dislocations exists over the entire melting range, induced by laser irradiation. As discussed in Section 7.4.2, supersaturated vacancies and interstitials are formed at the end of Si melting. These point defects are nonequilibrium defects, which increase the free energy in the resolidified hemisphere. Thus, there exists a thermodynamic driving force to drive point defect aggregation and, then, clustering, yielding to a reduction of the density of the isolated point defects and to the formation of dislocations. As indicated in Fig. 7.12 (a), under laser heating with energies lower than melting threshold, the region previously melted is heated to certain temperatures below the Si melting point. At random locations in the re-solidified Si film, with a highest density of vacancies or/and interstitials as indicated in Fig. 7.8 (a), dislocations are easily created in order to minimize the free
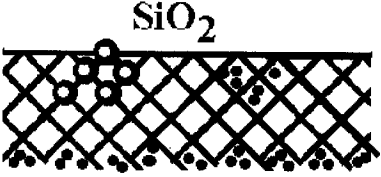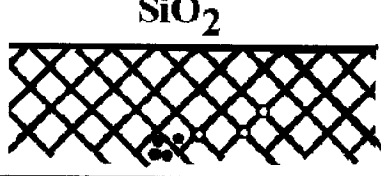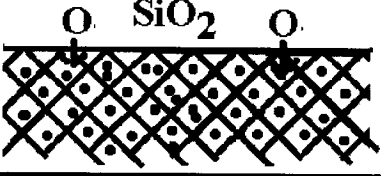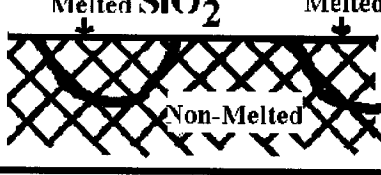
Type	Schematics	Formation Mechanisms
(a)	SiO$_2$	• Clustering of interstitials or vacancies at the surface or in the bulk of Si • Dislocations formed during thermal annealing
(b)	SiO$_2$	• Dislocation formed during crystal growth • Non-equilibrium point defects condense to form dislocations
(c)	O SiO$_2$ O	• Oxygen atoms are interstitials • High oxygen concentration in regrown Si
(d)	Melted SiO$_2$ Melted Non-Melted	• Thermal stress • Oxygen diffusion

Fig. 7.12 Schematics of mechanisms of dislocation formation.

energy of the materials. These dislocation generation locations could be at the silicon side close to the interface between the dielectric and the Si, inside the laser melted volume. For example, the location marked in Fig. 7.13 (a) should contain a very high concentration of vacancies, appearing as a contrast similar to that of amorphous Si. The dislocations first created at that site extend and split into some upward and downward dislocations. The upward dislocations grow following the paths at relatively high concentration and, then, end at the interface. Several downward branches end after extending over ~50 to ~150 nm. The extension of the other two dislocations starts from the vacancy supersaturated site and, then, both of them stretch downward. Once the dislocations reach the boundary between vacancy-rich and interstitial-rich regions, a simultaneous contraction of both defects occurs. They move close to each other to a
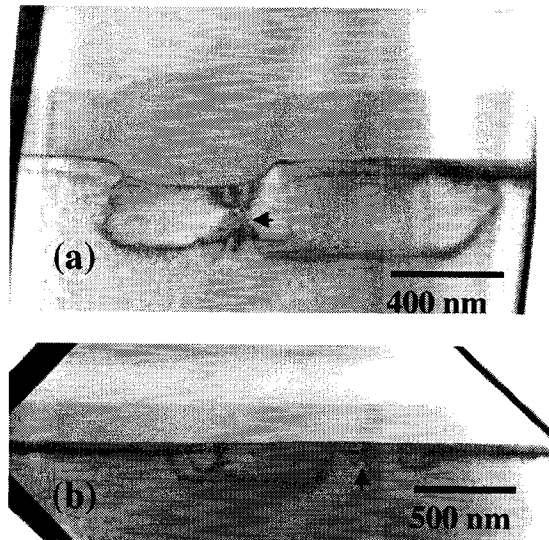
Fig. 7.13. TEM images obtained from LDRs produced under FC #5 (a) and under FC #3 with thermal annealing at temperature about 250 °C for several days (b).

distance of about one atomic volume; some vacancy-interstitial pairs can recombine [233]. However, the vacancies and interstitials, which are far from each other, cannot recombine during the processing period of the 100 μs laser irradiation. Under this thermal stress, those interstitials or vacancies may condense and become precursors of dislocation extension. Therefore, after condensation of nonequilibrium point defects, the two dislocations climb towards left and right, respectively, along the highest strain lines, which are most likely the boundaries between non-melt and melt Si [182]. During the extension of the dislocations toward the lateral edges of the regrown volume, it is possible that the dislocations meet sites, above the bottom boundary between the regrown layer and the bulk Si, containing extremely high concentrations of vacancies or interstitials and, thus, they may extend up toward, and end at, the interface between the dielectric and the Si, as shown in Fig. 7.13 (a). Based on TEM plan-view imaging, it is seen that most threading dislocations extend along the <111> Si crystalline orientation. However, the length of the dislocations existing in the devices processed under FC #5 is not identical. Furthermore, some LDRs, based on FC #3, were prepared for thermal

annealing at temperature of ~ 250 ^{0}C for several days; similar phenomena of dislocation formation were also observed, as shown in Fig. 7.13 (b). Moreover, dislocations formed based on this mechanism were also found in other microdevices, annealed with non-melting laser irradiation, fabricated with various number of laser pulses, e.g. with 10 pulses, as shown in Fig. 7.3 (a).

Dislocation formation due to condensation of point defects during Si regrowth
-- The second formation mechanism involves dislocation propagation during the crystal growth as schematically indicated in Fig. 7.12 (b). Fig. 7.14 shows TEM images, taken from FIB-prepared samples cross-sectioned along the y axis, from LDRs fabricated by FC #2 and FC #3, respectively. Fig. 7.14 (a), taken from a LDR with 100 pulses of laser irradiation, clearly shows dislocations, while Fig. 7.14 (b), with 50 pulses, does not show
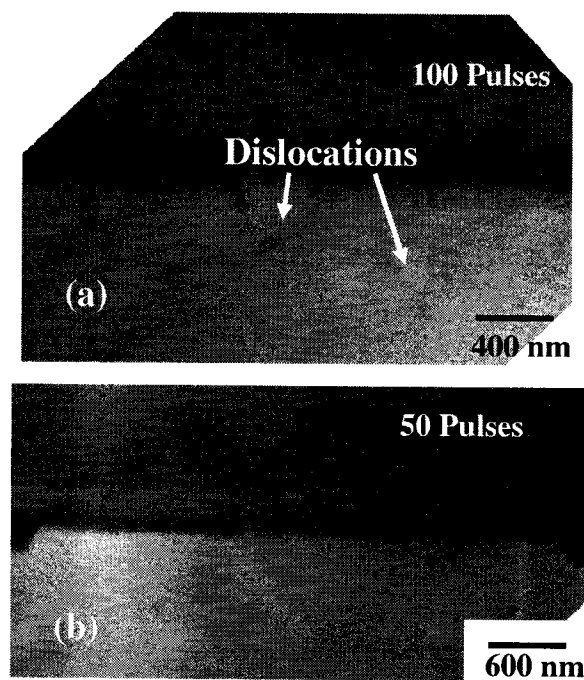
Fig. 7.14 (a) TEM image at high magnification, taken from a microdevice fabricated by FC #3. (b) TEM image, showing the cross-section of the entire resistive link, of an microdevice fabricated by FC #2. The two TEM samples were prepared along y axis.

any dislocations. The two cases have the same laser processing time of 100 µs, however, the absorbed energy, by the silicon material, with 100 pulse of laser irradiation is two times of that with 50 pulses of laser irradiation. Therefore, the local substrate temperature at the end of laser pulsing, underneath the melting pool, for 100 pulse irradiation is higher than that for 50 pulses of irradiation. For the case of 100 pulses, some non-equilibrium point defects have enough time, due to relative longer cooling time at the end of melting of the last laser pulse, to condense together to form dislocations, during movement of liquid/solid interface, reducing the free energy of the crystalline film. This phenomenon is similar to the case when dislocations are formed in samples that one cooled quickly from 1300 ^{0}C to room temperature [234]. Because these dislocations are formed during the growth process, they are inclined and follow the motion of the liquid/solid interface and of the path of the high concentration point defects. As shown in Fig. 7.14 (a), this type of dislocations does not follow the bottom of the deepest liquid/solid interface. Those dislocations are different from the threading dislocations, which, as shown in Fig. 7.3 (a) and Fig. 7.13, are located at the boundary between the deepest regrown and the original (non-melted) bulk Si, indicating the maximum melted depth. This dislocation dependence on the resolidified Si thickness is in good agreement with that suggested by Romanov et al. [35].

It is interesting to note that, in Fig. 7.14 (b), when only 50 pulses are used, no dislocation is observed. This case was found in all 5 LDRs produced with the same fabrication parameters. We can deduce that after irradiation by only 50 laser pulses, except the melting area the temperature of the local substrate is almost remaining at room temperature and the crystal grows rapidly following the quenching process; therefore, no visible dislocations were formed in this type of devices.

Dislocation formation due to oxygen diffusion -- The third mechanism of

dislocation formation, found in laser-processed micro-devices, involves dislocations

generated due to oxygen diffusion as indicated in Fig. 7.12 (c). Fig. 7.15 (a) and (b)

shows plan-view TEM images taken from one LDR fabricated by FC # 4, before and

after etching the dielectric materials, respectively, using HF solution. Those etched

dielectric materials were left on one side of the TEM sample after FIB preparation. Fig.

7.15 (a) shows the threading dislocation network under bright field imaging conditions.

Fig. 7.15 (b) does not reveal the dislocations but, shows the topography of Si in the

laser-tuned area, inside the circle, indicating the boundary between the regrown Si and

the dielectric. The false topography contrast, outside the circle, was not formed by

surface roughness but by strain defects left after implantation and thermal annealing.

The diffraction image shown in Fig. 7.15 (c) confirmed that the laser-tuned region in the
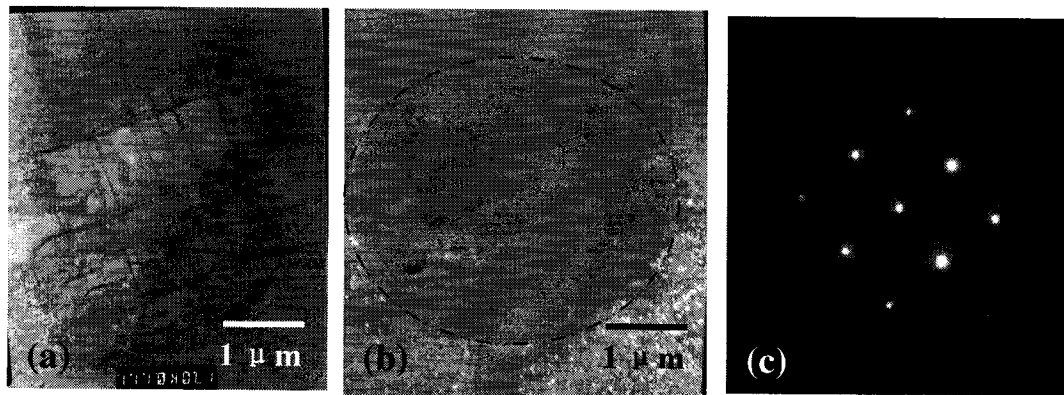
Fig. 7.15 (a) Plan-view TEM image reveals dislocation distribution in a LDR based on FC #4. (b) TEM image, taken from (a) after etching the dielectric using HF solution. (c) Diffraction image shows that the laser tuned area remains monocrystalline after oxygen diffusion.

device remains crystalline. The high density of threading dislocation network does not

exist in the LDRs with less than 100 laser pulses. Therefore, the solidification rate should not be the main reason to form this network. However, as discussed in Section 7.5, mobile oxygen atoms diffuse from the dielectric into the liquid Si during melting. As the number of laser pulses increase, more oxygen atoms diffuse and get deeper into the silicon. After a certain melt duration, the concentration of oxygen atoms at the bottom dielectric layer approaches almost the same level as that in the top layer of the melting silicon and, as a result, the dielectric in this volume melts due to its lowered melting point according to its phase diagram [39]. That is the reason why the rough topography in Fig. 7.15 (b) is observed after etching the dielectric layers. Therefore, after melting over a sufficiently long time, the entire melting pool contains a high concentration of oxygen atoms. From AFM measurement on the topographic roughness, caused by oxygen diffusion from the dielectrics and by partially melting of the bottom dielectrics as presented in Chapter 5, the oxygen interstitial level in the regrown Si is greater than 10^{20} atoms/cm^3, which is above the saturation limit for temperatures below 1500 K [235]. Nevertheless, the process of Si re-crystallization becomes complicated when the oxygen concentration is so high. The oxygen atoms precipitate out of liquid when the melting pool is cooling down. Therefore, the condensed oxygen-rich clusters take the places of atom sites of crystalline silicon and, then, some Si atoms become interstitials. At the same time, some oxygen atoms also become interstitials. Those oxygen precipitates, oxygen interstitials and silicon interstitials induce a high misfit strain at the boundary between the re-solidified Si and the Si bulk, which, in combination with the motion of interstitials and precipitates, creates dislocations,

enhances dislocations to climb due to dislocation absorption of interstitials, and glides during relaxation of the misfit. A possible model for these dislocations is pure-edge interstitial dislocations [98], formed from the uncoordinated Si dangling bonds [67]. During the cooling period of the regrown Si layer, the interstitial oxygen atoms will mostly disappear, resulting in more precipitates formed; consequently the initial dislocations will further propagate and/or more dislocations will be generated. Furthermore, the reason why dislocation density in the region closer to the interface between the dielectric and the regrown Si layer is higher than that in the deeper region in the tuned device with less than 150 pulses, as indicated by the arrow in Fig. 7.13 (b), may also be oxygen precipitation.

Dislocation formation due to thermal stress in periodically melted LDRs -- Fig. 7.16 shows dislocations, formed by periodic melting, as indicated in Fig. 7.12 (d), when a linearly polarized laser is used (see Chapter 5) [199]. The TEM sample, taken from a microdevice fabricated by FC #3, was prepared by FIB along the y axis. This formation mechanism is suggested to be a combination of thermal stress and oxygen diffusion as indicated in Fig. 7.12 (d). The areas, marked with M, are regions where melting occurred, and the area marked with N, is a region where the dark contrast indicates the strain defects left due to implantation and thermal annealing, revealing non-melting there. Those dislocations, shown in Fig. 7.16, vertically follow the boundaries between melting and non-melting regions and, meet both at the bottom of the melting and at the interface between the dielectric and Si. During the irradiation of the 100 laser pulses, the

boundary between melted and non-melted regions has a low lateral temperature gradient and, thus, the temperature in the non-melting region is also rather high. As a consequence, the thermal expansion in the periodic solid is noticeable. Therefore, the thermal mismatch between the hot solids and the cold substrate leads to a rather high tensile stress field, which is relaxed by local crack formation [236]. Dislocations are horizontally extended at the bottom of the melted regions, according to the point defect mechanism discussed above, and then climb vertically, following the crack during
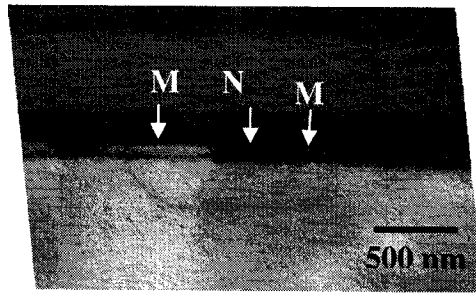
Fig. 7.16 TEM image was taken from a laser trimmed microdevice
with polarized light based on laser parameters of FC #3.

crystal growth. Interstitials that were injected by oxygen precipitate may also contribute partly on the dislocation formation. In this way, once periodic melting exists, dislocations are easily generated.

7.7. MASS TRANSPORT DUE TO LIQUID CONVECTION

Fig. 7.17 shows AFM images, taken from LDRs based on FC #3. Fig. 7.17 (a) was imaged after the dielectric layers were etched by HF solution. After additional HNA etching for 12 s, Fig. 7.17 (b) and (c) were obtained from the device in Fig. 7.17 (a) and

another device fabricated under the same laser conditions, respectively. Previously, laser-induced Marangoni convection on the free surfaces of absorbing materials and melts was considered as a result of influence of temperature gradient on the liquid surface tension [225-226][237]. This liquid flow can dominate the transport of both heat and mass in melts. In our case, the silicon surface is covered by a dielectric containing oxygen and silicon. Under focused laser irradiation, the highest temperature is reached at the centre of liquid Si close to the interface between the dielectric and liquid Si due to the longest illumination time and highest laser intensity. The temperature gradient results in a variation in the liquid interface tension; consequently, this provides a shear stress at the interface, inducing liquid motion, as shown in Fig. 7.18.

The liquid convection, induced by the temperature gradient, causes both heat and mass transportation. When a negative temperature derivative of the surface tension of the melt ($d\sigma/dT < 0$) occurs, the surface stress in the center of the melt pool is much lower than at the edges. As shown in Fig. 7.18 (a), under laser irradiation, the silicon material in the hemisphere was heated and melted. At the center of the melting pool, the Si liquid quickly moves from the bottom to the top, due to the significant temperature gradient. The lateral velocity of the liquid Si along the interface between the dielectric and liquid gradually decreases from the centre to the circular edges, arriving at a minimum value, which is smaller than that along the vertical direction at the center axis of the melt. Moreover, the liquid velocity, at the bottom of the hemisphere, gradually increases from the circular edge to the axis. The liquid velocity along solid Si at the bottom of hemisphere decreases faster than that along the interface between the
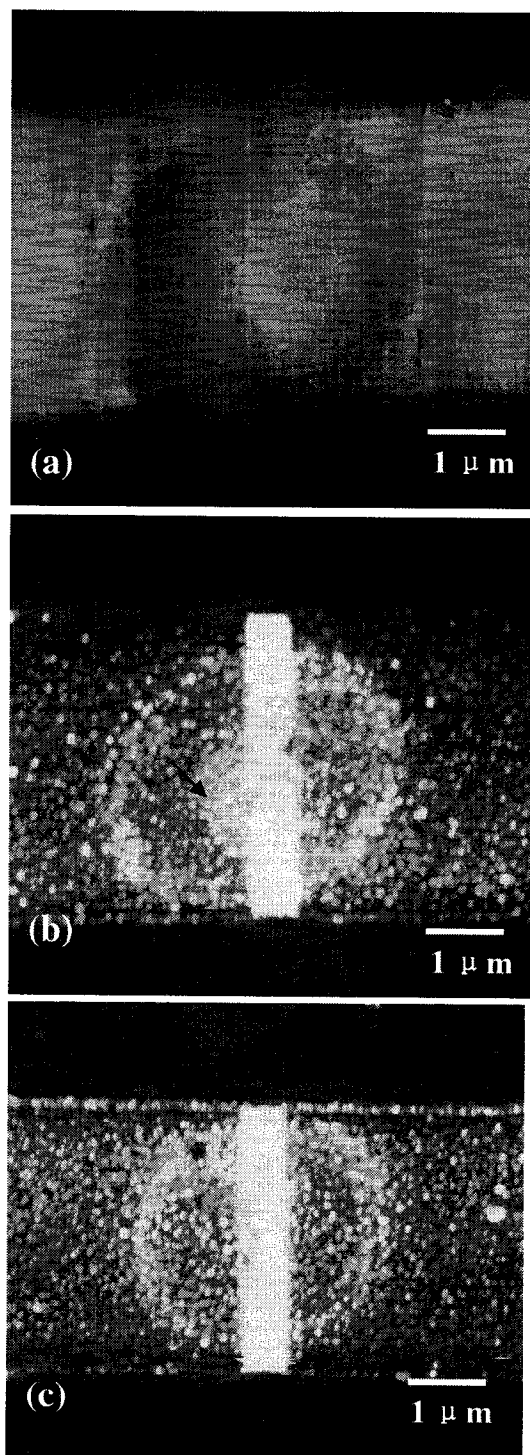
Fig. 7.17 (a) AFM image taken from one LDR based on FC #3;
(b) AFM image, of sample (a), after additional HNA etching;
(c) AFM image taken from another LDR based on FC #3.

dielectric and liquid Si because the heat dissipates into Si very fast. Therefore, the

average liquid velocity along solid Si is certainly lower than that along the dielectric/liquid Si interface. On the other hand, as discussed in Section 7.5, SiO_2 bonds are partly broken and some mobile oxygen atoms diffuse into the top melt as shown in Fig. 7.18 (a); consequently, the oxygen concentration is very high in this layer. The horizontal convective flow brings the oxygen atoms of this layer toward the edges of the melting pool, which is a circle at relatively low temperature and at the lowest flow velocity. The oxygen area density in this circle, defined from the top view, is the highest in the melting hemisphere. Those oxygen atoms are partly electrically activated, act as n-type dopants [68], and compensate p-type dopants; therefore, the concentration of net carrier (holes) there is lower than that in the rest of the source and drain regions. Thus, the etching rate along the circle is notably smaller than that of the rest of the area, as revealed by the fact of the higher topography along the white circles, as shown in Fig. 7.17 (b) and (c), obtained after HNA solution had etched the doped Si materials for a thickness of about 400 nm. It should be pointed out that the area close to the melting center, and marked in Fig. 7.17 (b) with high topography, might be caused by a large amount of oxygen atoms, diffused into this area by oxygen flow at a very high flux because the dielectric there was at a very high temperature. However, Fig. 7.17 (c) does not show this phenomenon. Moreover, the presence of convection is also seen from the fact that the area at the laser-irradiated center, and immediately underneath the heavily doped range, moves up; this can be seen from the contrast comparison there, as shown in Figs. 7.6 (a) and (b). Another phenomenon is that oxygen transportation, due to convection, induces oxygen aggregation in the liquid at the interface between the

dielectric and the melting Si, along the melting edge; therefore, a lower topography is observed in Fig. 7.17 (a) after etching the dielectric multilayers with HF solution. However, the fluid flow, generated during melting, rapidly decays during solidification.

It should also be mentioned that the melt becomes elongated because heat is also transferred from the center to the circular border. Moreover, from Fig. 7.18 (b), it can be
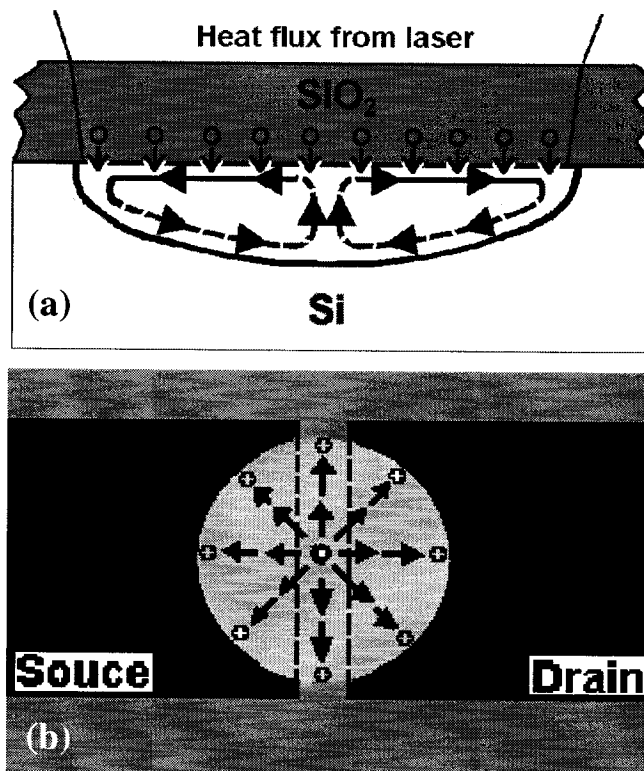
Fig. 7.18 (a) and (b) Cross-sectional and top-view schematics of convection action under laser irradiation.

seen that the resistive link formation is a result of the competition between dopant diffusion from the two heavily doped areas, and mass transportation due to convection. The dopant (boron) is driven into the initial gap from the heavily doped source and drain during melting; however, convection brings them back into the heavily doped areas. When the laser power is increased, or the size of the beam is reduced, the Marangoni

phenomenon is also enhanced [226]. Therefore, in order to minimize convection, low laser beam intensity, inducing thinner layer of melt, and laser pulse(s) with shorter pulse duration, in practical LFT technology, should be used.

7.8. CONCLUSION

The microstructures of laser-processed microdevices, fabricated by LFT, as well as additional laser-induced annealing, have been extensively studied by TEM, AFM, and chemically selective etching. The mechanisms of the formation of point defects, dislocations, interdiffusion of oxygen and silicon, and mass transportation due to convection, have been discussed. Schematic 2D distribution of point defects, including vacancies and interstitials, in the LDRs have been presented. The shorter the melting time, the higher the concentration of native point defects. However, increasing the melting time will lead to more the dislocations. Convection-induced mass transportation also affects the resistance value of the LDRs. Strong interdiffusion of materials, involving diffusion of oxygen atoms from the dielectric into the molten Si, and diffusion of Si atoms from the molten Si into the dielectric, as well as liquid convection, occur when a high intensity laser beam and/or longer pulse duration are used. Those results have indicated the direction of the optimization of the LFT technique, by adjusting these laser parameters.

CHAPTER 8. GENERAL DISCUSSION AND CONCLUSION

8.1 GENERAL DISCUSSION

In the analog integrated circuits, especially high-speed mixed-signal IC applications, including D/A and A/D converters, severe requirements are imposed on the accuracy of resistors in the integrated circuits. However, the values of resistance generally have previously deviated from designed values due to the variation of fabrication conditions. In order to achieve high accuracy beyond the limitation of the process control, it is necessary to adjust the resistance values in ICs after the fabrication process. Several resistor trimming techniques have been developed for altering the resistance values to compensate for process deviations. For example, laser trimming by ablation, laser annealing of polysilicon resistors and aluminum migration into diffused or polysilicon resistors have been employed for resistor trimming. However, almost all of them have their disadvantages, for instance, large area and/or complex additional fabrication process needed to obtain the trimmable resistors.

As an alternative approach to fabricate highly accurate resistors, laser fine tuning (LFT) is compatible with CMOS fabrication flow. The LFT is performed on a silicon micro-device structure, consisting of a gateless MOSFET. For a p-type resistor, the device structure consists of two highly boron doped regions, formed by ion implantation into an n-well and separated by initial gap (L), resulting into two facing p-n junctions. The device has a width of W with a typical value of 4 μm and the electrical connections to the devices are through vias. Finally, dielectric multilayer protects the device. Before LFT is performed, the only current, which is leakage current through two facing p-n junctions in the device, is very small, resulting essentially in an open circuit. By focusing an intense laser beam on the gap area and a part of heavily doped regions contacting with the two junctions the melting of Si material drives dopant diffusion from the highly doped regions into the lightly n-type gap region. After removing the laser beam, the silicon becomes resolidified, resulting in the locally diffused and electrically

activated redistributed dopants in the area of the former gap and, therefore, forming an electrical link between the highly doped regions.

The microstructure and dopant distribution of the resistors, induced by laser irradiation with various light parameters, were obtained by microstructural analytical methods, such as TEM (transmission electron microscopy) and AFM (atomic force microscopy), in combination with chemically selective etching technique, as well as SCM (scanning capacitance microscopy).

As shown in Chapter 4, the LDRs have non-uniform dopant distributions which depend on the temporal and spatial temperature profile and melt zone dynamics. Furthermore, as indicated in Chapter 6, those dopant distributions strongly depend on the initial dopant concentrations in heavily doped regions - nominal source and drain, the irradiation durations of the laser pulses, the intensities of the laser beams, the spot sizes of the laser beams, etc. The net majority carrier distribution in LDRs depends on the electrically activated impurities such as oxygen atoms, which could compensate the dopants.

According to the characterization of microstructures in the LDRs shown in Chapter 7, we can expect that some defects or phenomena listed in Table 8.1 could affect the LFT fabrication process as well as the electrical properties and/or stability of the produced LDRs.

Point defects are formed due to high cooling rate of the liquid Si. They could enhance the dislocation formation and affect the electrical stability of LDRs. To avoid the formation of point defects, one should lower the cooling rate by increasing the solid silicon temperature surrounding the melted zone. Increasing the temperature of the entire IC is not practicable since to significantly alter the temperature gradient, one must increase the temperature to the temperature, at which inter-diffusion of materials (mostly metals) would become important, destroying the devices. To possibly overcome that problem, it is proposed to increase the temperature locally by using a longer pulse duration of laser heating. In this case, care must be taken to limit the O and Si inter-

diffusions between the dielectrics and the melts as well as convection which will be

Table 8.1. Summary of microstructural phenomena in LDRs.

Phenomena	Characteristics	Possible effects on LDRs	Possible methods to overcome
Point-defects	-- High density of point defects induced when high cooling rate is obtained	-- Possible electrical instability	-- Decrease the cololing rate by locally increasing the temperature
Dislocations	-- Point defects, oxygen diffusion and periodic melting enhance dislocation formation	-- Increase resistance value by forming energy barrier at dislocations -- Electrical instability	-- Avoid point defects, O and Si inter-diffusion. -- Avoid periodic melting
Liquid convection	-- Enhanced by high laser intensity -- Enhance by longer pulse duration	-- No direct effect on electrical stability of LDRs -- Affects formation of resistive links	-- low intensity of laser beam -- Shorter pulse duration

discussed below

As shown in Table 8.1, dislocation can be induced by introducing point defects, diffused oxygen from the dielectrics and the periodic melting. The formed dislocations increase resistance value by forming energy barrier due to dangling bonds and also induce electrical instability of LDRs due to the high diffusion coefficients of impurities at the dislocations. To avoid dislocation formation, point defects, O and Si inter-diffusion should be suppressed and periodic melting should be avoided by using circularly polarized laser beam.

Liquid convection is enhanced by high laser intensity and by long pulse duration. There is no direct effect on electrical stability of LDRs due to liquid convection. However, as shown in Section 7.7, the liquid convection strongly affects the dopant/impurity redistribution during LFT process, thus influencing the final resistance value. Therefore, liquid convection should be avoided by using low light intensity and short laser pulse duration.

8.2 CONCLUSION

Different laser diffused resistors (LDRs) were fabricated by LFT under various processing conditions and were physically characterized in order to completely understand the laser- process itself and accurately control the electrical and material properties of the LDRs. The microstructure and dopant distribution of the resistors were characterized by various analytical techniques such as TEM, SEM, AFM, SCM in combination with chemical etching process.

Firstly, this work has experimentally demonstrated that the dopant atoms diffuse from the heavily doped source and drain regions into the lightly doped gap region by dopant selective etching (DSE) process and scanning capacitance microscopy (SCM), revealing that the electrical link can be formed, as a consequence of the disappearance of the two opposite p-n junctions.. The re-distributed dopant concentration inside the melted area of the original gap is lower than those in the initial source and drain regions. This lower dopant concentration induces higher resistivity, than that in the source and drain regions, forming the main LDR resistance. The two-dimensional (2D) dopant profiles, in the range of 9×10^{16} to 3.6×10^{18} atoms/cm^3 and quantified using an optimized DSE in combination with cross-sectional transmission electron microscopy (TEM) method, in laser diffused silicon resistors shows the non-uniformity of dopant distribution. This dopant evaluation method considered the chemical etching rate as a vector instead of a scalar. Those evaluated profiles show that the numerical simulation models, developed in our research group, based on a three-dimensional transient temperature field model (TTFM) and using out-of-equilibrium heat transfer and diffusion equations, are correct.

Secondly, the formation mechanism of the periodic submicron-resistors was studied using TEM, SEM and numerical simulation. By performing careful plan-view TEM samples and cross-sectional SEM samples prepared by FIB, we demonstrated that two-dimensional (2-D) periodic coexisting of liquid and solid exists (0.9<I<1.08 W) and

is responsible for the formation of periodic submicro-resistors. The periodicity of these structures is 360 nm, related to the wavelength of frequency doubled Nd:YAG laser (532 nm) and the index of refraction of SiO_2. We propose a model based on the fact that oxygen atoms are diffusing locally from SiO_2 into the melted Si, thus forming SiO_β with a lower melting point than that of pure Si; successive laser pulses melt preferentially these regions giving rise to a positive feedback. Moreover, when the light intensity is out of those ranges, either the periodicity of submicron resistors were not formed or destroyed because no melting was created (I<0.9 W) or periodic melting was destroyed (I>1.08 W). Dynamic nanoscale modeling, based on variations of melting points of Si and dielectric and reflection coefficient, confirms the experimental results.

It is also shown that arrays of periodic boron doped Si submicron resistors can be fabricated in silicon covered by SiO_2, under polarized Nd:YAG laser irradiation. In these experiments, a focused spot size less than 3 μm is used. By using scanning capacitance microscopy (SCM), electrical measurement and TEM technique, it was found that the number of submicron resistors in each device depends only on laser intensity, while their average width strongly depends on both laser intensity and number of laser pulses.

Thirdly, the microstructures of LDRs under different laser conditions and initial structures were presented by means of TEM and AFM, in combination with chemically selective etching technique. It is concluded that the diffusion of oxygen atoms, from the dielectrics into the liquid Si, is responsible for the formation of dislocations. It could also act as a donor which compensates acceptors, thus increasing the resistance when more than 100 laser pulses are used. Liquid convection has been observed and is responsible dopant/impurity redistribution in the melted silicon. Dislocations, presenting energy barriers for carriers in the regrown Si, are observed and are due to point defects and diffused oxygen atoms. Furthermore, it is shown that the vacancies, existing at the regrown Si surface, cannot be avoided in the LDRs fabricated in any LFT conditions, but point defects can be limited in the regrown bulk Si. On the other hand, it is possible to produce LDRs with dislocation free under quenching process. Those characterization

results could be extended to expect possible structural formation of LDRs with various initial structures for fabricating various p^+-v-p^+ and n^+-π-n^+ resistors.

8.3 RECOMMENDATIONS FOR FUTURE WORK

Although this thesis can serve as an initial understanding on the insight-view of the microstructures and mechanisms which take place during the fabrication of the LDRs, additional works couild be undertaken to better understand some of the interpretations made from the empirical data. The following suggestions should achieve further and complete knowledge of the physical mechanisms finally controlling the electrical behaviors of the LDRs.

● After laser irradiation, the physical properties, such as the thermal conductivity, of the bottom layer of the dielectrics (SiO_2) are expected to be altered by the inter-diffusion of oxygen and silicon atoms across the dielectrics/liquid interface. Further measurements and modeling of its physical property variation as a function of laser conditions have to confirm this hypothesis.

● A more detailed study should be performed on the effects of point defects on electrical properties. For instance, scanning capacitance microscopy (SCM) in combination with rapid thermal annealing (RTA) could be used for this evaluation.

● Laser reflectivity variation dependence on oxygen concentration change in the dielectrics and the regrown Si close to the dielectrics/Si interface should be investigated in order to understand the actual energy transformation in the gateless MOSFET system due to laser irradiation.

● Dopant transport due to liquid convection, formed under focused laser irradiation, should be quantified in order to completely control the fabrication process for

industrial application. This could be done by using the developed DSE (dopant selective etching) technique.

- In order to produce perfect crystalline silicon for improving the quality of the regrown Si, it is necessary to find out what are the exact values of cooling rate and V/G to avoid point defects after laser induced melting. The developed chemical etching process should be very helpful on this point.

- Some endeavour can be tried to produce high quality LDRs by following the ideas presented in Section 8.1. Those include a lot of work in optimization of initial device structures, laser processing, optical modification, and electrical measurements.

APPENDIX A FIB-TEM SAMPLE PREPARATION

In order to have microstructure analysis, samples for imaging by transmission electron microscopy (TEM) has to meet the requirement of which they must be thin enough for electrons to penetrate without excessive energy loss. For penetration of a 300 kV electron beam, silicon samples must be less than 200 nm thick if dislocation characterization or precipitates are needed. However, The TEM samples prepared for characterization of dopant and point defects, using chemical etching, should be thicker, e.g. up to 600 nm, because the chemical solutions also remove materials and, then, the TEM sample thickness will get thinner than as-prepared. In any case, the samples are required to represent the unaltered material in terms of structure, chemistry, and content of defects.

In this study, all the TEM samples were prepared using FIB technique. This method can be used to make site-specific TEM samples with sub-micron positional accuracy, using a new "lift-out" method, which requires no pre-thinning and as a result provide a rapid means of preparing an electron transparent cross-section. In this thesis, this technique was also used to prepare plan-view TEM sample because it is impossible to do it using conventional mechanical polishing technique as a consequence of only few laser diffused resistors (LDRs) in each IC device. The first steps of preparation procedures for all the FIB-TEM samples are the same, however, the last steps are different due to different purpose.

Firstly, the initial devices or LDRs should be cut in FIB system and lift-out by a tiny probe with diameter of about 1 μm. A relatively large IC device can be inserted directly into the FIB chamber and a TEM sample created straight from the IC's surface. The location of an area of interesting device can be done using the FIB microscope's imaging capabilities following the indication of the top metal lines as shown in Fig. 9.1 (a), where show 4 LDRs. As indicated in the right device in Fig. 9.1 (a), a layer of CVD-deposited tungsten is induced by a focused Ga ion beam using tungsten

hexacarbonyl [W(CO)$_6$] as precursor. This W layer is important and prevents milling or
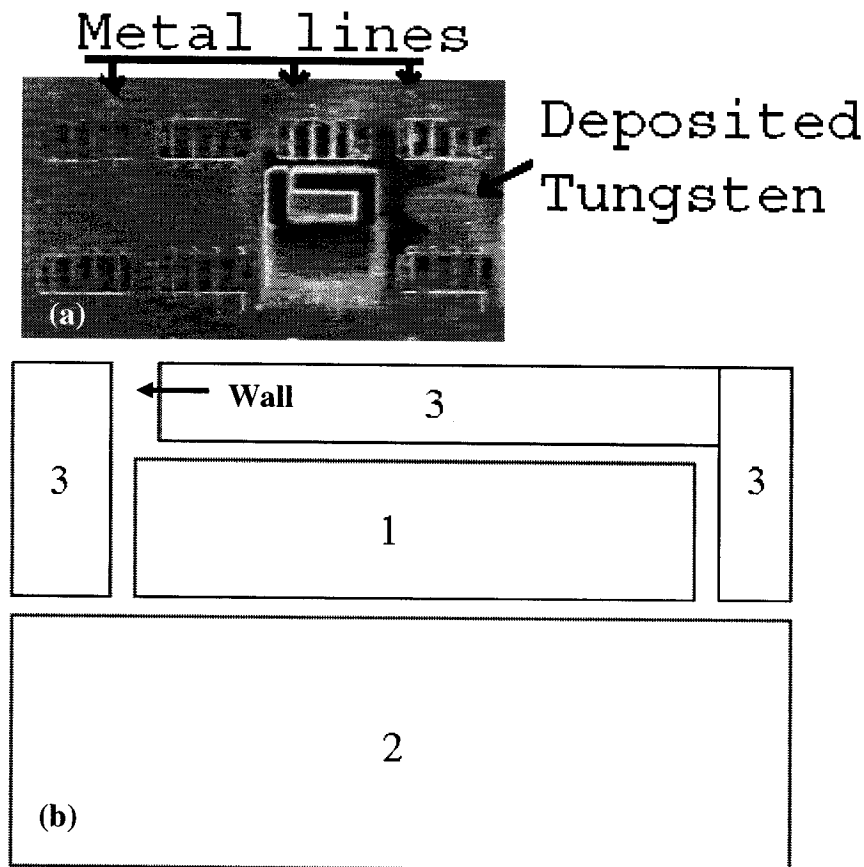
Fig. 9.1 (a) SEM image showing topography of LDRs in an IC device. (b) Schematics showing the TEM sample preparation steps.

multiple image scans from damaging the surface of the TEM sample.

Fig. 9.1 (b) shows schematically procedures of TEM sample preparation. The device is located underneath rectangular frame 1. The protecting tungsten thin film is produced on the dielectrics above the interesting device at rectangular frame 1. Using a large beam current for fast ion milling, the four trenches indicated by the four rectangular frames marked as 2 and 3 in Fig. 9.1 (b) are milled on either side of the tungsten film. The rectangular frames marked by "3" can be simultaneously obtained in only one preparation step. The trenches here have been milled so as to just leave a wall of material at one left corner that is approximately two to three microns thick. Then, the

bulk IC device and the area of interest are tilted to a steep angle, commonly 56°. The bottom cut is made at 5 μm deep underneath the silicon surface of the devices. After all the cuts here, one tiny probe is called to attach the deposited W and was fixed on that surface by tungsten deposition with a rectangular of 3μm×5μm and, then, the left wall is cut by Ga beam.

Secondly, the sample can be lifted and put into one metal grid. By following the preparation steps above, the sample can be lifted as shown in Fig. 9.2 (a). After that, holes can be made at the corner of a TEM sample grid as shown in Fig. 9.2 (b) and, then, the lifted TEM sample can be inserted and fixed, with W-deposition on both sides of the TEM sample, into the hole as shown in Fig. 9.2 (c).

9.1. Cross-sectional TEM sample preparation

By following the preparation step described in Fig. 9.2 (c), the central region of the fixed TEM sample can be thinned to less than 200 nm, e.g. for dislocation analysis, as shown in Fig. 9.3. However, for dopant analysis in resistive links of LDRs, the final thickness of the TEM sample should be less than 600 nm as indicated in Chapter 4 and shown in Fig. 4.1 (d).

9.2. Wedge-shaped TEM sample preparation for dopant calibration

Instead of only one TEM sample fixing into a sample grid, there are two TEM samples, from standard wafer and from device, respectively, fixed into one TEM grid as discussed in Chapter 4 and shown in Fig. 4.1 (a).

9.3. Plan-view TEM sample preparation

For this type of TEM sample preparation, before fixing the lifted TEM into grid, the TEM grid should be rotated for 90 degree in order to have ion-milling with Ga beam parallel to Si surface as shown in Fig. 9.4 instead of cross-sectional milling as shown in Fig. 9.2 (c). The left thickness of silicon material after final milling should be not less than 600 nm because all the dislocations, if existing, are within depth of 500
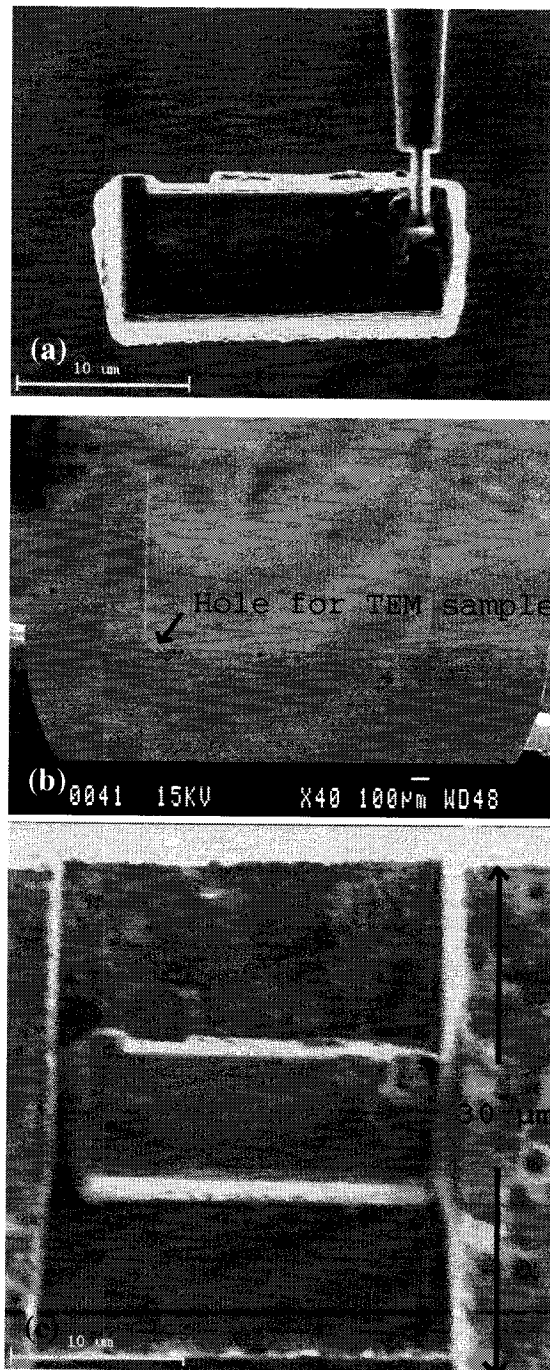
Fig. 9.2 (a) Lifted TEM sample; (b) Side-view of TEM sample grid with FIB-milled hole at the corner; (c) Top-view of a fixed TEM sample in a sample grid.

nm underneath the dielectrics/Si interface. However, this left Si thickness should be
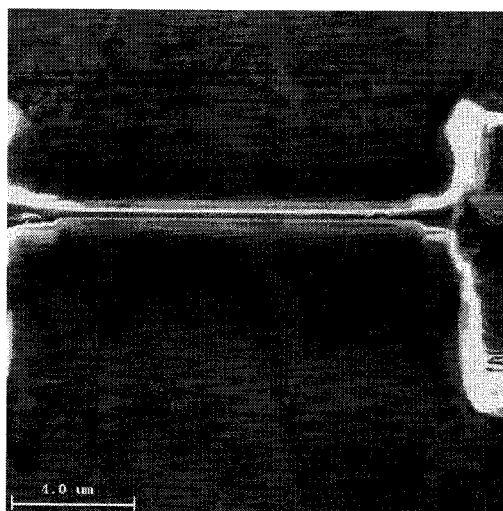
Fig. 9.3 FIB-thinned TEM sample after final milling.
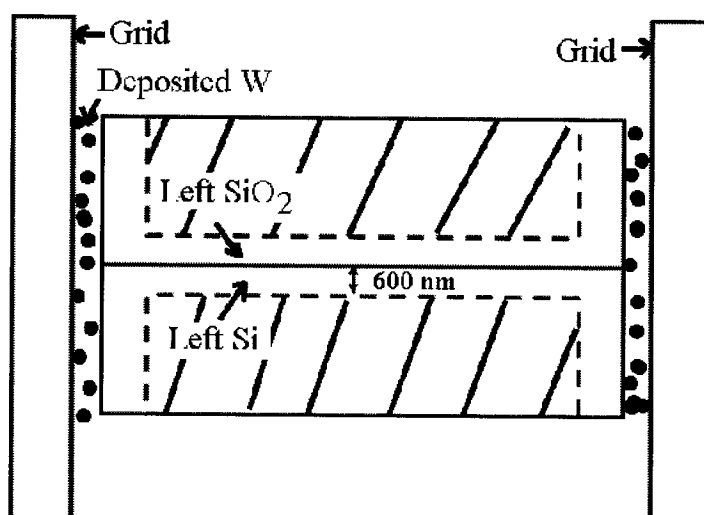
Fig. 9.4 Schematics showing plan-view TEM sample preparation. The shaded areas are removed by FIB milling.

adjusted by considering the actual dislocation depth depending on the specific laser intensity used. The other later preparation steps are the same as what for cross-sectional milling. After the final milling, the prepared TEM sample should be dipped into HF solution (~20%) to etch for about 2 minute in order to remove the left dielectrics.

For final thinning of the area of interest, the beam current must be lowered to about 0.346 nA

REFERENCE:

[1] ELSHABINI-RIAD, A. AND BHUTTA, I. A. 1993. "Lightly Trimming the Hybrids". IEEE Circuits Devices, 9, pp. 30–34.

[2] PARKER, D. L., AND HUANG, W. 1990. "Polysilicon Resistor Trimming by Laser Link Making". IEEE transations on semiconductor manufacturing, 3:2 pp. 80-83.

[3] MEUNIER, M., GAGNON, Y., LACOURSE, A., SAVARIA, Y. AND CADOTTE, M. 2001. "A New Laser Trimming Process for Microelectronics". Proceedings of the SPIE, 4274, pp. 385-392.

[4] MEUNIER, M., GAGNON, Y., SAVARIA, Y., LACOURSE, A. AND CADOTTE, M., 2002. "A Novel Laser Trimming Technique for Microelectronics". Appl. Surf. Sci., 186, pp. 52-56.

[5] DUCHARME, M., BERNIER, J.-S. AND MEUNIER, M. 2004. "Analytical Model for a Current Density Versus Voltage Relation in n+ υ n+ Devices". Semicond. Sci. Technol. 19 pp. L103–L105.

[6] MEUNIER, M., CADOTTE, M., DUCHARME, M., GAGNON, Y., LACOURSE, A., 2002. "Laser Induced Diffusible Resistance: Device Characterization and Process Modeling" Proceeding of the SPIE.

[7] TALWAR, S., FELCH, S., DOWNEY, D. AND WANG, Y., 2000. "Study of Laser Thermal Processing (LTP) to Meet Sub 130 nm Node Shallow Junction Requirements". IEEE Conference on Ion Implantation Technology, pp. 175-177.

[8] MURTO, R., JONES, K., RENDON, M. AND TALWAR, S., 2000. "An Investigation of Species Dependence in Germainium Pre-amorphized and Laser Thermal Annealed Ultra-Shallow Abrupt Junctions". IEEE Conference on Ion Implantation Technology, pp. 182-185.

[9] ALLMEN, M. VON, 1987. "Laser-Beam Interactions with Materials". Springer Series in Materials Science 2, Springer, Berlin.

[10] POATE, J. M., MAYER, J. W. (Eds.), 1982. "Laser Annealing of Semiconductors". Academic Press, New York.

[11] LIU, P. L., YEN, R., BLOEMBERGEN, N., HODGSON, R. T., 1979. "Picosecond Laser-Induced Melting and Resolidification Morphology on Si". Appl. Phys. Lett. 34, pp. 864-866.

[12] TSU, R., HODGSON, R. T., TAN, T. Y., AND BAGLIN, J. E., 1979. "Order-Disorder Transition in Single-Crystal Silicon Induced by Pulsed uv Laser Irradiation". Phys. Rev. Lett. 42, pp. 1356-1358.

[13] STIFFLER, S. R., THOMPSON, M. O., AND PEERCY, P. S., 1991. "Transient Nucleation Following Pulsed-Laser Melting of Thin Silicon Films". Phys. Rev. B 43, pp. 9851-9855.

[14] KACHURIN, G. A., PRIDACHIN, N. B., AND SMIRNOV, L. S., 1975. Sov. Phys. Semicond. "Annealing of Radiation Defects by Laser Radiation Pulses". 9, pp. 946-949.

[15] GAT, A., GIBBONS, J. F., MAGEE, T. J., PENG, J., WILLIAMS, P., DELINE, V., AND EVANS JR. C. A., 1978. "Use of a Scanning cw Kr Laser to Obtain Diffusion-Free Annealing of B-implanted Silicon". Appl. Phys. Lett. 33, pp. 389-391.

[16] DUCHARME, M. 2002. "Phénomènes de Transport dans un Dispositif Microélectronique Modifié Par Laser". Master Thesis.

[17] BÄUERLE, D., 1996. "Laser Processing and Chemistry", second edition, Springer-Verlag Berlin Heidelberg New York.

[18] DEGORCE, J.-Y., GILLET, J.-N., MAGNY, F., AND MEUNIER, M., 2005. "Three-Dimensional Transient Temperature Field Model For Laser Annealing". J. Appl. Phys., 97, pp. 033520-033526.

[19] MITEV, P. D., SAITO, M., WASEDA, Y., AND SATO, Y., 2000. "Theoretical Estimation of Diffusion Coefficients of Impurities in Silicon Melt". High Temperature Materials and Processes, 19, pp. 307-312.

[20] Kodera, H., 1963. "Diffusion Coefficients of Impurities in Silicon Melt", Jap. J. Appl. Phys., 2(4), pp.212-219.

[21] CULLIS, A. G., WEBBER, H. C., AND CHEW, N. G., 1980. "Correlation of the Structure and Electrical Properties of Ion-implanted and Laser-annealed Silicon". Appl. Phys. Lett., 36, pp. 547-550.

[22] RAVI, K. V., 1981. "Imperfections and Impurities in Semiconductor Silicon". Wiley, New York.

[23] ROZGONYI, G. A., 1983. "Trends in Defect and Impurity Control for Fine Line VLSI Processing", Defects in Silicon, Electrochem. Soc., Pennington, N. J., pp. 29.

[24] CRAVEN, R., 1985. "Internal Gettering in CZ Silicon". Matls, Res. Soc. Symp. Proc., 36, pp. 159-165.

[25] ZUHLEHNER, W. AND HUBER, D., 1982. "Czochralski Growth Silicon", in Crystals 8 (Silicon Chemical Etching), Springer-Berlin.

[26] HULL, D., 1965. "Introduction to Dislocations". Pergamon Press, New York.

[27] HIRTH, J. P. AND LOTHE, J., 1968. "Theory of Dislocations" McGraw-Hill, New York.

[28] WATTS, R. K., 1977. "Point Defects in Crystals". Wiley and Sons, New York.

[29] DOBACZEWSKI, L., PEAKER, A. R., AND NIELSEN, K. B., 2004. "Laplace-Transform Deep-level Spectroscopy: The Technique and its Applications to the Study of Point Defects in Semiconductors". J. Appl. Phys., 96, pp. 4689-4728.

[30] MICHAEL, A. E., RAUSCH, W., RONSHEIM, P. A., AND KASTL, R. H., 1987. "Rapid Annealing and the Anomalous Diffusion of Ion Implanted Boron into Silicon". Appl. Phys. Lett. 50, pp. 416-418.

[31] COWERN, N. E. B., JANSSEN, K. T. F., AND JOS, H. F. F., 1990. "Transient Diffusion of Ion-implanted B in Si: Dose, Time, and Matrix Dependence of Atomic and Electrical Profiles". J. Appl. Phys. 68, pp. 6191-6198.

[32] PELAZ, L., JARAIZ, M., GILMER, G. H., GOSSMANN, H.-J., RAFFERTY, C. S., EAGLESHAM, D. J., AND POATE, J. M., 1997. "B Diffusion and Clustering in Ion Implanted Si: The Role of B Cluster Precursors". Appl. Phys. Lett. 70, pp. 2285-2287.

[33] PELAZ, L., GILMER, G. H., GOSSMANN, H.-J., RAFFERTY, C. S., JARAIZ, M., AND BARBOLLA, J., 1999. "B Cluster Formation and Dissolution in Si: A Scenario Based on Atomistic Modeling". Appl. Phys. Lett. 74, pp. 3657-3659.

[34] YAKIMOV, E. B., 1997. "Dislocation-Point Defect Interaction on Local Electrical Properties of Semiconductors". J. Phys. III France, 7, pp. 2293-2307.

[35] ROMANOV, A. E., POMPE, W., BELTZ, G. E., AND SPECK, J. S., 1996. "An Approach to Threading Dislocation "Reaction Kinetics"". Appl. Phys. Lett. 69, pp. 3342-3344.

[36] MATARE, H. F., 1984. "Carrier Transport at Grain Boundaries in Semiconductors". J. Appl. Phys., 56, pp. 2605-2631.

[37] COTTRELL, A. H., 1948. "Report on the Strength of Solids". (Physical Society, London), p. 30.

[38] SZABO, G., 1985. "Thermal Strain During Czochralski Growth". Journal of Crystal Growth, 73, pp. 131-141.

[39] WOLF, H. F., 1969. "Silicon Semiconductor Data". Pergamon, Oxford.

[40] PIKE, G. E., AND SEAGER, C. H., 1979. "The dc Voltage Dependence of Semiconductor Grain-boundary Resistance". J. Appl. Phys. 50, pp. 3414-3422.

[41] SZE, S. M., 2002. "Semiconductor Devices, Physics and Technology". 2nd Edition, John Wiley & Sons, Inc..

[42] Gillet, J.-N., Degorce, J.-Y., and Meunier, M. 2005. "General Model and Segregation Coefficient Measurement for Ultrashallow Doping by Excimer Laser Annealing". Appl. Phys. Lett. 86, pp. 2221041-2221043.

[43] MAROUDAS, D., AND BROWN, R. A., 1991. "Analysis of the Effects of Oxygen Migration on Dislocation Motion in Silicon". J. Appl. Phys. 69, pp. 3865-3877.

[44] SAARINEN K., AND RANKI, V., 2003. "Identification of Vacancy Complexes in Si by Positron Annihilation". J. Phys.: Condens. Matter 15, pp. S2791–S2801.

[45] WATKINS G. D. 1986. "Deep Centers in Semiconductors". edited by Pantelides S. (New York: Gordon and Breach), p 147.

[46] KAKI H., AND HORITA, S., 2005. "Periodic Grain-boundary Formation in a Poly-Si Thin Film Crystallized by Linearly Polarized Nd:YAG Pulse Laser with an Oblique Incident Angle". J. of Appl. Phy. 97, pp. 0149041- 0149049.

[47] KIM, H. J., AND IM, J. S., 1996. "New Excimer-Laser-Crystallization Method for Producing Large-Grained and Grain Boundary-Location-Controlled Si Films for Thin Film Transistors". Appl. Phys. Lett. 68, pp. 1513-1515.

[48] OZAWA, M., OH, C.-H., AND MATSUMURA, M., 1999. "Two-Dimensionally Position-Controlled Eximer-Laser-Crystallization of Silicon Thin Films on Glassy Substrate". Jpn. J. Appl. Phys., Part 1 38, pp. 5700-5705.

[49] HARA A., AND SASAKI, N., 2000. "Control of Nucleation and Solidification Direction of Polycrystalline Silicon by Eximer Laser Irradiation". Jpn. J. Appl. Phys., Part 2 39, pp. L1-L4.

[50] SHIMIZU, K., SUGIURA, O., AND MATSUMURA, M., 1993. "High-Mobility Poly-Si Thin-Film Transistors Fabricated by a Novel Eximer Laser Crystallization Method". IEEE Electron Device Lett. 40, pp. 112-117.

[51] CHOI, D.-H., SHIMIZU, K., SUGIURA, O., AND MATSUMURA, M., 1992. "Drastic Enlargement of Grain Size of Excimer-Laser-Crystallized Polysilicon Films". Jpn. J. Appl. Phys., Part 1, Part 1 31, pp. 4545-4549.

[52] ISHIHARA, R., AND WILT, P. C. V. D., 1998. "Location Control of Crystal Si Grain Followed by Exicimer-Laser Melting of Si Thin-Films". Jpn. J. Appl. Phys., Part 2:37, pp. L15-L17.

[53] MARIUCCI, L., CARLUCCIO, R., PECORA, A., FOGLIETTI, V., FORTUNATO, G., AND SALA, D. D., 1999. "A Two-Pass Excimer Laser Annealing Process to Control Amorphous Silicon Crystallization". Jpn. J. Appl. Phys., Part 2:38, pp. L907-L910.

[54] CULLIS, A. G., 1982. "Microstructure and Topography" in "Laser Annealing of Semiconductors". Edited by POATE, J. M., AND MAYER, J. W., Academic Press, New York, pp. 147-201.

[55] FOTI, G., AND RIMINI, E., 1982. "Epitaxy by Pulsed Annealing of Ion-implanted Silicon" in "Laser Annealing of Semiconductors". Edited by POATE, J. M., MAYER, J. W., Academic Press, New York, pp. 203-245.

[56] NIPOTI, R., BIANCONI, M., FABBRI, R., AND SERVIDORI, M., 1989. "Electrical and Structural Characterization of Silicon Layers Directly Doped With Boron by Excimer Laser Irradiation". Appl. Surf. Sci. 43, pp. 321-324.

[57] FAHEY, P. M., GRIFFIN, P. B., AND PLUMMER, J. D., 1989. "Point Defects and Dopant Diffusion in Silicon". Rev. Mod. Phys. 61, pp. 289-384.

[58] CHRISTIANSEN, S., LENGSFELD, P., KRINKE, J., NERDING, M., NICKEL, N. H.AND STRUNK, H. P., 2001. "Nature of Grain Boundaries in Laser Crystallized Polycrystalline Silicon Thin Films". J. Appl. Phys., 89, pp. 5348-5354.

[59] Omling, P., Weber, E. R., Montelius, I., Alexander, H., and Michel, J., (1985). "Electrical Properties of Dislocations and Point Defects in Plastically Deformed Silicon". Phys. Rev. B, 32:10, pp. 6571-6581..

[60] ALEXANDER, H., "Changes of Electrical Properties of Silicon Caused by Plastic Deformation" in "Point and Extended Defects in Semiconductors", 1988. Edited by BENEDEK, G., pp. 51-63.

[61] PUSKA, M. J., POYKKO, S., PESOLA, M., AND NIEMINEN, R. M., 1998. "Convergence of Supercell Calculations for Point Defects in Semiconductors: Vacancy in Silicon". Phys. Rev.B 58, pp. 1318-1315.

[62] LEE, W.-C., LEE, S.-G., AND CHANG, K. J., 1998. "First-principles Study of the Self-Interstitial Diffusion Mechanism in Silicon". J. Phys.: Condens. Matter 10, pp. 995-1002.

[63] WATKINS, G. D., 1975. "Defects in Irradiated Silicon: EPR and Electron-nuclear Double Resonance of Interstitial Boron". Phys. Rev. B 12, pp. 5824-5839.

[64] EMTSEV, V. V., EHRHART, P., POLOSKIN, D. S., AND DEDEK, U., 1999. "Electron Irradiation of Heavily Doped Silicon: Group-III Impurity Ion Pairs". Physica B 273-274, pp. 287-290.

[65] CERVERA, M., GARCIA, B. J., MARTINEZ, J., GARRIDO, J., AND PIQUERAS, J., 1988. "Electrical Defect Levels in Continuous Wave Laser Annealed Silicon Metal Oxide Semiconductor Devices". J. Appl. Phys. 64, pp. 3079-3084.

[66] BARHDADI, A., AND MULLER, J. -C., 2000. "Electrically Active Defects in Silicon after various Optical Thermal Processing". Rev. Energ. Ren., 3, pp. 29-38.

[67] QIAN, J. J., WANG, Z. G., WAN, S. K., AND LIN, L. Y., 1990. "A Novel Model of "New Donors" in Czochralski-Grown Silicon". J. Appl. Phys. 68, pp. 954-957.

[68] MADA Y., AND INOUE, N., 1986. "p-n Junction Formation Using Laser Induced Donors in Silicon". Appl. Phys. Lett. 48, pp. 1205-1207.

[69] CAZCARRA V., AND ZUNINO, P., (1980). "Influence of Oxygen on Silicon Reistivity". J. Appl. Phys. 51, pp. 4206-4211.

[70] HAHN, S., HUNG, D., SHATAS, S. C., AND REK, S., (1984). "VLSI Science and Technology". Edited by BEAN, K., AND ROZGONYI, G., The Electrochem. Soc., Pennington, NJ.

[71] LANNOO, M. AND BOURGOIN, J., (1981). "Point Defects in Semiconductors I, Theoretical Aspects". Springer Series in Solid-State Sciences 22.

[72] WOLF, S. AND TAUBER, R. N., (1995). "Silicon Processing for the VLSI Era Volume 1 – Process Technology".

[73] DANNEFAER, S., (1982). "A Systematic Study of Positron Lifetimes in Semiconductors". J. Phys. C.: Solid St. Phys., 15, pp. 599-603.

[74] DANNEFAER, S., DEAN, G. W., KERR, D. P., AND HOGG, B. G., (1976). "Influence of Defects and Temperature on the Annihilation of Positrons in Neutron-Irradiated Silicon". Phys. Rev. B., 14(7), pp. 2709-2716.

[75] DANNEFAER, S., FRUENSGAARD, N., KUPCA, S. K., HOGG, B. G., AND KERR, D. P. (1983). "A Positron Study of Plastic Deformation of Silicon". Can. J. of Phys, 61, pp. 451.

[76] Dannefaer, S., Kupca, S. K., Hogg, B. G., Kerr, D. P., and Hogg. B.G., (1980). "Temperature Dependence of the Annihilation of Positrons in Si Containing Divacancies and Quadrivacancies". Phys. Rev. B., 22:12, pp. 6135-6139.

[77] DANNEFAER, S., HOGG, B., AND KERR., D. (1985). "Positron Annihilation in Silicon at High Temperatures". In Proceedings 25th Intl. Conf. on Defects in Semicond., Edited by L.C. KIMERLING AND J.M. PARSEY, pp. 255-259.

[78] CEROFOLINI, G. F., (1989). "Point and Extended Defects in Semiconductors". edited by G. Benedek, A. Cavallini and W. Schroter, NATO ASI Series, Series B: Physics, Plenum Press, New York and London, Vol. 202, pp. 124.

[79] SCHIMMEL, D. G., (1976). "A Comparison of Chemical Etches for Revealing <100> Silicon Crystal Defects". J. Electrochem. Soc., 123, pp. 734-741.

[80] SECCO D'ANGONA, F., (1972). "Dislocation Etch for (100) Planes in Silicon". J. Electrochem. Soc, 129, pp. 948-951.

[81] JENKINS, M. W., (1977). "A New Preferential Etch for Defects in Silicon Crystals". J. Electronchem. Soc., 124, pp. 757-762.

[82] SEO, Y. H., NAHM, K. S., LEE, K. D., (1993). "Mechanistic Study of Silicon Etching in HF-KBrO3-H2O Solution". J. Electronchem. Soc., 140, pp. 1453-1458.

[83] GRAFF, K., AND HEIM, P., (1994). J. Electrochem. Soc., 141, pp. 2825-2921.

[84] VOGEL, F. L., PFANN, W. G., COREY, H. E., AND THOMAS, E. E., (1953). "Observations of Dislocations in Lineage Boundaries in Germanium". Phys. Rev., 90, pp. 489-490.

[85] LEHMANN, V., (2002). "Electrochemistry of Silicon, Instrumentation, Science, Materials and Applications". WILEY-VCH.

[86] BREZNA, W., WANZENBOCK, H., LUGSTEIN, A., BERTAGNOLLI, E., GORNIK, E., AND SMOLINER, J., (2003). "Focussed Ion Beam Induced Damage in Silicon Studied by Scanning Capacitance Microscopy". Semicond. Sci. Technol. 18, pp. 195-198.

[87] HANSEN, P. J., STRAUSSER, Y. E., ERICKSON, A. N., TARSA, E. J., KOZODOY, P., BRAZEL, E. G., IBBETSON, J. P., AND MISHRA, U., (1998). "Scanning Capacitance Microscopy Imaging of Threading Dislocations in GaN Films Grown on (0001) Sapphire by Metalorganic Chemical Vapour Deposition". Appl. Phys. Lett., 72, pp. 2247-2249.

[88] LANG, D. V. (1974). "Deep-Level Transient Spectroscopy: A New Method to Characterize Traps in Semiconductors". J. of Appl. Phys. 45 (7) 3023-3032, 1974.

[89] FAN, Z. K., HO, V. Q., AND SUGANO, T., (1982). "Quenched-in Defects in Laser Annealed Silicon". Appl. phys. Lett. 40, pp. 418-420.

[90] MESLI, A., MULLER, J. C., SALLES, D., AND SIFFERT, P., (1981). "Origin of the Defects Observed after Laser Annealing of Implanted Silicon". Appl. Phys. Lett. 39, pp. 159-160.

[91] HARTITI, B., SLAOUI, A., MULLER, J. C., AND SIFFERT, P., (1989). "Electrically Active Defects in Silicon after Excimer Laser Processing". J. Appl. Phys. 66, pp. 3934-3937.

[92] RAIV, K. V., (1981). "Imperfections and Impurities in Semiconductor Silicon". Wiley, New York.

[93] GOLDSTEIN, J. I., (1981). "Scanning Electron Microscopy and X-Ray Microanalysis". Plenum, New York.

[94] THORNTON, P. R., (1968). "Scanning Electron Microscopy". Chapman and Hall, London.

[95] MURR, L., (1982). "Electron and Ion Microscopy and Analysis". Marcel Dekker Inc., New York.

[96] CRUPI, I., LOMBARDO, S., SPINELLA, C., BONGIORNO, C., LIAO, Y., GERARDI, C., FAZIO, B., VULPIO, M., AND PRIVITERA, S., (2001). "Electrical and Structural Characterization of Metal–Oxide–Semiconductor Capacitors with Silicon Rich Oxide". J. of Appl. Phys., 89:9, pp. 5552-5558 .

[97] PAN, G. Z., AND TU, K. N., (1997). "Transmission Electron Microscopy on {113} Rodlike Defects and {111} Dislocation Loops in Silicon-Implanted Silicon". J. Appl. Phys. 82, pp. 601-608.

[98] BOURRET, A., THIBAULT-DESSEAUX, J., AND SEIDMAN, D. N., (1984). "Early Stages of Oxygen Segregation and Precipitation in Silicon". 55, pp. 825-836.

[99] FURUKAWA, J., TANAKA, H., NAKADA, Y., ONO, N., SHIRAKI, H., (2000). "Investigation on Grown-in Defects in CZ-Si Crystal under Slow Pulling Rate". J. of Cryst. Growth 210, pp. 26-30.

[100] BISERO, D., (1994). "SEM Overestimation of the Mean Grain Size of Chemically Etched Polycrystalline Silicon Films". Materials Letters 18, pp. 215-217.

[101] VANDERVORST, W., AND BENDER, H. (1989). "Limitations and Use of Analytical Techniques for ULSI". Proc. of 19th European Solid State Device Res. ESSDERC 89, Springer Verlag. 843-860.

[102] COLE, D. C., (1990). "The Use of Simulation in Semiconductor Technology Development". Solid-State Electronics, 33, pp. 591-623.

[103] "The National Technology Roadmap for Semiconductors". (1997). Semiconductor Industry Association, 4300 Stevens Creek Blvd. San Jose, CA.

[104] SUBRAHMANYAN, R., (1992). "Methods for the Measurement of Two-Dimensional Doping Profiles". J. Vac. Sci. Technol. B 10, pp. 358-368.

[105] BENNINGHOVEN. A., RUDENAUER, F. G., AND WERNER, H. R., (1998). SIMS VI. Wiley, New York.

[106] LAW, M. E., (1996). "Technology Computer Aided Design Characterization Needs and Requirements, J. Vac. Sci. Technol. B14:1, pp. 213-217,.

[107] TAKAMURA, Y., VAILIONIS, A., MARSHALL, A. F., GRIFFIN, P. B., AND PLUMMER, J. D., (2002). "Dopant Deactivation in Heavily Sb Doped Si (001): A High-Resolution X-ray Diffraction and Transmission Electron Microscopy Study". J. of Appl. Phy., 92, pp. 5503-5507.

[108] MCNALLY, P. J., DANILEWSKY, A. N., CURLEY, J. W., READER, A., RANTAMAKI, R., TUOMI, T., BOLT, M., AND TASKINEN, M., (1999). Microelectronic Engineering 45, pp. 47-56.

[109] SUBRAMANYAN, R., MASSOUD, H. Z., AND FAIR, R. B., (1988). "Accurate Junction Depth Measurements using Chemical Staiing, Semiconductor Fabrication: Technology and Metrology". ASTM STP, pp. 990.

[110] Wu, C. P., Douglas, E. C., Mueller, C. W., and Williams, R., (1979). "Techniques for Lapping and Staining Ion-Implanted Layers". J. Electrochem. Soc. 126, pp. 1982-1988.

[111] SHIH, S., JUNG, K. H., HSIEH, T. Y., SARATHY, J., CAMPBELL, J. C., AND KWONG, D. L., (1992). "Photoluminescence and Formation Mechanism of Chemically Etched Silicon". Appl. Phys. Lett., 60, pp. 1863-1865.

[112] S. M. HU AND D. R. KERR, (1967). "Observation of Etching of n-Type Silicon in Aqueous HF Solutions". J. Electrochem. Soc: Solid State Science, pp. 414.

[113] WOLF, P. D, STEPHENSON, R., TRENKLER, T., CLARYSSE, T., HANTSCHEL, T., AND VANDERVORST, W., (2000). "Status and Review of Two-Dimensional Carrier and Dopant Profiling using Scanning Probe Microscopy". J. Vac. Sci. Technol. B 18, pp. 361-368.

[114] LIU, J., DASS, M. L. A., AND GRONSKY, R., (1994). "Transmission Electron Microscopy Study of Two-Dimensional Semiconductor Device Junction Delineation by Chemical Etching". J. Vac. Sci. Technol. B 12, pp. 353-356.

[115] ALVIS, R., LUNING, S., THOMPSON, L., SINCLAIR, R., AND GRIFFIN, P., (1996). "Physical Characterization of Two-Dimensional Doping Profiles for Process Modeling". J. Vac. Sci. Technol. B 14, pp. 231-235.

[116] SPINELLA, C., RAINERI, V., VIA, F. L., AND CAMPISANO, S. U., (1996). "Two-Dimensional Junction Profiling by Selective Chemical Etching: Applications to Electron Device Characterization ". J. Vac. Sci. Technol. B 14, pp. 414-420.

[117] TAKIGAMI, T., AND TANIMOTO, M., (1991). "Measurements of the Three-Dimensional Impurity Profile in Si using Chemical Etching and Scanning Tunneling Microscopy". Appl. Phys. Lett. 58, pp. 2288-2290.

[118] BARRETT, M., DENNIS, M., TIFFIN, D., LI, Y., AND SHIH, C. K. , (1995). "2-D Dopant Profiling in VLSI Devices Using Dopant-Selective Etching: An Atomic Force Microscopy Study". IEEE Electron Device Lett. 16, pp. 118-120.

[119] BARRETT, M., SHIH, C. K., DENNIS, M., TIFFIN, D., AND LI, Y., (1996). "Two-dimensional dopant profiling of very large scale integrated devices using selective etching and atomic force microscopy". J. Vac. Sci. Technol. B 14, pp. 447-451.

[120] ALVIS, R., MANTIPLY, B., AND YOUNG, M., (1996). "Junction Metrology by Cross-Sectional Atomic Force Microscopy". J. Vac. Sci. Technol. B 14, pp. 452-456.

[121] Roberts, M. C., Booker, G. R., Davidson, S. M., and Yallup, K. J., (1983). "TEM Studies of Small Geometry Silicon MOSFETs". Inst. Phys. Conf. Ser. 67, 467.

[122] GONG, L., BARTHEL, A., LORENZ, J., AND RYSSEL, H., "Simulation of the Lateral Spread of Implanted Ions - Experiments" in "Proceedings of the ESSDEC '89". Edited by A. HEUBERGER, H. RYSSEL, AND P. LANGE, Springer, Berlin, pp. 198–201 (1989).

[123] VANDERVORST, W., CLARYSSE, T., VANHELLEMONT, J., AND ROMANO-RODRIGUEZ, A., (1992). "Two-Dimensional Carrier Profiling". J. Vac. Sci. Technol. B 10, 449-455.

[124] RAINERI, V., PRIVITERA, V., VANDERVORST, W., HELLEMANS, L., AND SNAUWAERT, J., (1994). "Carrier Distribution in Silicon Devices by Atomic Force Microscopy on Etched Surfaces". Appl. Phys. Lett. 64, pp. 354-356.

[125] SHENG, T. T., AND MARCUS, R. B., (1981). "Delineation of Shallow Junctions in Silicon by Transmission Electron Microscopy". Solid-State Sci. Technol. 128, pp. 881-884.

[126] GOLD, D. P., WILLS, J. H., BOOKER, G. R., WILSON, M. C., AND GODFREY, D. J., (1989). Inst. Phys. Conf. Ser. 100, Section 11.

[127] ROBERTS, M. C., YALLUP, K. J., AND BOOKER, G. R., (1985). Inst. Phys. Conf. Ser. 76, Section 11.

[128] NEOGI, S. S., VENABLES, D., NA, Z., AND MAHER, D. M., (1998). "Factors Affecting Two-Dimensional Dopant Profiles Obtained by Transmission Electron Microscopy of Etched p- n Junctions in Si". J. Vac. Sci. Technol. B 16, pp. 471-475.

[129] YOO, K. D., MARSH, C. D., AND BOOKER, G. R., (2002). "Two-Dimensional Dopant Concentration Profiles from Ultrashallow Junction Metal-Oxide-Semiconductor Field-Effect Transistors Using the Etch/Transmission Electron Microscopy Method". App. Phys. Lett., 80, pp. 2687-2689.

[130] SPINELLA, C., RAINERI, V., AND CAMPISANO, S. U., (1995). "Selective Etching of B-Doped Silicon: Mechanisms and Two-Dimensional Delineation of Concentration Profiles". J. Electrochem. Soc., 142, pp. 1601-1607.

[131] CHOI, C.-J., AND SEONG, T.-Y., (2000). "Transmission Electron Microscopy Study of Two-Dimensional Dopant Profiling in Metal-Oxide-Semiconductor Field Effect Transistor Test Structures and Devices". J. Electrochem. Soc., 147:4, pp. 1525-1529.

[132] TAKIGAMI, T., AND TANIMOTO, M., (1994). "Measurements of the Three-dimensional Impurity Profile in Silicon using Chemical Etching and Scanning Tunneling Microscopy". Appl. Phys. Lett. 64, pp. 354-356.

[133] WANG, X.-D., MAHAFFY, R., TAN, K., SHIH, C. K., LEE, J. J., AND FOISY, M., (2000). "Two-Dimensional Dopant Profile of 0.2 μm Metal–Oxide–Semiconductor Field Effect Transistors". J. Vac. Sci. Technol. B 18, pp. 560-565.

[134] BARRETT, M., DENNIS, M., TIFFIN, D., LI, Y., AND SHIH, C. K., 1996. "Two-Dimensional Dopant Profiling of Very Large Scale Integrated Devices using Selective Chemical Etching and Atomic Force Microscopy". J. Vac. Sci. Technol. B 14(1), pp. 447-451.

[135] ALVIS, R., MANTIPLY, B., AND YOUNG, M., (1996). "Junction metrology by cross-sectional atomic force microscopy". J. Vac. Sci. Technol. B 14, pp. 452-456.

[136] UKRAINTSEV, V. A., MCGLOTHLIN, R., GRIBELYUK, M. A., AND EDWARDS, H., (1998). "Strong Effect of Dopant Concentration Gradient on Etching Rate". J. Vac. Sci. Technol. B 16, pp. 476-480.

[137] TSENG, W. F., AND WILKINS, B. R., (1987). "Direct Observations of n-MOSFET Channel Lengths". J. Electrochem. Soc. 134, pp. 1258-1260.

[138] TRENKLER, T., STEPHENSON, R., JANSEN, P., VANDERVORST, W., AND HELLEMANS, L., (2000). "New Aspects of Nanopotentiometry for Complementary Metal–Oxide–Semiconductor Transistors". J. Vac. Sci. Technol. B 18, pp. 586-594.

[139] BAN, D., SARGENT, E. H., DIXON-WARREN, ST. J., CALDER, I., SPRINGTHORPE, A. J., DWORSCHAK, R., ESTE, G., AND WHITE, J. K., (2002). "Direct Imaging of the Depletion Region of an InP p–n Junction under Bias using Scanning Voltage Microscopy". Appl. Phys. Lett., 81, pp. 5057-5059.

[140] ZAVYALOV, V. V., MCMURRAY, J. S., STIRLING, S. D., WILLIAMS, C. C., AND SMITH, H., (2000). "Two Dimensional Dopant and Carrier Profiles Obtained by Scanning Capacitance Microscopy on an Actively Biased Cross-Sectioned Metal–Oxide–Semiconductor Field-Effect Transistor". J. Vac. Sci. Technol. B 18, pp. 549-554.

[141] MURALT, P., MEIER, H., POHL, D. W., AND SALEMINK, H. W. M., (1987). "Scanning Tunneling Microscopy and Potentiometry on a Semiconductor Heterojunction". App. Phys. Lett., 55, pp. 1352-1354.

[142] WILLIAMS, C. C., SLINKMAN, J., HOUGH, W. P., AND WICKRAMSINGHE, H. K., (1989). "Lateral Dopant Profiling with 200 nm Resolution by Scanning Capacitance Microscopy". App. Phys. Lett., 55, pp. 1662-1664.

[143] HESSEL, H. E., MEMMERT, U., CERA, H., AND BEHM, R. J., (1991). "Dopant Migration in Silicon during Implantation/Annealing Measured by Scanning Tunneling Microscopy". J. Vac. Sci. Technol. B, 9, pp. 690-694.

[144] HOSAKA, S., HOSOKI, S., TAKATA, K., HORIUCHI, K., AND NATSUAKI, N., (1988). "Observation of pn Junctions on Implanted Silicon using a Scanning Tunneling Microscope". App. Phys. Lett., 53, pp. 487-489.

[145] KORDIC, S., VANLOENEN, E. J., DIJKKAMP, D., HOEVEN, A. J., AND MORAAL, H. K., (1990). "Scanning Tunneling Spectroscopy on Cleaved Silcion pn Junctions". J. Vac. Sci. Technol. A, 8, pp. 549-552.

[146] KIM, Y.-C., NOWAKOWASKI, M. J., AND SEIDMAN, D. N., (1996). "Novel in situ Cleavage Technique for Cross-Sectional Scanning Tunneling Microscopy Sample Preparation". Rev. Sci. Instrum. 67, pp. 1922-1924.

[147] BOURGOIN, J.-P., JOHNSON, M. B., AND MICHEL, B., (1994). "Semiconductor Characterization with the Scanning Surface Harmonic Microscope". Appl. Phys. Lett. 65, pp. 2045-2047.

[148] HENNING, A. K., HOCHWITZ, T., SLINKMAN, J., NEVER, J., HOFFMANN, S., KASZUBA, P., AND DAGHLIAN, C., (1995). "Two-dimensional surface dopant profiling In silicon using scanning Kelvin probe microscopy". J. Appl. Phys. 77, pp. 1888-1896.

[149] SZE, S. M., (1981). "Physics of Semiconductor Devices". 2nd ed. Wiley, New York.

[150] TAUR, Y., AND NING, T. H., (1998). "Fundamentals of Modern VLSI Devices". Cambridge Univeristy Press, UK.

[151] POYAI, A., CLAEYS, C., AND SIMOEN, E., (2002). "Improved extraction of carrier concentration and depletion width from capacitance–voltage characteristics of silicon n^+– p-well junction diodes". Appl. Phys. Lett., 80, pp. 1192-1194.

[152] MATEY, J. R., AND BLANC, J., (1985). "Scanning Capacitance Microscopy". J. Appl. Phys. 57, pp. 1437-1444.

[153] EDWARDS, H., UKRAINTSEV, V. A., MARTIN, R. S., JOHNSON, F. S., MENZ, P., WALSH, S., ASHBURN, S., WILLS, K. S., HARVEY, K., AND CHANG, M.-C., (2000). "pn-junction delineation in Si devices using scanning capacitance spectroscopy". J. Appl. Phys., 87, pp. 1486-1495.

[154] Nicollian, E. H., and Brews, J. R. , (1982). "MOS Physics and Technology", Wiley, New York.

[155] HUANG, Y., WILLIAMS, C. C., AND SLINKMAN, J., (1995). "Quantitative two-dimensional dopant profile measurement and inverse modeling by scanning capacitance microscopy". Appl. Phys. Lett. 66, pp. 344-346.

[156] ZAVYALOV, V. V., MCMURRAY, J. S., AND WILLIAMS, C. C., (1999). "Advances in experimental technique for quantitative two-dimensional dopant profiling by scanning capacitance microscopy". Rev. Sci. Instrum., 70, pp. 158-164.

[157] ISENBART, J., BORN, A., AND WIESENDANGER, R., (2001). "The physical principles of scanning capacitance spectroscopy". Appl. Phys. A 72 [Suppl.], S243–S251.

[158] MAZUR, R. G., AND DICKEY, D. H., (1966). "A Spreading Resistance Technique for Resistivity Measurements on Silicon". J. Electrochem. Soc. 113, pp. 255.

[159] VANDERVORST, W., CLARYSSE, T., AND SMITH, H. E., (1996). "Influence of the substrate doping level on spreading resistance profiling". J. Vac. Sci. Technol. B, 14, pp. 404-407.

[160] VANDERVORST, W., CLARYSSE, T., AND EYBEN, P., (2002). "Spreading resistance roadmap towards and beyond the 70 nm technology node". J. Vac. Sci. Technol. B 20, pp. 451-458.

[161] EYBEN, P., XU, M., DUHAYON, N., CLARYSSE, T., CALLEWAERT, S., AND VANDERVORST, W., (2002). "Scanning spreading resistance microscopy and spectroscopy for routine and quantitative two-dimensional carrier profiling". J. Vac. Sci. Technol. B 20, pp. 471-478.

[162] BRYAN, S. R., WOODWARD, W. S., LINTON, R. W., AND GRIFFIS, D. P., (1985). "Secondary ion mass spectrometry/digital imaging for the three-dimensional chemical characterization of solid state devices". J. Vac. Sci. Tech. A3, pp. 2102-2107.

[163] DOWSETT, M. G., AND COOKE, G. A., (1992). "Two dimensional profiling using secondary ion mass spectrometry". J. Vac. Sci. Technol. B, 10, pp. 353-357.

[164] ROBERTS, M. C., BOOKER, G. R., DAVIDSON, S. M., AND YALLUP, K. J., (1983). "TEM Studies of Small Geometry Silicon MOSFETs". Inst. of Phys. Conf. Series No. 67: Section 10. London, Institute of Physics.

[165] DOWSETT, M. G., (2003). "Depth Profiling using Ultra-Low-Energy Secondary Ion Mass Spectrometry". Appl. Surf. Sci., 203-204, pp. 5-12.

[166] STEVIE, F. A., (1992). "Secondary ion mass spectrometry ananlysis strategy for shallow junctions on test and product silicon wafers". J. Vac. Sci. Technol. B, 10, pp. 323-328.

[167] UKRAINTSEV, V. A., CHEN, P. J., GRAY, J. T., MACHALA, C. F., MAGEL, L. K., AND CHANG, M.-C., (2000). "High-resolution two-dimensional dopant characterization using secondary ion mass spectrometry". J. Vac. Sci. Technol. B, 18, pp. 580-585.

[168] ROITMAN, P., ALBERS, J., AND MEYERS, D. R., (1984). "An Investigation of the Two-Dimensional Shape of Ion-Implanted Regions". J. Appl. Phys. 55, pp. 4436-4443.

[169] PEROVIC, D. D., CASTELL, M. R., HOWIE, A., LAVOIE, C., TIEDJE, T., AND COLE, J. S. W., (1994). "Doping layer imaging in the field-emission scanning electron microscope". Proc. of 13th Intl. Cong. on Elec. Microscopy, 1, pp. 91-92.

[170] PEROVIC, D. D., CASTELL, M. R., HOWIE, A., LAVOIE, C., TIEDJE, T., COLE, AND, J. S. W., (1995), "Field-emission SEM imaging of compositional

and doping layer semidconductor superlattices". Ultramicroscopy 58, pp. 104–113.

[171] CASTELL, M. R., MULLER, D. A., AND VOYLES, P. M., (2003). "Dopant mapping for the nanotechnology age". Nature Materials, 2, pp. 129-131.

[172] CASTELL, M. R.,SIMPSON,T.W.,MITCHELL, I. V.,PEROVIC,D. D. AND BARIBEAU, J. M., (1999). "Deactivation and diffusion of boron in ion-implanted silicon studied by secondary electron imaging". Appl. Phys.Lett. 74, pp. 2304–2306.

[173] SEALY, C. P., CASTELL, M. R., AND WILSHAW, P. R. J., (2000). "Mechanism for Secondary Electron Dopant Contrast in the SEM". Electron.Microsc. 49, pp. 311–321.

[174] ELLIOTT, S. L., BROOM, R. F., AND HUMPHREYS, C. J., (2002). "Dopant profiling with the scanning electron microscope—A study of Si". J. Appl. Phys., 91, pp. 9116-9122.

[175] TURAN, R., PEROVIC, D. D., AND HOUGHTON, D. C., (1996). "Mapping electrically active dopant profiles by field-emission scanning electron microscopy". Appl. Phys. Lett. 69, pp. 1593-1595.

[176] VENABLES, D., JAIN, H., AND COLLINS, D. C., (1998). "Secondary electron imaging as a two-dimensional dopant profiling technique: Review and update". J. Vac. Sci. Technol. B, 16, pp. 362-366.

[177] SCHONJAHN, C., HUMPHREYS, C. J., AND GLICK, M., (2002). "Energy-filtered imaging in a field-emission scanning electron microscope for dopant mapping in semiconductors". J. Appl. Phys., 92, pp. 7668-7671.

[178] TURNER, D. R., (1960). "On the Mechanism of Chemically Etching Germanium and Silicon". J. Electrochem. Soc. 107, pp. 810-816.

[179] NEOGI, S. S., VENABLES, D., MA, Z., MAHER, D. M., TAYLOR, M., AND CORCORAN, S., (1997). "Mapping two-dimensional arsenic distributions in silicon using dopant-selective chemical etching technique". J. Appl. Phys., 82, pp. 5811-5815.

[180] OVERWIJK, M. H. F., VAN DEN HEUVEL, F.C., AND BULLE-LIEUWMA, C.W.T., (1993). "Novel Scheme for the Preparation of Transmission Electron Microscopy Specimens with a Focused Ion Beam". J. Vac. Sci. Technol. B, 11, pp. 2021-2024.

[181] LIU, S., PALSULE, C., YI, S., AND GANGOPADHYAY, S., (1994). "Characterization of Stain-Etched Porous Silicon". Phys. Rev. B, 49:15, pp. 10318-10325.

[182] WHELAN, S., PRIVITERA, V., ITALIA, M., MANNINO, G., BONGIORNO, C., SPINELLA, C., FORTUNATO, G., MARIUCCI, L., STANIZZI, M., AND MITTIGA, A., (2002). "Redistribution and electrical activation of ultralow energy implanted boron in silicon following laser annealing". J. Vac. Sci. Technol. B, 20, pp. 644-649.

[183] MCCAFFREY, J. P., PHANEUF, M.W., AND MADSEN, L.D., (2001). "Surface damage formation during ion-beam thinning of samples for transmission electron microscopy". Ultramicroscopy 87, pp. 97-104.

[184] NISHIO, K., ISSHIKI, T., AND SHIOJIRI, M., (2000). "Quantitative intensity measurement of equal thickness fringes in Si and MgO crystal images with an energy-filtering transmission electron microscope using an imaging plate". J. of Electron Microscopy 49, pp. 607-619.

[185] FATHAUER, R. W., GEORGE, T., KSENDZOV, A., AND VASQUEZ, R. P., (1992). "Visible luminescence from silicon wafers subjected to stain etches". Appl. Phys. Lett. 60:8, pp. 995-997.

[186] FAIR, R. B., "Concentration Profiles of Diffused Dopants in Silicon" (1981), in "Impurity Doping Processes in Silicon", ed. by F. F. Y. WANG, Materials Processing-Theory and Practices, Amsterdam: North-Holland, 2, pp. 338.

[187] Combescot, M., and Bok, J., (1984). "Instability at the Melting Threshold of Laser-Irradiated Silicon". Phys. Rev. B 29, pp. 6393-6395.

[188] BIRNBAUM, M., (1965). "Semiconductor Surface Damage Produced by Ruby Lasers". J. Appl. Phys. 36, pp. 3688-3689.

[189] EMMONY, D. C., HOWSON, R. P., AND WILLIS, L. J., (1973). "Laser Mirror Damage in Germanium at 10.6 um". Appl. Phys. Lett. 23, pp. 598-600.

[190] WALTERS, C. T., (1974). "Surface Scattering at LSD-Wave Initiation Sites on Nonmetallic Materials". Appl. Phys. Lett. 25, pp. 696-698.

[191] Isenor, N. R., (1977). "CO2 laser-Produced Ripple Patterns on Ni_xP_{1-x} Surfaces". Appl. Phys. Lett. 31, pp. 148-150.

[192] THEPPAKUTTAI, S., AND CHEN, S., (2004). "Submicron Ripple Formation on Glass Surface upon Laser-Nanosphere Interaction". J. Appl. Phys. 95, pp. 5049-5052.

[193] KEILMANN, F., AND BAI, Y. H., (1982). "Periodic Surface Structures Frozen. into CO_2 Laser-Melted Quartz". Appl. Phys. A, 29, pp. 9-18.

[194] MARACAS, G. N., HARRIS, G. L., LEE, C. A., AND MCFARLANE, R. A., (1978). "On the Origin of Periodic Surface Structure of Laser-Annealed Semiconductors". Appl. Phys. Lett. 33, pp. 453-455.

[195] SIPE, J. E., YOUNG, J. F., PRESTON, J. S., AND VAN DRIEL, H. M., (1983). "Laser-Induced Periodic Surface Structure. I. Theory". Phys. Rev. B, 27, pp. 1141-1154.

[196] GUOSHENG, Z., FAUCHET, P. M., AND SIEGMAN, A. E., (1982). "Growth of Spontaneous Periodic Surface Structures on Solids during Laser Illumination". Phys. Rev. B 26, pp. 5366-5381.

[197] YOUNG, J. F., SIPE, J. E., PRESTON, J. S., AND VAN DRIEL, H. M., (1982). "Laser-Induced Periodic Surface Damage and Radiation Remnants". Appl. Phys. Lett. 41, pp. 261-264.

[198] FAUCHET, P. M., AND SIEGMAN, A. E., (1982). "Surface Ripples on Silicon and Gallium Arsenide under Picosecond laser Illumination". Appl. Phys. Lett. 40, pp. 824-826.

[199] LIAO, Y., DEGORCE, J.-Y., AND MEUNIER, M., (2005) "Laser Induced Formation of Periodic Nanostructures in Silicon Covered by SiO_2". Submitted to Applied Physics A.

[200] LIAO, Y., DEGORCE, J.-Y., BELISLE, J., AND MEUNIER, M., (2005). "2-D Dopant Determination in Laser Locally Modified Si Microdevices using Dopant-selective Etching". Submitted to Journal of The Electrochemical Society.

[201] Schroder, D. K., (1990). "Semiconductor Material and Device Characterization". John Wiley, New York.

[202] YAMAMOTO, T., SUZUKI, Y., MIYASHITA, M., SUGIMURA, H., AND NAKAGIRI, N., (1997). "Scanning Capacitance Microscopy as a Characterization Tool for Semiconductor Devices". Jpn. J. Appl. Phys. 36, pp. 1922-1926.

[203] NAKAGIRI, N., YAMAMOTO, T., SUGIMURA, H., SUZUKI, Y., MIYASHITA, M., AND WATANABE, S., (1997). "Application of Scanning Capacitance Microscopy to Semiconductor Devices". Nanotechnology 8, pp. A32-A37.

[204] WHELAN, S., LA MAGNA, A., PRIVITERA, V., MANNINO, G., ITALIA, M., BONGIORNO, C., FORTUNATO, G., AND MARIUCCI, L., (2003). "Dopant Redistribution and Electrical Activation in Silicon Following Ultra-low Energy Boron Implantation and Excimer Laser Annealing". Phys. Rev. B, 67, pp. 075201-075208.

[205] OZKAN, A. M., MALSHE, A. P., RAILKAR, T. A., BROWN, W. D., SHIRK, M. D., AND MOLIAN, P. A., (1999). "Femtosecond Laser-Induced Periodic Structure Writing on Diamond Crystals and Microclusters". Appl. Phys. Lett., 75, pp. 3716-3718.

[206] VAREL, H., WAHMER, M., ROSENFELD, A., ASHKENASI, D., AND CAMPBELL, E. E. B., (1998). "Femtosecond Laser Ablation of Sapphire: Time-of-Flight Analysis of the Ablation Plume". Appl. Surf. Sci. 127-129, pp. 128-133.

[207] IHLEMANN, J., WOLFF, B., AND SIMON, P., (1992). "Nanosecond and Femtosecond Excimer Laser Ablation of Fused Silica". Appl. Phys. A: Solids Surf. 54, pp. 363-368.

[208] LEAMY, H. J., ROZGONYI, G. A., SHENG, T. T., AND CELLER, G. K., (1978). "Periodic Regrowth Phenomena Produced by Laser Annealing of Ion-Implanted Silicon". Appl. Phys. Lett. 32, pp. 535-537.

[209] HANEMAN, D., AND NEMANICH, R. J., (1982). "Surface Topography of Laser Annealed Silicon". Solid State Commun. 43, pp. 203-206.

[210] TEMPLE, P. A., AND SOILEAU, M. J., (1981). " Polarization Charge Model for Laser-Induced Ripple Pattern in Dielectric Materials". IEEE J. Quant. Elec. QE-17, pp. 2067-2072.

[211] ORON, M., AND SORENSEN, G., (1979). "New Experimental Evidence of the Periodic Surface Structure in Laser Annealing". Appl. Phys. Lett. 35, pp. 782-784.

[212] FAUCHET, P. M., AND SIEGMAN, A. E., (1981). "Surface Ripples on Silicon and Gallium Arsenide under Picosecond Laser Illumination". Appl. Phys. Lett. 40, pp. 824-826.

[213] ZAVECZ, T. E., AND SAIFI, M. A., (1975). "Metal Reflectivity under High–Intensity Optical Radiation". Appl. Phys. Lett. 26, pp. 165-168.

[214] KOO, J. C., AND SLUSHER, R. E., (1976). "Diffraction from Laser-Induced Deformation on Reflective Surfaces". Appl. Phys. Lett. 28, pp. 614-616.

[215] BOSCH, M. A. AND LEMONS, R. A., (1981). "Laser-Induced Melt Dynamics of Si and Silica". Phys. Rev. Lett. 47, pp. 1151-1155.

[216] CHIM, W. K., WONG, K. M., TEO, Y. L., LEI, Y., AND YEOW, Y. T., (2002). "Dopant Extraction from Scanning Capacitance Microscopy Measurements of p-n Junctions using Combined Inverse Modeling and Forward Simulation". Appl. Phys. Lett., 80, pp. 4837-4839.

[217] NEMANICH, R. J., BIEGELSEN, D. K., AND HAWKINS, W. G., (1983). "Aligned, Coexisting Liquid and Solid Regions in Laser-Annealed Si". Phys. Rev. B 27, pp. 7817-7819.

[218] YOUNG, J. F., SIPE, J. E., AND VAN DRIEL, H. M., (1983). "Regimes of Laser-Induced Periodic Surface Structure on Germanium: Radiation Remnants and Surface Plasmons". Opt. Lett. 8, pp. 431-433.

[219] VAN VECHTEN, J. A., (1985). "Experimental Tests for Boson Condensation and Superconductivity in Semiconductors during Pulsed Beam Annealing". Solid State Commun. 39, pp. 1285-1291.

[220] ANTHONY, T. R., AND CLINE, H. E., (1977). "Surface Rippling Induced by Surface-tension Gradients During Laser Surface Melting and Alloying". J. Appl. Phys. 48, pp. 3888-3894.

[221] COHEN, S. S., WYATT, P. W., CHAPMAN, G. H., AND CANTER, J. M., (1988). "Laser-Induced Diode Linking for Wafer-Scale Integration". IEEE Trans. Electr. Dev. 35, pp. 1533-1550.

[222] COHEN, S. S., WYATT, P. W., AND CHAPMAN, G. H., AND CANTER J. M., (1989). "The Resistance of Laser-Diffused Diode Links". IEEE Trans. Electr. Dev. ED-36, pp. 1220-1223.

[223] CALDER, I. D., AND NAGUIB, H. M., (1985). "Activation of Polysilicon Connections by Selective CW Laser Annealing". IEEE Electr. Dev. Lett. 6, pp. 557-559.

[224] NISHIHIRA, K., AND MOTOOKA, T., (2002). "Molecular-Dynamics Simulations of Crystal Growth from Melted Si: Self-Interstitial Formation and Migration". Phys. Rev. B, 66, pp. 2333101-2333104.

[225] BASU, B., AND DATE, A. W., (1992). "Rapid Solidification Following Laser Melting of Pure Metals-1. Study of Flow Field and Role of Convection". Int. J. Heat Mass Transfer. 35(5), pp. 1049-1058.

[226] MCCAY, M. H., HOPKINS, J. A., AND MCCAY, T. D., (2002). "Melt Instabilities During Laser Surface Alloying". J. Laser Appl., 14:1, pp. 24-30.

[227] RABIER, J., GAREM, H., AND VEYSSIERE, P., (1976). "Transmission Electron Microscopy Determinations of Dislocation Burgers Vectors in Plastically

Deformed Yttrium Iron Garnet Single Crystals". J. Appl. Phys., 47, pp. 4755-4758.

[228] BROWN, R. A., MAROUDAS, D., SINNO, T., (1994). "Modelling Point Defect Dynamics in the Crystal Growth of Silicon". J. of Cryst. Grow., 137, pp. 12-25.

[229] VINTSENTS, S. V., ZAITSEVA, A. V., AND PLOTNIKOV, G. S., (2003). "Self-Organization of Laser-Induced Point Defects at the Initial Stages of Inelastic Photodeformation in Germanium". Semiconductors, 37, pp. 124-130.

[230] PARK, J.-G., KURITA, K., LEE, G.-S., SHIN, S.-A, AND FURUYA, H., (2003). "Dependence of Crystal Nature on the Gettering Efficiency of Iron and Nickel in a Czochralski Silicon Wafer". Microelectronic. Eng., 66, pp. 247-257.

[231] Christian, J. W., (2002). "The Theory of Transformations in Metals and Alloys Part 1", Amsterdam, Pergamon Press.

[232] CULLIS, A. G., WEBBER, H. C., CHEW, N. G., POATE, J. M., AND BAERI, P., (1982). "Transitions to Defective Crystal and the Amorphous State Induced in Elemental Si by Laser Quenching". Phys. Rev. Lett. 49, pp. 219-222.

[233] GOSELE, U., FRANK, W., AND SEEGER, A., (1983). "An Entropy Barrier against Vacancy-Interstitial Recombination in Silicon". Solid State Commun., 45, pp. 31-33.

[234] YANG, D., AND QUE, D., (1999). "Influence of Dislocations on Nitrogen-Oxygen Complex in Silicon" phys. stat. sol. (a) 171, pp. 203-207.

[235] INOUE, N., WADA, K., AND OSAKA, J., (1987). "Defects and Properties of Semiconductors: Defect Engineering", edited by J. CHIKAWA, K. SUMINO, AND K. WADA, KTK Scientific, Tokyo, p. 197.

[236] GRUHN, H., HEIDINGER, R., ROHDE, M., RUDIGER, S., SCHNEIDER, J., AND GAHR, K.-H. Z., (2000). "Of the Laser Induced Surface Modification of Ceramic Substrates for Thermal and Electrical Lines in Microsystems". Mat. Res. Soc. Symp. 617, pp. J5.3.1-J5.3.6.

[237] LONGTIN, J. P., HIJIKATA, K., AND OGAWA, K., (1999). "Laser-Induced Surface-Tension-Driven Flows in Liquids". Int. J. Heat Mass Tran. 42, pp. 85-93.